Molecular Tensile Machines: a New Tool for Quantitative Mechanochemistry

Yuanchao Li

A dissertation submitted to the faculty of the University of North Carolina at Chapel Hill in partial fulfillment of the requirements for the degree of Doctor of Philosophy in the Department of Chemistry

Chapel Hill
2013

Approved by:

Stephen Craig

Michael Rubinstein

Edward Samulski

Sergei Sheiko

Wei You

ABSTRACT

YUANCHAO LI: Molecular Tensile Machines: a New Tool for Quantitative Mechanochemistry
(Under the direction of Sergei Sheiko)

Controlling force at molecular length scales is a challenge in mechanochemistry. Well-defined macromolecules and tools that allow accurate control of both magnitude and direction of bond tension have been developed during the past two decades. Our contribution to this endeavor has been the design of molecular tensile machines that are highly branched macromolecular architectures (e.g. bottlebrushes, pom-poms, and dendrimers), which are able to generate bond tensions up to nanoNewton range due to steric repulsion between densely grafted branches. Furthermore, these macromolecular devices allow accurate variation of the bond tension through changes in the surrounding environment such as temperature, solvent quality, and salinity, making them ideal systems for the study of quantitative mechanochemistry.

In this dissertation, we focus on bottlebrushes that can generate bond tension along the backbone and also amplify & focus this tension to a chemical group of interest. We have explored two complementary effects of the self-generated tension: activation of chemical reactions and electronic properties. Specifically, we have studied homolytic cleavage and reduction of disulfides under controlled force and analyze the bond activation parameters quantitatively. We have shown that the scission rate of disulfide increases exponentially with tension as reported by others but decreases with temperature. This anti-Arrhenius behavior is ascribed to the decrease of backbone tension with

temperature, which can overpower thermal effect. Moreover, the reduction rate constant at zero force was found significantly lower than that in bulk solution, which suggests an acidic composition of the water surface with pH=3.7. To investigate the effect of tension on electronic structures, we have synthesized bottlebrushes with a polythiophene backbone and constructed a unique experimental set-up enabling measurements of fluorescence spectra of sub-monolayer films as a function of backbone tension. The energy band gap was found decreasing with tension due to the increase of conjugation length and then increasing due to the deformation of bond lengths and angles, which agrees with our prediction by DFT calculations.

In addition to bottlebrushes, we have explored other types of strained molecular architectures including spoked-wheel macromolecules and block-copolymer brushes. Molecular dimensions and emission spectra of these unique molecular architectures have been characterized.

ACKNOWLEDGMENT

Most importantly I would like to thank my advisor Dr. Sergei Sheiko for taking me under your wing and sharing your knowledge, not just science but about life as well.

I would like to thank all of my friends and colleagues, past and present, in the Sheiko group: Mike, Sherryl, Natalia, Alex, Jing, Ping, Will, Chelsea, David and Frank, thank you for making graduate research and life fun. I would like to thank our esteemed colleagues, especially at Carnegie Mellon University (Prof. Matyjaszewski and his group) and Eindhoven University of Technology (Prof. E. W. Meijer and his group) for the collaborations and friendships. I would also like to thank my graduate committee for their advice, time and discussions.

I would like to thank all my family. My parents for their love and support for my graduate study abroad. My brothers and sisters-in-law for taking care of the whole family when I was away. My niece, Chuhan, for her birth and bringing happiness to the family. I would also to thank my grandparents who I have missed so much.

Finally, I would like to thank all my friends, Kunqiang, Songpan, Yesu, Xing, Yuan, Kai, Can, Hongbei, and others, who have helped me get to this point in one piece. I couldn't have made it this far without any of your help.

TABLE OF CONTENTS

LIST OF TABLES

Table

LIST OF FIGURES

Figure

Chapter 1

Introduction

1.1 An overview on mechanochemistry

As one can learn from chemistry textbooks, chemical reactions can be induced by heat, light, and electric current, corresponding to thermochemistry, photochemistry and electrochemistry respectively. Yet, there is another stimulus that can trigger chemical reactions: mechanical force, which is arguably even more common than heat and light as it controls many biochemical process and behavior of life objects. The effect of mechanical force on the course of chemical reactions is one of the earliest experiences of mankind, and it has have been utilized since prehistorical time when primitive man used friction to make fire and is still frequently used in many fields. The first written document of a mechanochemical reaction is found in a book by Theophrastus of Ephesus (371-286 B.C.), a student of Aristotle: if native cinnabar is rubbed in a brass mortar with a brass pestle in the presence of vinegar, metallic mercury is obtained.[1] However, unlike other reaction stimuli, the effect of mechanical forces on molecular length scales is less understood due to poorly controlled distribution of mechanical forces over myriad of chemical bonds within a macroscopic sample. As such, mechanochemistry remains a well-established and active field of science, which studies the coupling of the mechanical and chemical phenomena on both macroscopic and molecular scale, including bonds fracture, protein folding, and force-induced variations of color. Mechanochemistry is in wide use in material science,[2-3] force sensors,[4] *etc*…

Besides, it has potential application in self-healing materials, lithography, chemical synthesis and drug delivery. Therefore, it is of great importance to first understand the fundamentals of mechanochemistry.

Although mechanochemistry has drawn scientists' attention for centuries, [1,3,5] conventional mechanochemistry remains largely destructive and non-selective. One of the most studied mechanochemical processes is the degradation of polymers that can occur both in solution (ultrasonic irradiation and flows)[6-13] and in the solid state (mastication, cold-milling, and stretching).[14-16] In flow, the central bond in a linear polymer chain experiences the highest tension[17] and thus has the highest probability to break.[18-21] Kinetic studies have been done to elucidate the molecular mechanism of degradation and estimate critical tensions on the individual bonds.[6,22] Elongational flow experiments in a cross-slot device corroborated the midchain scission of carbon-carbon bonds[23] and allowed quantitative evaluation of the rupture force in the range of 2.6-13.4 nN.[13] Recently, strength of chemical bonds has been studied by various nanoprobes that enable mechanical probing of individual molecules.[23-28] For the C-C bonds, one observed an average bond-rupture force of 2.0±0.3 nN, which is close to the elongation flow experiments and theoretical calculations.[29] The mechanochemistry of polymeric solids[30] exhibits a broader variety of reactions than in polymer solutions. This is probably due to the fact that the formed radicals remain localized and a larger number density of fractured bonds can be built up. Furthermore, bimolecular reactions, which circumvent the radical formation, were envisioned to be more readily activated than homolytic bond cleavage.[31] Mechanically induced homolytic cleavage of the C-C backbone bonds leads to the formation of two free radicals as established by electron spin resonance studies,[32-33] NMR,[34] and infrared spectroscopy.[6] The radicals may recombine

or disproportionate, react with oxygen from the air, or attack other polymer molecules. With the help of radical traps, it was quantitatively shown that each rupture event produced radicals.[35] In the absence of radical scavengers, block or graft polymers may be formed.

Research carried out during the past two decades, however, has shown that mechanical forces can be used in a more controlled fashion through the development of special macromolecules and tools that allow management of bond tension on molecular length scales. Single molecule force spectroscopy, including optical tweezers,[36-37] magnetic tweezers,[38] atomic force microscopy (AFM)[39-43] has emerged as powerful tools to investigate the forces and motions associated with biological molecules, enzyme activity and chemical reactions. AFM has been especially successfully in studying the mechanical properties of proteins[44-47] and polymers.[40,48-49] For a typical AFM pulling experiment, there are two operation modes: (i) pulling at constant loading/extension rate and (ii) pulling at constant force (force-clamp AFM).[41] Compared to constant loading/extension rate mode, force-clamp AFM allows accurate measurement of reaction rates.[50-52] On the other hand, special stressed molecules have also been designed and developed from synthetic views as a useful tool to study mechanochemistry, such as molecular force probes that are stiff stilbene based macrocyclic molecules with a function group of interest incorporated, which can generate a restoring force up to hundreds of picoNewtons,[53-54] molecular tensile machines that are highly branched macromolecular architectures capable of generating a force up to nanoNewtons along the backbones,[55-61] which will be discussed in more detail in the following section, and new types of mechanophores.[62-63] With the help of these powerful tools, mechanochemistry has been thriving during the past decade with a flurry of reports showing novel mechanochemical phenomena, including scission of specific chemical bonds,[53,58] steering of

reaction pathways,[64] changing color of materials,[4] triggering multiple reactions in a single polymer chain,[62] mechanocatalysis,[65-68] reconfiguring stereoisomers,[69] controlling spin states in transition-metal complexes,[70] mechanically induced chemiluminescence,[71] and *etc*.

1.1 Molecular tensile machines

Our contribution to the growth of mechanochemistry was the creation of macromolecular architectures, including molecular bottlebrushes,[72] pom-poms,[73] and tethered macromolecules,[74] which are able to generate bond tensions without applying an external force[55-61].

Connectivity of atoms into molecules and molecular assemblies results in a decrease of entropy and causes net tensile force in chemical bonds. Additional enhancement of the bond tension can be achieved by changing molecular architecture, *e.g.* through introduction of linear chain branches and grafts. Steric repulsion between the branches or grafts is transmitted to a covalent skeleton of a branched macromolecule and causes additional tension in their chemical bonds.[55-61] The tension depends on the branching (or grafting) density, length of the branches, and interaction with the surrounding environment (*e.g.* solvent molecules). In addition, playing with molecular architecture allows creation of macromolecules with a distribution of tension over their chemical bonds, wherein different (yet chemically identical) bonds are imposed to different tensions. This provides a unique opportunity to design molecular architectures, with a particular distribution of tension that enable focusing mechanical tension to specific chemical bonds.[59] It is possible to create the so-called molecular tensile machines that can generate bond tension without applying an external force, and also amplify and focus this tension to a chemical group of interest.[53-54,58,60]

Here, we focus on bottlebrush macromolecules. Tension is self-generated along the backbone of bottlebrush macromolecules due to steric repulsion between densely grafted side chains. Unlike flow- or cavitation-induced tension along polymer chains in typical elongational flow and ultrasonic experiments, the self-generated tension is evenly distributed along the backbone (transmission regime) except the bottlebrushes ends which are tension focusing regime (Figure 1.1).

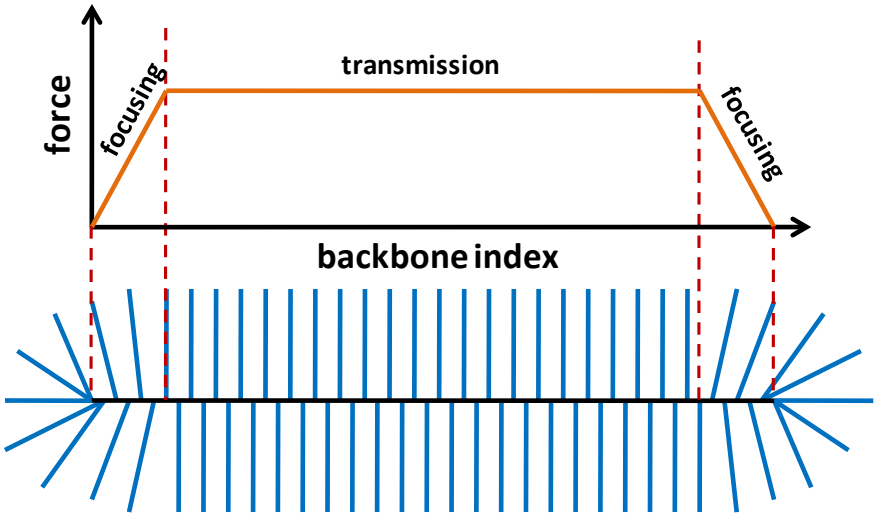

Figure 1.1 Tension is generated and accumulated at the bottlebrush end-caps and transmitted along the backbone.

Recently, we have extended the concept of molecular tensile machines further by introducing in the middle of the backbone a weak linker, which is important because any functional group of interest can be studied if synthesis is allowed. As a proof of this concept, we were able to selectively activate disulfide bond, leading to its homolytic cleavage and acceleration of its reduction by dithiothreitol.[58,60]

To study the mechanochemistry of the tensile machines, it is important to calibrate or at least estimate the self-generated tension in the backbone of bottlebrush macromolecules.

Here we investigate two different systems: bottlebrushes in dilute solutions and on substrates (Figure 1.2).

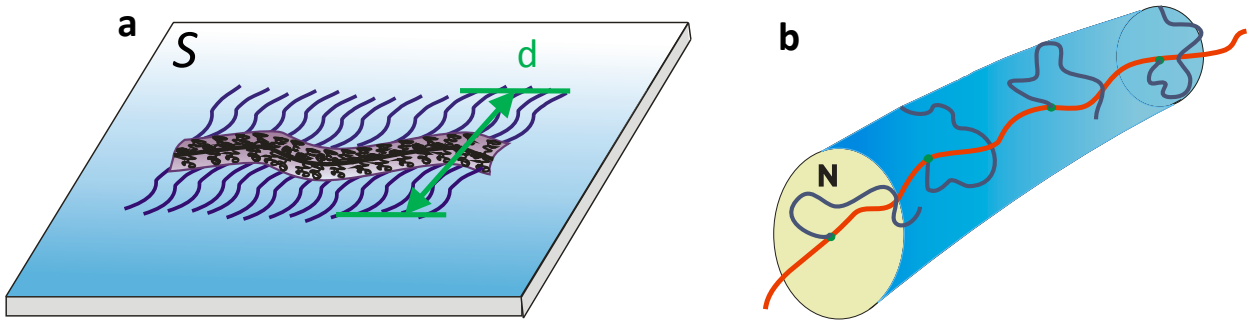

Figure 1.2 (a) a molecular bottlebrush adsorbed on substrates. *S* is its spreading coefficient on the substrate, and *d* is its width. (b) a cylindrical worm-like molecular bottlebrush with side chains of N Kuhn monomers in solutions.

On substrates, the tension along the backbone is high due to strong repulsion between adsorbed side chains at a 2D surface, which can be expressed as

$$f \cong S \cdot d \tag{1.1}$$

where d is the width of adsorbed bottlebrushes (Figure 1.1a), which is proportional to the degree of polymerization of side chains. The spreading parameter $S = \gamma_{sg} - (\gamma_{sl} + \gamma_{lg})$ is the difference between the interfacial energies for the substrate/gas (γ_{sg}), substrate/liquid (γ_{sl}), and liquid/gas (γ_{lg}) interfaces. For example, the spreading coefficient for poly(butyl acrylate) bottlebrushes on air/water interface is ~20 mN/m at room temperature, with a width (d) of 100 nm, giving a backbone tension of ~2 nN, which is large enough to break C-C bonds.[55-56,61]

In dilute solutions, the tension in the backbone is small due to weak steric repulsion between densely grafted side chains, because there is more space for the side chains in a 3D space compared to a 2D surface. The tension is given by

$$f \cong \frac{k_B T}{b} N^{\alpha} \tag{1.2}$$

where $k_B = 1.38 \times 10^{23}\, J/K$ is Boltzmann constant, T is absolute temperature, b and N are the length and number of Kuhn monomers of the side chains and α is scaling factor depending on the solvent properties, with $\alpha = 3/8$ for good solvent and $\alpha = 1/3$ for theta solvent. To give a rough idea of how large the tension is, we take molecular bottlebrushes with $b \cong 1\, nm$ and $N \cong 100$ as an example, the tension is on the order of tens of picoNewtons, which is much smaller than that on a substrate.

In the context of this dissertation, we will review two major implications of strained chemical bonds with the use of molecular tensile machines: (i) activation of chemical reactions and (ii) perturbation of the electronic structure. While sufficient amount of literature is available for the analysis of force effect on a range of chemical and biochemical reactions, there is little, almost non-existent information of the effect of mechanical tension on the electronic structure and related properties (color, fluorescence, catalytic activity, etc.).

1.2 Mechanical activation of chemical reactions

The tension effect on chemical reactions has been studied experimentally and theoretically. The questions of interest include bond life-time as a function of applied force, pathways and energetics of chemical reactions, and transient states. Experimental studies can be roughly divided into two classes: (i) mechanical interrogation of macroscopic systems (fibers, composites, films, etc.) and (ii) molecular-scale experiments (single-molecule force spectroscopy, molecular force probes). Most studies have been focused on the tension effect on kinetics of materials degradation. However, it remains challenging to relate rupture forces determined in bulk materials or solutions to the rupture forces of individual chemical bonds. Unlike macroscopic experiments, in molecular mechanochemistry one interrogates individual

molecules by applying well-defined force, deformation, and loading rate and monitoring chemical reactions directly one molecule at a time.

Witta et al. investigated the force dependent kinetics of disulfide reduction by dithiothreitol under controlled force by force-clamp atomic force microscopy (AFM) and showed that the rate constant was exponentially dependent on applied force.[50] Singh et al. also used dynamic NMR spectroscopy to study the kinetics of thiolate/disulfide interchange involving cyclic five-, six- and seven-membered disulfides and demonstrated that the interchange reaction involving penta-cyclic disulfides that experience higher tension is faster by ~10^3 than cyclic six- and seven-membered disulfides.[75] However, Kucharski and his coworkers in their work on disulfide reduction in macrocycles as a function of restoring force, have presented convincing evidence that pulling on a disulfide bond with a force up to ca. 350 picoNewton does not accelerate its reduction by thiolates.[54] A conclusion on whether force can accelerate disulfide-thiol exchange reaction exponentially or not cannot be made so far and further studies are needed. In this dissertation, we will review the effects of tension coupled with temperature on chemical reactions by answering the following questions:

- How does reaction rate constant depend on tension?
- Does tension change the potential of bonds? How is activation barrier dependent on applied tension?

1.3.1 Reaction rate theories

Chemical reactions are the basis of chemical synthesis, biological metabolism and even the change of natural environment. Any deep understanding of the processes involved must be based on a sound theory of chemical reaction dynamics. Here, we give a brief introduction

to three commonly used reaction rate theories, which are Arrhenius equation, transition state theory and Kramers theory respectively.

1.3.1.1 Arrhenius equation

The reaction rates depend on many parameters. The most important one is temperature. The Arrhenius equation is a simple but remarkably accurate empirical formula for the temperature dependence of reaction rate constant, proposed by Arrhenius in 1887,[76] which is given as:

$$k = Ae^{-E_a/k_BT} \tag{1.3}$$

The pre-exponential factor A is essentially temperature (T) independent. E_a is the activation energy, which controls the temperature dependence, and $k_B = 1.38 \times 10^{-23}\, J/K$ is the Boltzmann constant.

The Arrhenius equation has been widely used by chemist. From the measured reaction rates, A and E_a can be found by plotting $logk$ versus $1/T$ (Arrhenius plot). It works well with small experimental temperature range. Otherwise, temperature dependence of the pre-exponential factor should be taken into consideration.

1.3.1.2 Transition state theory (TST)

The Arrhenius equation derives from empirical observations and ignores any mechanistic considerations. Therefore, further development was necessary to understand the two parameters associated with this empirical equation, the pre-exponential factor and the activation energy. To address these two issues, TST, assuming a chemical equilibrium (quasi-equilibrium) between reactants and activated transition state complex, was developed by Eyring in 1935, leading to the Eyring equation.[77] The equation is given below:

$$k = \kappa \frac{k_BT}{h} e^{\Delta S_{TS}/k_B} e^{-\Delta H_{TS}/k_BT} \tag{1.4}$$

where ΔH_{TS} and ΔS_{TS} are the enthalpy and entropy differences between transition state complex and reactants respectively, κ is the transmission coefficient ($\kappa < 1$) and $h = 6.63 \times 10^{-34} Js$ is Planck constant. The term $\frac{k_B T}{h}$ is called attempt frequency, which represents the frequency of the vibrational mode responsible for converting the activated transition state complex to the product. However, each attempt does not necessarily yield the product due to some effects, such as steric hindrance and adsorption to a surface. That is why the transmission coefficient is introduced to account for these effects.

1.3.1.3 Kramers theory

Five years after the development of TST (the Eyring equation), Kramers treated a simple model of a chemical reaction, namely the escape of a particle from a potential well through the shuttling action of Brownian motion, elucidating the applicability of TST.[78]

In his model, the effect of friction, depending on viscosity, on the reaction rate constant is discussed in detail. But in this dissertation, we are not going deep into Kramers theory. Instead, the main conclusions are described:

(1) At low friction (energy-diffusion regime), the reaction rate constant is proportional to friction.

(2) At high friction (spatial-diffusion regime), the reaction rate constant is proportional to the reciprocal of friction.

(3) Although TST predicts the upper limits of Kramers theory, in the wide range of intermediate friction, TST gives reasonable results within ~10% error.

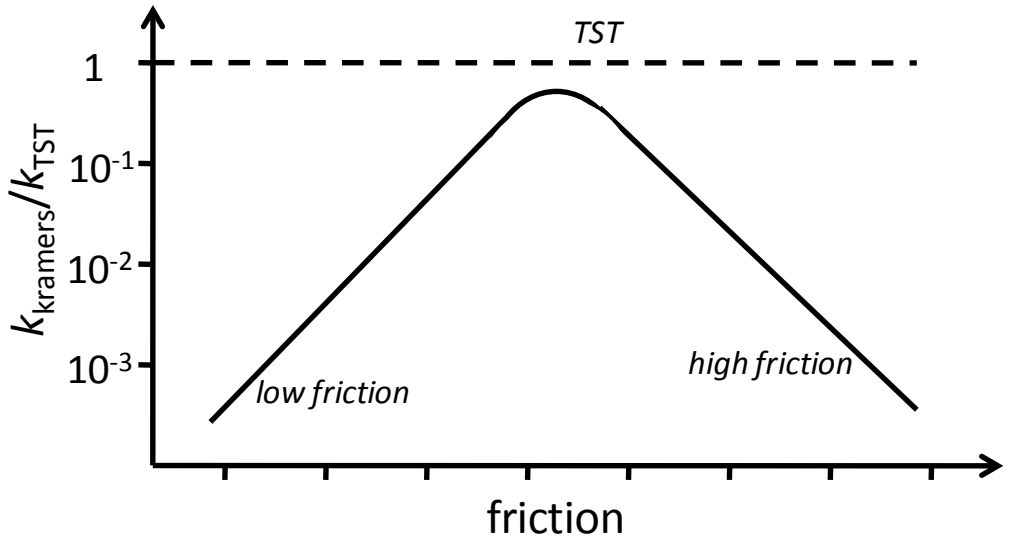

Figure 1.3 General behavior of the ratio of rate constants predicted by Kramers theory and TST, plotted in log-log scale.

Kramers theory becomes more and more popular among biologists, because in biological systems, most chemical reactions take place in viscous medium, and their reaction rates are usually slower than those predicted by TST. Indeed, experiments have shown that viscosity affects, for instance, enzyme reactions[79] and the binding of ligands to heme proteins.[80] To evaluate the effect of viscosity, Kramers theory is usually employed. The reader is encouraged to pursue reviews articles for more details.[81-82]

In the abovementioned three reaction theories, force is not taken into account. However, for a mechanically activated chemical reaction, force may change its pathway and energetics. Thus, the theories should be modified to include the effects of force, as will be shown in Chapter 3.

1.3.2 Monitoring reactions by AFM imaging

Thirty years ago, the development of scanning probe microscopy (SPM) revolutionized the scientific world by providing a technique capable of visualizing both conductive and

insulating materials at the nanometer scale and probing their properties,[83-84] in contrast to scanning tunneling microscopy (STM) that is limited to imaging of conductive materials.[85] In particular, atomic force microscopy (AFM), developed in 1986 by Binnig *et. al.*,[86] is one of the most successful SPMs, allowing for 3D visualization and analysis of a variety of materials under various environmental conditions.[87-91] Besides imaging, another major application of AFM is force spectroscopy,[43] which is not discussed here.

In addition to biological specimens, AFM has been recently applied to imaging synthetic macromolecules. The first convincing examples of visualization of synthetic single polymer chains by AFM were showed by Kumaki *et. al.* in 1996.[92] However, reliable and accurate imaging of conventional polymer chains is hindered by their small lateral dimensions (<0.5 nm) and high flexibility characterized by short persistence lengths on the order of 1 nm. Molecular imaging can be greatly enhanced by grafting polymer chains with bulky side groups or chains, which is ascribed to both backbone extension and separation of the backbones due to enhancement of steric repulsion between adsorbed side chains on substrates (Figure 1.4).

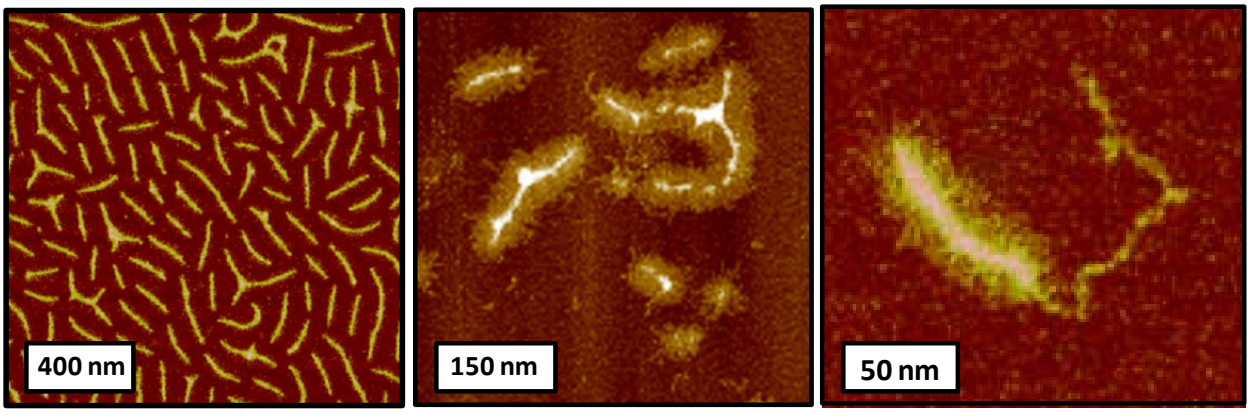

Figure 1.4 AFM height images of bottlebrush molecules: dense polymer bottlebrush monolayer transferred from air/water interface to mica substrate, left; polymer bottlebrushes on mica prepared by spin casting, middle; a polymer bottlebrush with a linear polymer tail, right.

Molecular imaging can serve as a supplementary method to characterize macromolecules, providing information beyond simple visualization (*e.g.* size, composition, and chain topology), in addition to classic methods such as gel permeation chromatography (GPC), nuclear magnetic resonance (NMR) spectroscopy and scattering techniques that measure average information. The advantage of molecular visualization of single polymers is to allow direct correlation between polymer synthesis and visual observation. It is a powerful tool to study the structures and conformation of polymers,[93-96] the flow of polymer films[97-99] and supramolecular self-assembly.[100] Combined with Langmuir-Blodgett (LB) technique, molecular imaging by AFM allows measurement of number average molecular weight of bottlebrush polymers.[101] With the development of techniques, now AFM can even discriminate individual chemical bonds.[102-103]

In this dissertation, we will show that AFM can be also employed to monitor the reaction of molecular tensile machines. Every scission of bond in the bottlebrush backbone yields two brush molecules, leading to the decrease of average contour length of the bottlebrushes. The measurement of reaction rate by AFM is based on its correlation with the evolution of average contour length, which will be discussed in detail in Chapter 3.

1.4 Mechanochromism

The phenomenon that materials change color upon mechanical stress is termed Mechanochromism, which has potential applications in pressure or stress sensors. The mechanisms for tension induced color/spectroscopic change vary from case to case. Weder et al. have done pioneer work on the photoluminescent character change of polymer blends upon mechanical deformation.[104-105] In this case, the color change was attributed to the dissociation of dye aggregates by mechanic force. In another example, bulk polymers with

mechanophores (spiropyran) links incorporated into the networks change color upon stretching, involving the ring-opening reaction of spiropyran to form merocyanine with C-O bond rupture.[4] Reneker et al. showed that tension induced cis to trans conformation change of azobenzene could also result in the change of color.[106] However, in all these three examples, the bonds, including length and angle, might be deformed due to tension, which could also affect the color/spectroscopic change. Unfortunately, the effect of bond deformation was neglected, and there is little, almost non-existent information of the effect of mechanical tension on the electronic structure and related properties (color, fluorescence, catalytic activity, etc.).

To understand this effect, we have used molecular tensile machines that are bottlebrush molecules with full polythiophene backbone to study its fluorescence under tension, which will be discussed in detail in Chapter 4. Thus it is necessary to give a brief introduction to fluorescence here.

Photoluminescence is a process in which susceptible molecules emit light from electronically excited states created by absorption of ultraviolet or visible light photons, which is divided into two categories, fluorescence and phosphorescence, depending on the electronic configuration of the excited state and the emission pathway. Phosphorescence is a similar process to fluorescence, but involves intersystem crossing between singlet states where the spin is paired and excited triplet states where the spin is no longer paired due to "forbidden" spin transition, which will not be discussed here.

The fluorescence process consists of three important events (Figure 1.5), all of which occur on different time scales. A susceptible molecule is excited from the ground state S_0 (S stands for singlet state) to the excited single state (S_1) by absorbing an incoming photon,

which happens in femtoseconds (10^{-15} s). Then the excited state electron relaxes from higher vibrational energy level to the lowest vibrational energy level in the excited singlet state on the timescale of picoseconds (10^{-12} s). Finally, the excited molecule returns to the ground accompanied by emission of a longer wavelength photon, which occurs in a relatively long time period of nanoseconds (10^{-9} s). The energies of the absorbed and emitted photons have to match the energy differences between initial and final states of each transition, expressed by Planck's Law,

$$E = h\nu = hc/\lambda \tag{1.5}$$

where E is the energy, ν and λ are the frequency and wavelength of the photon, and c is the speed of light.

Franck-Condon principle provides a selection rule for the relative probability of vibronic transitions,[107] which is related to fluorescence absorption and emission intensities. The probability of a transition from the ground state (S_0) to the excited singlet state (S_1) depends on the degree of similarity between the vibrational and rotational energy states when an electron resides in the ground state versus those present in the excited state as showed in Figure 1.5. The higher the similarity is, the higher probability the transition has. Both excitation transition (blue line) and emission transition (green line) occur in such short timeframes that the internuclear distance associated with the bonding orbitals does not have enough time to change, and thus the transitions are represented as vertical lines.

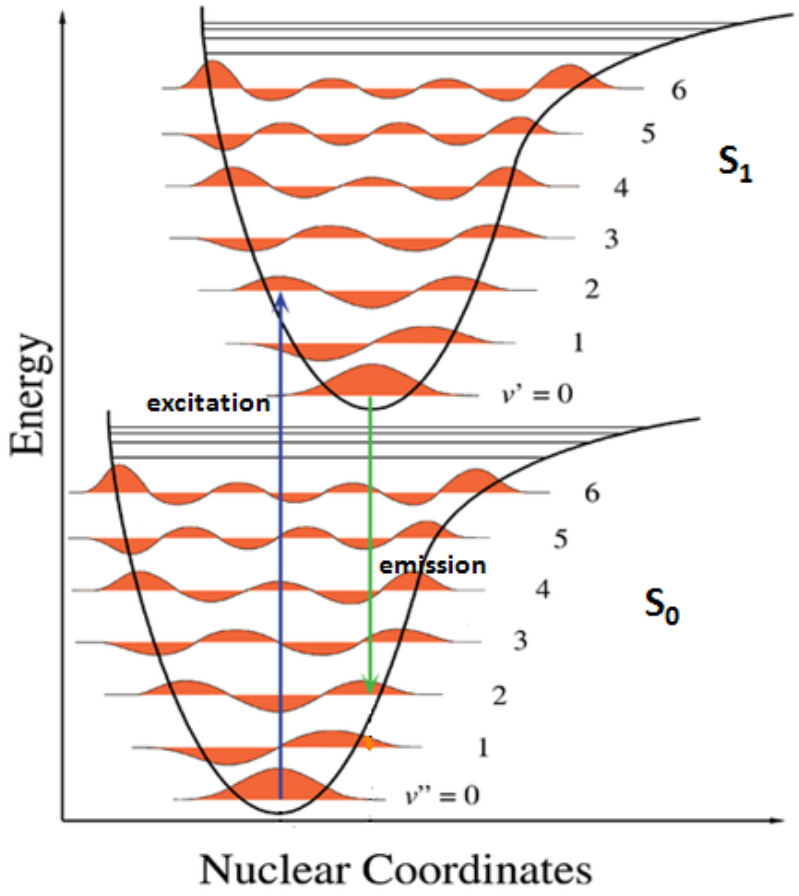

Figure 1.5 Fluorescence process described by Franck-Condon principle energy diagram.[108]

Knowing the basis of fluorescence, we have been able to extract some valuable information about electronic structures of polythiophene backbone from its fluorescence spectra with respect to applied tension, e.g., energy band gap, as shown in Chapter 4.

1.5 Outline of dissertation: goals and accomplishments

The next chapter (Chapter 2) of the dissertation describes the experimental methods, including synthesis, sample preparation, molecular imaging and analysis, and fluorescence spectroscopy.

Chapter 3 and 4 are focused on the fundamental study of mechanochemistry with the help of molecular tensile machines. In Chapter 3, the effects of tension on the scission of disulfide

bonds, through homolytic cleavage and reduction by dithiothreitol will be presented. In Chapter 4, the investigation of tension effect on the electronic structures of polythiophene by fluorescence spectroscopy will be presented.

In Chapter 5, collaborative work on synthesis of bottlebrush macromolecules and self-assembly via H-bonding will be presented.

Chapter 6 is to conclude and provides directions for future work.

References

(1) Beyer, M. K.; Clausen-Schaumann, H. *Chem. Rev.* **2005**, *105*, 2921-2948.

(2) Vladimir, V. B. *Russian Chemical Reviews* **2006**, *75*, 177.

(3) Caruso, M. M.; Davis, D. A.; Shen, Q.; Odom, S. A.; Sottos, N. R.; White, S. R.; Moore, J. S. *Chem. Rev.* **2009**, *109*, 5755-5798.

(4) Davis, D. A.; Hamilton, A.; Yang, J.; Cremar, L. D.; Van Gough, D.; Potisek, S. L.; Ong, M. T.; Braun, P. V.; Martinez, T. J.; White, S. R.; Moore, J. S.; Sottos, N. R. *Nature* **2009**, *459*, 68-72.

(5) Ribas-Arino, J.; Marx, D. *Chem. Rev.* **2012**.

(6) Harrington, R. E.; Zimm, B. H. *The Journal of Physical Chemistry* **1965**, *69*, 161-175.

(7) Boldyrev, V. V. *Ultrasonics Sonochemistry* **1995**, *2*, S143-S145.

(8) Nguyen, T. Q.; Liang, Q. Z.; Kausch, H.-H. *Polymer* **1997**, *38*, 3783-3793.

(9) Jellinek, H. H. G. *Degradation of Vinyl Polymers*; Academic Press: New York, 1955.

(10) Porter, R. S.; Johnson, J. F. *The Journal of Physical Chemistry* **1959**, *63*, 202-205.

(11) Nguyen, T.; Kausch, H.-H. In *Macromolecules: Synthesis, Order and Advanced Properties*; Springer Berlin Heidelberg: 1992; Vol. 100/1, p 73-182.

(12) Casale, A. *Journal of Applied Polymer Science* **1975**, *19*, 1461-1473.

(13) Odell, J. A.; Keller, A. *Journal of Polymer Science Part B: Polymer Physics* **1986**, *24*, 1889-1916.

(14) Watson, W. F. *Die Makromolekulare Chemie* **1959**, *34*, 240-252.

(15) Sohma, J. *Progress in Polymer Science* **1989**, *14*, 451-596.

(16) Zhurkov, S. N.; Korsukov, V. E. *Journal of Polymer Science: Polymer Physics Edition* **1974**, *12*, 385-398.

(17) Frenkel, J. *Acta Physicochim U.R.S.S.* **1944**, *19*, 51-76.

(18) Nguyen, T. Q.; Kausch, H. H. *Macromolecules* **1990**, *23*, 5137-5145.

(19) Buchholz, B. A.; Zahn, J. M.; Kenward, M.; Slater, G. W.; Barron, A. E. *Polymer* **2004**, *45*, 1223-1234.

(20) Kuijpers, M. W. A.; Iedema, P. D.; Kemmere, M. F.; Keurentjes, J. T. F. *Polymer* **2004**, *45*, 6461-6467.

(21) Sivalingam, G.; Agarwal, N.; Madras, G. *AIChE Journal* **2004**, *50*, 2258-2265.

(22) Odell, J. A.; Muller, A. J.; Narh, K. A.; Keller, A. *Macromolecules* **1990**, *23*, 3092-3103.

(23) Krüger, D.; Fuchs, H.; Rousseau, R.; Marx, D.; Parrinello, M. *Phys Rev Lett* **2002**, *89*, 186402-186402.

(24) Grandbois, M.; Beyer, M.; Rief, M.; Clausen-Schaumann, H.; Gaub, H. E. *Science* **1999**, *283*, 1727-1730.

(25) Conti, M.; Falini, G.; Samorì, B. *Angewandte Chemie* **2000**, *112*, 221-224.

(26) Schmitt, L.; Ludwig, M.; Gaub, H. E.; Tampé, R. *Biophysical Journal* **2000**, *78*, 3275-3285.

(27) Kienberger, F.; Kada, G.; Gruber, H. J.; Pastushenko, V. P.; Riener, C.; Trieb, M.; Knaus, H.-G.; Schindler, H.; Hinterdorfer, P. *Single Molecules* **2000**, *1*, 59-65.

(28) Skulason, H.; Frisbie, C. D. *J. Am. Chem. Soc.* **2002**, *124*, 15125-15133.

(29) Beyer, M. K. *J. Chem. Phys.* **2000**, *112*, 7307-7312.

(30) Zhurkov, S. N. *Int J Fract* **1984**, *26*, 295-307.

(31) Tabata, M.; Yamakawa, H.; Takahashi, K.; Sohma, J. *Polymer Degradation and Stability* **1979**, *1*, 57-68.

(32) Devries, K. L.; Roylance, D. K.; Williams, M. L. *Journal of Polymer Science Part A-1: Polymer Chemistry* **1970**, *8*, 237-252.

(33) Kondo, S.-i.; Sasai, Y.; Hosaka, S.; Ishikawa, T.; Kuzuya, M. *Journal of Polymer Science Part A: Polymer Chemistry* **2004**, *42*, 4161-4167.

(34) Kolbert, A. C.; Didier, J. G.; Xu, L. *Macromolecules* **1996**, *29*, 8591-8598.

(35) Ayrey, G.; Moore, C. G.; Watson, W. F. *Journal of Polymer Science* **1956**, *19*, 1-15.

(36) Grier, D. G. *Nature* **2003**, *424*, 810.

(37) Moffitt, J. R.; Chemla, Y. R.; Smith, S. B.; Bustamante, C. *Annu, Rev. Biochem* **2008**, *77*, 205-228.

(38) Zlatanova, J.; Leuba, S. H. *Biochemistry & Cell Biology* **2003**, *81*, 151.

(39) Florin, E.; Moy, V.; Gaub, H. *Science* **1994**, *264*, 415-417.

(40) Rief, M.; Oesterhelt, F.; Heymann, B.; Gaub, H. E. *Science* **1997**, *275*, 1295-1297.

(41) Oberhauser, A. F.; Hansma, P. K.; Carrion-Vazquez, M.; Fernandez, J. M. *Proc. Natl. Acad. Sci. USA* **2001**, *98*, 468-472.

(42) Liang, J.; Fernández, J. M. *ACS Nano* **2009**, *3*, 1628-1645.

(43) Neuman, K. C.; Nagy, A. *Nature Methods* **2008**, *5*, 491-505.

(44) Rief, M.; Gautel, M.; Oesterhelt, F.; Fernandez, J. M.; Gaub, H. E. *Science* **1997**, *276*, 1109-1112.

(45) Carrion-Vazquez, M.; Oberhauser, A. F.; Fowler, S. B.; Marszalek, P. E.; Broedel, S. E.; Clarke, J.; Fernandez, J. M. *Proceedings of the National Academy of Sciences* **1999**, *96*, 3694-3699.

(46) Carrion-Vazquez, M.; Marszalek, P. E.; Oberhauser, A. F.; Fernandez, J. M. *Proceedings of the National Academy of Sciences* **1999**, *96*, 11288-11292.

(47) Oberhauser, A. F.; Marszalek, P. E.; Carrion-Vazquez, M.; Fernandez, J. M. *Nature Structural Biology* **1999**, *6*, 1025-1028.

(48) Wu, D.; Lenhardt, J. M.; Black, A. L.; Akhremitchev, B. B.; Craig, S. L. *J. Am. Chem. Soc.* **2010**, *132*, 15936-15938.

(49) Schmidt, S. W.; Kersch, A.; Beyer, M. K.; Clausen-Schaumann, H. *Physical Chemistry Chemical Physics* **2011**, *13*, 5994-5999.

(50) Wiita, A. P.; Ainavarapu, S. R. K.; Huang, H. H.; Fernandez, J. M. *Proc. Natl. Acad. Sci. USA* **2006**, *103*, 7222-7227.

(51) Wiita, A. P.; Perez-Jimenez, R.; Walther, K. A.; Grater, F.; Berne, B. J.; Holmgren, A.; Sanchez-Ruiz, J. M.; Fernandez, J. M. *Nature* **2007**, *450*, 124-127.

(52) Liang, J.; Fernández, J. M. *J. Am. Chem. Soc.* **2011**, *133*, 3528-3534.

(53) Yang, Q.-Z.; Huang, Z.; Kucharski, T. J.; Khvostichenko, D.; Chen, J.; Boulatov, R. *Nature Nano.* **2009**, *4*, 302-306.

(54) Kucharski, T. J.; Huang, Z.; Yang, Q.-Z.; Tian, Y.; Rubin, N. C.; Concepcion, C. D.; Boulatov, R. *Angew. Chem., Int. Ed.* **2009**, *48*, 7040-7043.

(55) Sheiko, S. S.; Sun, F. C.; Randall, A.; Shirvanyants, D.; Rubinstein, M.; Lee, H.-i.; Matyjaszewski, K. *Nature* **2006**, *440*, 191-194.

(56) Lebedeva, N. V.; Sun, F. C.; Lee, H.-i.; Matyjaszewski, K.; Sheiko, S. S. *J. Am. Chem. Soc.* **2008**, *130*, 4228-4229.

(57) Park, I.; Shirvanyants, D.; Nese, A.; Matyjaszewski, K.; Rubinstein, M.; Sheiko, S. S. *J. Am. Chem. Soc.* **2010**, *132*, 12487-12491.

(58) Park, I.; Sheiko, S. S.; Nese, A.; Matyjaszewski, K. *Macromolecules* **2009**, *42*, 1805-1807.

(59) Park, I.; Nese, A.; Pietrasik, J.; Matyjaszewski, K.; Sheiko, S. S. *J. Mater. Chem.* **2011**, *21*, 8448-8453.

(60) Li, Y.; Nese, A.; Lebedeva, N. V.; Davis, T.; Matyjaszewski, K.; Sheiko, S. S. *J. Am. Chem. Soc.* **2011**, *133*, 17479-17484.

(61) Lebedeva, N. V.; Nese, A.; Sun, F. C.; Matyjaszewski, K.; Sheiko, S. S. *Proc. Natl. Acad. Sci. USA* **2012**, *109*, 9276-9280.

(62) Lenhardt, J. M.; Black, A. L.; Craig, S. L. *J. Am. Chem. Soc.* **2009**, *131*, 10818-10819.

(63) Kean, Z. S.; Ramirez, A. L. B.; Craig, S. L. *Journal of Polymer Science Part A: Polymer Chemistry* **2012**, *50*, 3481-3484.

(64) Hickenboth, C. R.; Moore, J. S.; White, S. R.; Sottos, N. R.; Baudry, J.; Wilson, S. R. *Nature* **2007**, *446*, 423-427.

(65) van Leeuwen, P. W. N. M.; Kamer, P. C. J.; Reek, J. N. H.; Dierkes, P. *Chem. Rev.* **2000**, *100*, 2741-2770.

(66) Piermattei, A.; Karthikeyan, S.; Sijbesma, R. P. *Nat Chem* **2009**, *1*, 133-137.

(67) Tennyson, A. G.; Wiggins, K. M.; Bielawski, C. W. *J. Am. Chem. Soc.* **2010**, *132*, 16631-16636.

(68) Alegre-Cebollada, J.; Perez-Jimenez, R.; Kosuri, P.; Fernandez, J. M. *J. Biol. Chem* **2010**, *285*, 18961-18966.

(69) Wiggins, K. M.; Hudnall, T. W.; Shen, Q.; Kryger, M. J.; Moore, J. S.; Bielawski, C. W. *J. Am. Chem. Soc.* **2010**, *132*, 3256-3257.

(70) Parks, J. J.; Champagne, A. R.; Costi, T. A.; Shum, W. W.; Pasupathy, A. N.; Neuscamman, E.; Flores-Torres, S.; Cornaglia, P. S.; Aligia, A. A.; Balseiro, C. A.; Chan, G. K.-L.; Abruna, H. D.; Ralph, D. C. *Science* **2010**, *328*, 1370-1373.

(71) Chen, Y.; Spiering, A. J. H.; KarthikeyanS; Peters, G. W. M.; Meijer, E. W.; Sijbesma, R. P. *Nat Chem* **2012**, *4*, 559-562.

(72) Panyukov, S.; Zhulina, E. B.; Sheiko, S. S.; Randall, G. C.; Brock, J.; Rubinstein, M. *J. Phys. Chem. B* **2009**, *113*, 3750-3768.

(73) Panyukov, S. V.; Sheiko, S. S.; Rubinstein, M. *Phys. Rev. Lett.* **2009**, *102*, 148301.

(74) Sheiko, S. S.; Panyukov, S.; Rubinstein, M. *Macromolecules* **2011**, *44*, 4520-4529.

(75) Singh, R.; Whitesides, G. M. *J. Am. Chem. Soc.* **1990**, *112*, 6304-6309.

(76) Arrhenius, S. *Z. Phys. Chem.* **1889**, *4*, 226.

(77) Wynne-Jones, W. F. K.; Eyring, H. *J. Chem. Phys.* **1935**, *3*, 492-502.

(78) Kramers, H. A. *Physica* **1940**, *7*, 284-304.

(79) Gavish, B.; Werber, M. M. *Biochemistry* **1979**, *18*, 1269-1275.

(80) Beece, D.; Eisenstein, L.; Frauenfelder, H.; Good, D.; Marden, M. C.; Reinisch, L.; Reynolds, A. H.; Sorensen, L. B.; Yue, K. T. *Biochemistry* **1980**, *19*, 5147-5157.

(81) Hänggi, P.; Talkner, P.; Borkovec, M. *Rev. Mod. Phys.* **1990**, *62*, 251-341.

(82) Pollak, E.; Talkner, P. *Chaos* **2005**, *15*, 026116.

(83) Bottomley, L. A. *Analytical Chemistry* **1998**, *70*, 425-476.

(84) Hansma, H. G.; Pietrasanta, L. *Current Opinion in Chemical Biology* **1998**, *2*, 579-584.

(85) Binnig, G.; Rohrer, H.; Gerber, C.; Weibel, E. *Phys. Rev. Lett.* **1982**, *49*, 57-61.

(86) Binnig, G.; Quate, C. F.; Gerber, C. *Phys. Rev. Lett.* **1986**, *56*, 930-933.

(87) Ratcliff, G. C.; Erie, D. A.; Superfine, R. *Applied Physics Letters* **1998**, *72*, 1911-1913.

(88) Sheiko, S. S.; Möller, M. *Chem. Rev.* **2001**, *101*, 4099-4124.

(89) Shi, D.; Somlyo, A. V.; Somlyo, A. P.; Shao, Z. *Journal of Microscopy* **2001**, *201*, 377-382.

(90) Gromer, A.; Rawiso, M.; Maaloum, M. *Langmuir* **2008**, *24*, 8950-8953.

(91) Mantelli, S.; Muller, P.; Harlepp, S.; Maaloum, M. *Soft Matter* **2011**, *7*, 3412-3416.

(92) Kumaki, J.; Nishikawa, Y.; Hashimoto, T. *J. Am. Chem. Soc.* **1996**, *118*, 3321-3322.

(93) Sun, F.; Sheiko, S. S.; Möller, M.; Beers, K.; Matyjaszewski, K. *The Journal of Physical Chemistry A* **2004**, *108*, 9682-9686.

(94) Sun, F. C.; Dobrynin, A. V.; Shirvanyants, D.; Lee, H.-I.; Matyjaszewski, K.; Rubinstein, G. J.; Rubinstein, M.; Sheiko, S. S. *Phys. Rev. Lett.* **2007**, *99*, 137801.

(95) Yu-Su, S. Y.; Sheiko, S. S.; Lee, H.-i.; Jakubowski, W.; Nese, A.; Matyjaszewski, K.; Anokhin, D.; Ivanov, D. A. *Macromolecules* **2009**, *42*, 9008-9017.

(96) Yu-Su, S. Y.; Sun, F. C.; Sheiko, S. S.; Konkolewicz, D.; Lee, H.-i.; Matyjaszewski, K. *Macromolecules* **2011**, *44*, 5928-5936.

(97) Xu, H.; Shirvanyants, D.; Beers, K.; Matyjaszewski, K.; Rubinstein, M.; Sheiko, S. S. *Phys. Rev. Lett.* **2004**, *93*, 206103.

(98) Xu, H.; Sun, F. C.; Shirvanyants, D. G.; Rubinstein, M.; Shabratov, D.; Beers, K. L.; Matyjaszewski, K.; Sheiko, S. S. *Advanced Materials* **2007**, *19*, 2930-2934.

(99) Barrett, M. J.; Sun, F. C.; Nese, A.; Matyjaszewski, K.; Carrillo, J.-M. Y.; Dobrynin, A. V.; Sheiko, S. S. *Langmuir* **2010**, *26*, 15339-15344.

(100) Qin, S.; Matyjaszewski, K.; Xu, H.; Sheiko, S. S. *Macromolecules* **2003**, *36*, 605-612.

(101) Sheiko, S. S.; da Silva, M.; Shirvaniants, D.; LaRue, I.; Prokhorova, S.; Moeller, M.; Beers, K.; Matyjaszewski, K. *J. Am. Chem. Soc.* **2003**, *125*, 6725-6728.

(102) Gross, L.; Mohn, F.; Liljeroth, P.; Repp, J.; Giessibl, F. J.; Meyer, G. *Science* **2009**, *324*, 1428-1431.

(103) Gross, L.; Mohn, F.; Moll, N.; Schuler, B.; Criado, A.; Guitián, E.; Peña, D.; Gourdon, A.; Meyer, G. *Science* **2012**, *337*, 1326-1329.

(104) Löwe, C.; Weder, C. *Advanced Materials* **2002**, *14*, 1625-1629.

(105) Crenshaw, B. R.; Weder, C. *Chemistry of Materials* **2003**, *15*, 4717-4724.

(106) Reneker, D. H.; Mattice, W. L.; Quirk, R. P.; Kim, S. J. *Smart Materials and Structures* **1992**, *1*, 84.

(107) Franck, J.; Dymond, E. G. *Transactions of the Faraday Society* **1926**, *21*, 536-542.

(108) Wikipedia; Wikimedia Foundation, Inc.: 2012.

Chapter 2

Experimental Methods

2.1 Synthesis of strained macromolecules with tension probes

The bottlebrush macromolecules as molecular tensile machines used to study mechanochemistry in this work were synthesized in Professor Matyjaszewski's group at Carnegie Mellon University using atom transfer radical polymerization (ATRP).[1-5] ATRP is an example of controlled/living radical polymerization (CRP) techniques, which can be used to polymerize a variety of monomers. The basic principle of ATRP is the equilibrium between active species and dominant species through a reversible redox process of active species catalyzed by a transition metal complex. One of the advantages of ATRP (or other CRP) is good control of distributions of molecular weight, i.e. a low polydispersity index (PDI). Since a polymer's properties, such as modulus, viscosity, solubility, and diffusion coefficient, are affected by its molecular size and PDI, it becomes important to keep molecular weight distribution as narrow as possible.

As an example, the synthetic outline for bottlebrush molecules with a disulfide linker in the center of the backbone is shown in Figure 2.1. The synthesis of the bottlebrush molecules consists of two steps: (i) synthesis of macroinitiator and (ii) grafting of side chains from the macroinitiator. To insert the disulfide bond in the center of the backbone, a diinitiator with one bromide at each end was used to initiate the polymerization. The bromide atom reversibly bound to a catalyst forming a radical at a polymer chain end, which enabled the

addition of monomers leading to the growth of the polymer chain. However, the bromide atom would rebind to the chain end, thus temporarily deactivating the reaction site and starting the process over again. After polymerization was finished, the polymers were bromized through the deprotection of trimethylsilyloxy groups, yielding the macroinitiators. N-butyl acrylate monomers were then grafted from the macroinitiators by ATRP to grow side chains, giving the final product.

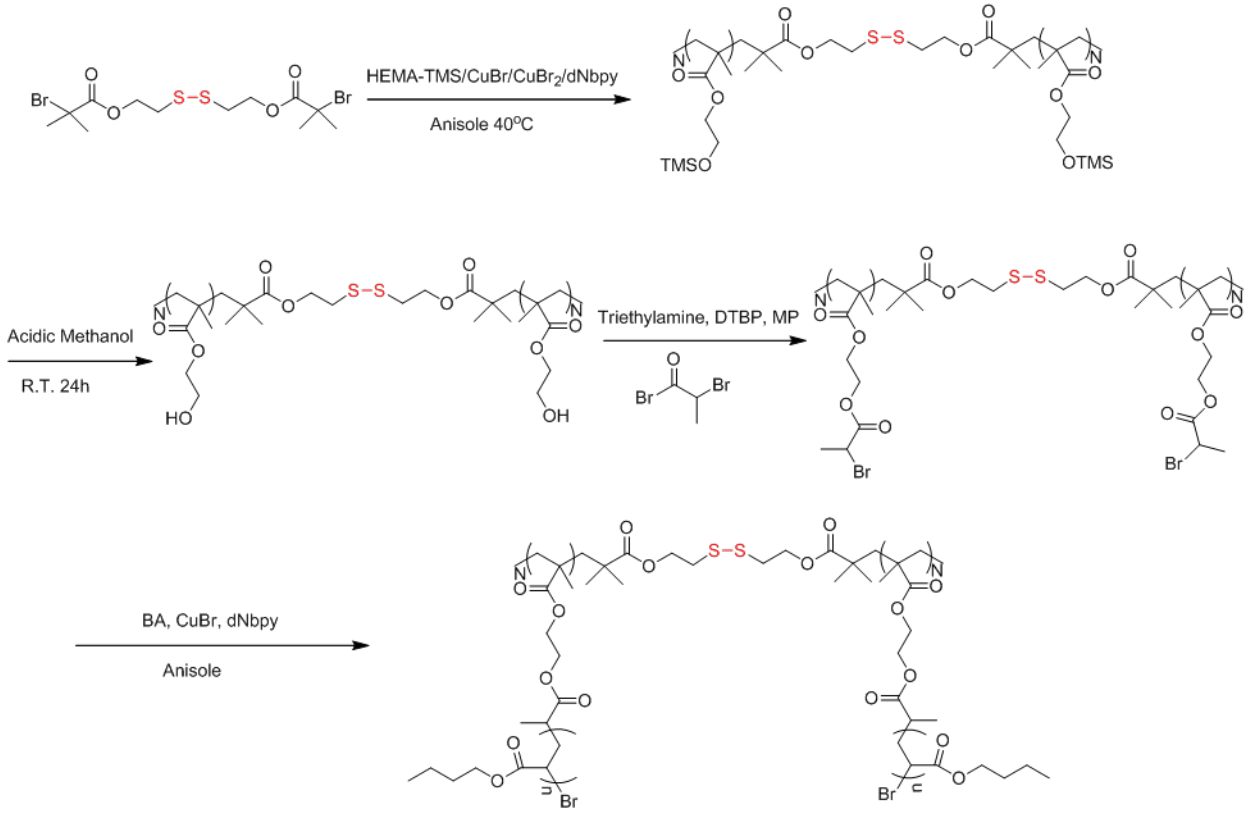

Figure 2.1 Synthetic outline for the molecular bottlebrush with a disulfide bond in the center of its backbone.

2.2 Molecular imaging by AFM

2.2.1 Sample preparation

Sample preparation is crucial to molecular imaging experiments. To be visualized by AFM, single molecules were deposited onto solid substrates, such as mica and highly

oriented pyrolytic graphite (HOPG). Two film preparation techniques were employed: spincasting and Langmuir-Blodgett (LB) film deposition.

Spincasting is usually used to prepare either dilute, single molecule films or thick polymer films, which involves dispersing a solution of polymers onto a substrate as it is spinning at a constant velocity. Figure 2.2 shows how a typical spin coater works. Solution concentration and spin rate are two important factors that can affect the density of film and structure/conformation of single polymer chains. The choice of substrates is also important. Mica is one of the widely used substrates due to its atomically flat surface and low cost, and does a good job in most cases. However, it fails when the attraction between polymer molecules and mica (hydrophilic) is weak and aggregation is favored, e.g. polystyrene. In this case, hydrophobic substrates should be considered, e.g. HOPG.

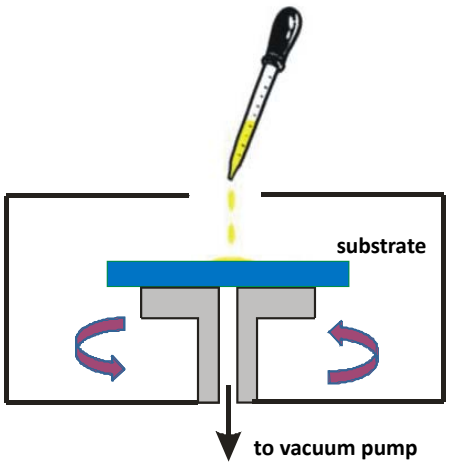

Figure 2.2 spincasting: sample molecules are dispersed on a substrate while spinning.

LB deposition is another important method for transferring films from a liquid substrate to a solid one. It is can be used to prepare both monolayer and multilayer films. The LB trough works by compressing a known quantity of molecules within a confined surface area between two physical barriers (Figure 2.3), thus controlling their surface pressure.[6] No other

techniques (e.g. sputter coating, thermal evaporation and molecular epitaxy)[7] can offer such uniform control over the thickness of the film, the number of layers , or its surface pressure.

To prepare a LB film, a solution of the molecule in a volatile liquid is deposited drop wise onto a liquid substrate, typically water, as the subphase contained in a trough made of Teflon. This creates a floating layer of the molecules, which is then compressed by the barriers in a controlled manner to get a uniform film. The surface pressure of the film is monitored by a Wilhelmy plate, which is a vertical plate hanging from a balance that measures buoyancy force supplied by the surface and film. The film can be transferred onto a solid substrate, such as mica, silicon, or glass, keeping the surface pressure constant, *i.e.* film uniformity upon transfer. This is important because one can use imaging techniques such as AFM to study the freshly prepared film. Indeed, the combination of LB technique and AFM imaging allow measurement of number average molecular weight bottlebrush polymers.[8]

In this body of work, LB trough was also used as a "reactor" and "tension amplifier" for molecular tensile machines (*i.e.* molecular bottlebrushes). The tension and reactant concentration can be finely tuned by controlling the composition of the subphase or the surface pressure.[9] After a certain period of reaction time, the bottlebrush molecules were transferred to mica substrates for AFM imaging.

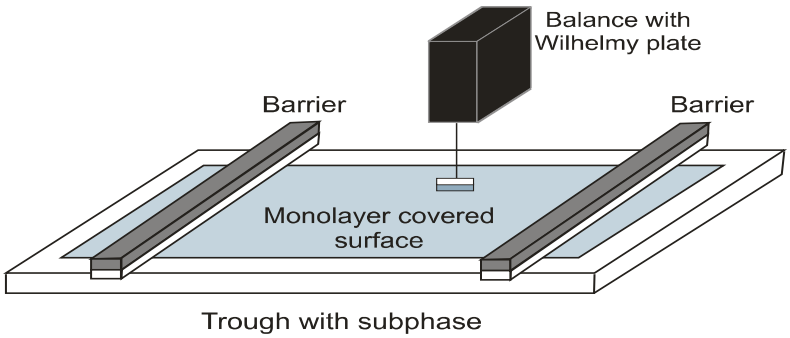

Figure 2.3 typical Langmuir-Blodgett trough set-up.

2.2.2 Imaging by AFM and image analysis

The AFM consists of 3 major components: the probe tip, the detection system, and the scanning peizo (Figure 2.4). The probe tip is the sensor that collects the force information by interacting with the local force fields of the sample under study. It consists of a very sharp tip on the edge of a cantilever which deflects upon attraction or repulsion from the surface. This tip can be constructed of a variety of materials such as silicon, silicon nitride, tungsten, and carbon nanotubes. A laser is focused onto the back side of the cantilever and is directed towards a quad photo detector which can measure the deflection of the laser as the cantilever moves. The sample is controlled by a sensitive peizo system that scans the sample underneath the tip with nanometer precision.

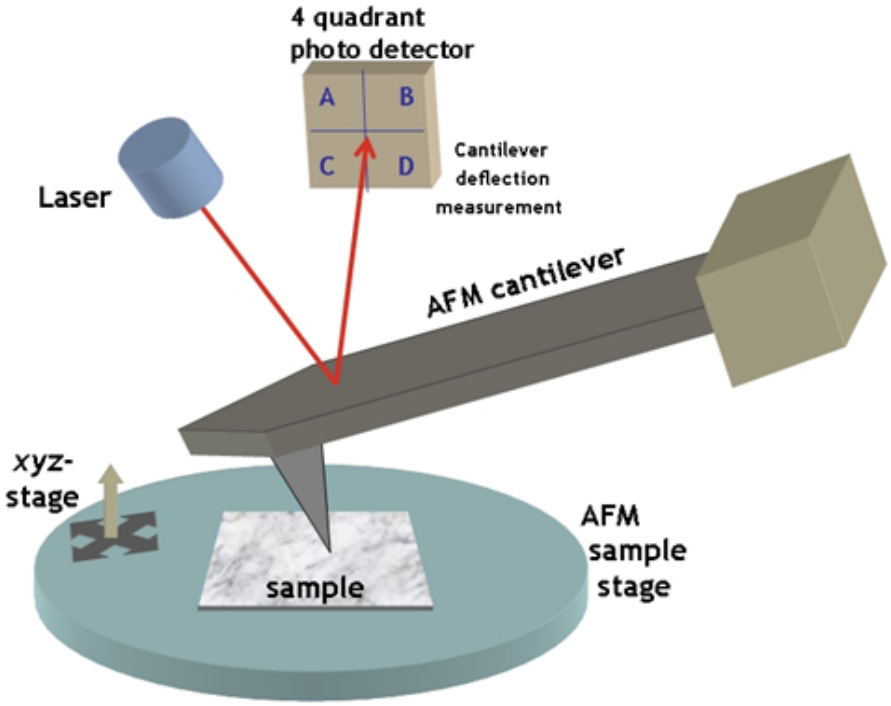

Figure 2.4 Atomic force microscope.

In our experiments we operated the AFM in PeakForce QNM mode that produces height images and quantitative nano-mechanical sample property images at the same time. PeakForce QNM consists two parts: (i) the PeakForce tapping part is the feedback mode used to track and image the sample surface and produce force curves while scanning; (ii) the QNM part uses the force curves to extract quantitative material properties data and construct sample property images. Unlike tapping mode where the feedback loop keeps the cantilever vibration amplitude constant, PeakForce tapping controls the maximum force (Peak Force) on the tip. This protects the tip and sample from damage while allowing tip-sample contact area to be minimized. Although PeakForce tapping does not allow phase mapping as tapping mode does, it can provide much more sample property images, such as modulus, adhesion, deformation and dissipation. Another advantage of PeakForce tapping over tapping mode is that one does not need to tune the cantilever, which makes the operation simpler and easier.

Image analysis was performed using an in-house developed program known as “PEN” that allows identification of individual molecules and tracing their contours. Once the contours are traced the program can automatically extract a large wealth of quantitative data, such as end-to-end distance, radius of gyration, contour length, bond angle, and more.

2.3 Molecular-fluorescence spectroscopy

To study the effect of tension on electronic structure, a molecular-fluorescence spectroscopy setup was built to measure the fluorescence spectra of bottlebrush molecules with polythiophene backbones adsorbed on a liquid substrate.

This spectroscopy setup consists of five major components: a laser source, a microscope, a Langmuir-Blodgett trough, a spectrograph and a CCD camera (Figure 2.5). The laser (405 nm) is used to excite the polythiophene backbones in molecular bottlebrushes that are

deposited on a liquid substrate in the LB trough. The tension can be tuned by controlling surface pressure of the film and composition of the subphase. The microscope, with excitation and emission filter set incorporated into the light path, is used to focus the excitation light on the sample molecules on the liquid substrate and collect the emitted light. The fluorescence emission light is then separated by the spectrograph into a frequency spectrum that is finally recorded by the CCD camera.

There is one major technique issue involved during a typical measurement, that is, the fluorescence intensity is low due to the two facts: (i) only a small number of molecules are excited on a 2D surface and (ii) the side chains of the bottlebrush molecules even dilute the fluorescent polythiophene backbones. To address this issue, a low magnification objective (10X) is used to focus on a larger surface area on the substrate for both excitation and emission processes.

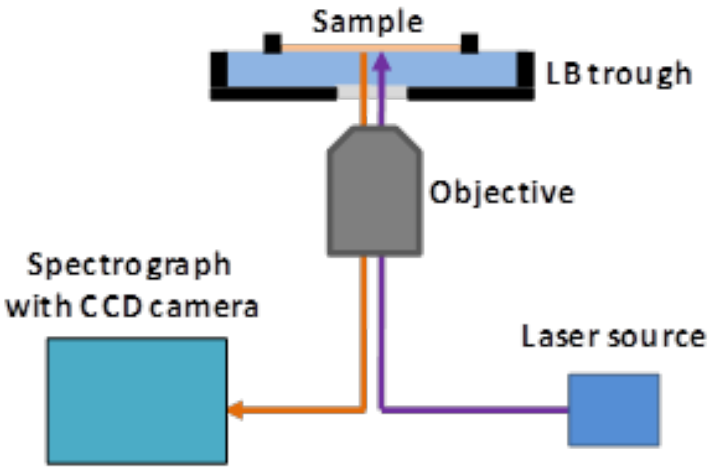

Figure 2.5 Schematic representation of molecular-fluorescence spectroscopy.

References

(1) Matyjaszewski, K.; Xia, J. *Chem. Rev.* 2001, *101*, 2921-2990.

(2) Pakula, T.; Zhang, Y.; Matyjaszewski, K.; Lee, H.-i.; Boerner, H.; Qin, S.; Berry, G. C. *Polymer* 2006, *47*, 7198-7206.

(3) Sheiko, S. S.; Sumerlin, B. S.; Matyjaszewski, K. *Prog. Polym. Sci.* 2008, *33*, 759-785.

(4) Lee, H.-i.; Pietrasik, J.; Sheiko, S. S.; Matyjaszewski, K. *Prog. Polym. Sci.* 2010, *35*, 24-44.

(5) Matyjaszewski, K. *Macromolecules* 2012, *45*, 4015-4039.

(6) Langmuir, I. *J. Am. Chem. Soc.* 1917, *39*, 1848-1906.

(7) Petty, M. C. *Thin Solid Films* 1992, *210–211, Part 2*, 417-426.

(8) Sheiko, S. S.; da Silva, M.; Shirvaniants, D.; LaRue, I.; Prokhorova, S.; Moeller, M.; Beers, K.; Matyjaszewski, K. *J. Am. Chem. Soc.* 2003, *125*, 6725-6728.

(9) Lebedeva, N. V.; Sun, F. C.; Lee, H.-i.; Matyjaszewski, K.; Sheiko, S. S. *J. Am. Chem. Soc.* 2008, *130*, 4228-4229.

Chapter 3

Kinetics of Bond Scission in Strained Macromolecules

3.1 Introduction

Mechanochemistry is a growing field and has been thriving during the past decade with the help of development of special macromolecules and tools that allow management of bond tension on molecular length scales.[1-4] It has been shown that mechanical force can break specific bonds,[5-6] steer reaction pathways,[7] control spin states in transition-metal complexes,[8] trap diradical transition states,[9] and *etc*.[10-14] In spite of the discovery of these novel mechanochemical phenomena, the effect of tension of tension on chemical reactions is not clear so far though it has been studied experimentally and theoretically for decades of years.[15-17] So, further study is absolutely in need.

Our contribution to the growth of mechanochemistry was the creation of macromolecular architectures that are able to generate bond tensions without applying an external force.[6,18-23] Connectivity of atoms into molecules and molecular assemblies results in a decrease of entropy and causes net tensile force in chemical bonds. Additional enhancement of the bond tension can be achieved by changing molecular architecture, *e.g.* through introduction of linear chain branches and grafts. Steric repulsion between the branches or grafts is transmitted to a covalent skeleton of a branched macromolecule and causes additional tension in their chemical bonds.[6,18-23] The tension depends on the branching (or grafting) density, length of the branches, and interaction with the surrounding environment (*e.g.* solvent molecules). In addition, playing with molecular architecture allows creation of

macromolecules with a distribution of tension over their chemical bonds, wherein different (yet chemically identical) bonds are imposed to different tensions. This provides a unique opportunity to design molecular architectures, with a particular distribution of tension that enable focusing mechanical tension to specific chemical bonds.[21] It is possible to create the so-called molecular tensile machines that can generate bond tension without applying an external force, and also amplify and focus this tension to a chemical group of interest.[5-6,17,22]

Here, we will apply this concept to study the mechanical activation of disulfide bonds that play a vital role in many life systems, especially in protein folding and unfolding.[24-26] A single disulfide bond was incorporated into the center of bottlebrush backbone. Upon adsorption onto a liquid substrate, the tension along the backbone can be amplified to nanoNewtons. Both the homolytic scission of disulfide (first-order reaction) and the reduction disulfide by dithiothreitol (DTT) (second-order reaction) were studied. The reactions were followed by monitoring the average contour length of the molecular bottlebrushes using atomic force microscopy (AFM). The experimental approach based on molecular imaging is unique as it allows monitoring reactions for a large ensemble of individual macromolecules subjected to identical, yet, tunable mechanical and thermal conditions.[27-29] This capability combines the advantages of single molecule probes and macroscopic tensile machines by offering respectively well-defined bond-tension distributions and representative statistics of bond-rupture events. For homolytic scission, we exploited the effects of bond tension and surrounding temperature on the lifetime of disulfide bond. While analysis of the effect of tension is a well-established procedure,[30-33] the effect of temperature on a mechanochemical process is a more complex task.[23,34] Temperature exhibits multiple effects, including (i) change of the thermal energy (k_BT), (ii) change of the pre-

exponential factor,[35-36] and also change of bond tension (force).[23] Here we have attempted to sort out these individual contributions to the rate constant of bond scission, and have shown that the temperature effect on force has a dominant role, which accounts for the anti-Arrhenius scission kinetics. In the case of reduction of disulfide by DTT, the reaction kinetics was studied as a function of bond tension and DTT concentration. The reduction rate is linearly dependent on DTT concentration, indicating a second order reaction, and exponentially dependent on the tension applied to disulfide bond.

3.2 Experimental section

3.2.1 Materials and sample preparation

The bottlebrush macromolecules with a disulfide bond in the middle of the backbone were synthesized by ATRP.[6,37-41] The polymer bottlebrush consists of a poly(2-hydroxyethyl methacrylate) backbone and poly(n-butyl acrylate) (PBA) side chains (Figure 3.1). A combination of molecular characterization techniques (GPC, LS, gravimetric analysis, and AFM) was employed to measure the number-average degree of polymerization (DP) of the brush backbone and side chains, which was reported somewhere else.[6] Two bottlebrush molecules were prepared with the same backbone (N=650), but different side chain lengths (n=60, 130 respectively). The bottlebrush molecules with n=130 were used for the study of homolytic scission, while in the reduction experiments, the bottlebrush molecules with n=60 were used. Dithiothreitol **(**DTT) (99%) was purchased from Acros Organics, Inc.

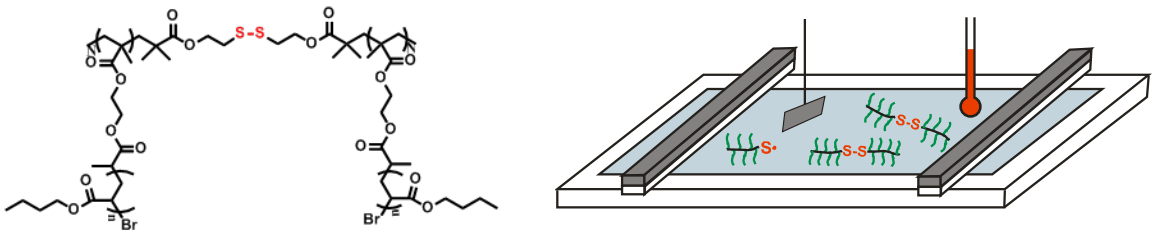

Figure 3.1 Chemical structure of the bottlebrush molecules with N=650 and n=130 (left); Langmuir-Blodgett experiment set-up, where the reactions were carried out (right).

3.2.2 Controlling bond tension in Langmuir-Blodgett monolayers

The bottlebrush macromolecules were adsorbed from a dilute solution in chloroform onto a surface of water/2-propanol mixtures in a Langmuir-Blodgett trough (KSV-5000 instrument equipped with a Wilhelmy plate balance). Mixing water (Milli-Q double-distilled, ρ=18.2 MΩ) and 2-propanol (Aldrich, 99%) allowed accurate ($\pm$0.1 mN/m) control of the spreading parameter of the macromolecules. The measurements were performed under controlled vapor pressure of propanol to minimize the effect of solvent evaporation on the spreading parameter. The temperature was controlled through circulation of a thermostated liquid around the trough and independently monitored by a set of thermocouples placed at the water/2-propanol surface. The accuracy of the temperature measurements was $\pm$ 0.5 *K*. In disulfide reduction experiments, DTT was added to the subphase (2-propanol/water mixture). After different exposure times (time spent on air/water-propanol interface), the monolayer films were transferred from the air/water interface to freshly cleaved mica substrates at a constant pressure of 0.5 mN/m for AFM analysis.

3.2.3 Molecular imaging by AFM

Topographic images of individual molecules were collected using a multimode Atomic Force Microscopy (Bruker) with NanoScope V controller in PeakForce tapping mode.[27] We used silicon cantilevers with a resonance frequency of about 50-90 kHz and a spring constant of about 0.4 N/m. The analysis of digital images was performed using a custom software program (PEN) developed in-house. The length distributions were obtained from two

3μm×3μm AFM images, including more than 600 molecules to ensure a relative standard deviation of the mean below 4%.

3.3 Homolytic scission of disulfide bonds

Our results are presented in two sections. First, we report the effects of temperature and tension on bond scission rate constant. Second, we analyze the measured data and evaluate the potential of disulfide bond quantitatively. Note that scission of C-C and S-S bonds can occur simultaneously in the studied systems but on different time scales. Since the scission rate of C-C and C-S bonds is at least one order of magnitude lower than the rate of the S-S scission,[6] we conducted our experiments within shorter period of time at lower bond tensions to suppress scission of C-C and C-S bonds, and thus the observed chain scission is ascribed to mid-chain scission of disulfide bonds (Appendix I). The bond tension was controlled by using higher 2-propnaol concentration (0.4-0.8 wt. %) of water/2-propanol mixtures as substrates on which the spreading parameter of bottlebrush macromolecules is smaller.[19] The change of bond tension due to 2-propanol evaporation can be neglected within experimental time (< 2h).[22]

3.3.1 Anti-Arrhenius scission

Every scission of disulfide bond yields two molecular bottlebrushes of half length. As showed in Figure 3.2, bimodal length distributions were observed, represented by two bands at L≅320 nm and L/2≅160 nm that correspond respectively to i) the full length of bottlebrushes with the intact disulfide linker and ii) monosulfide bottlebrushes due to mid-chain scission of the disulfide linker.[6]

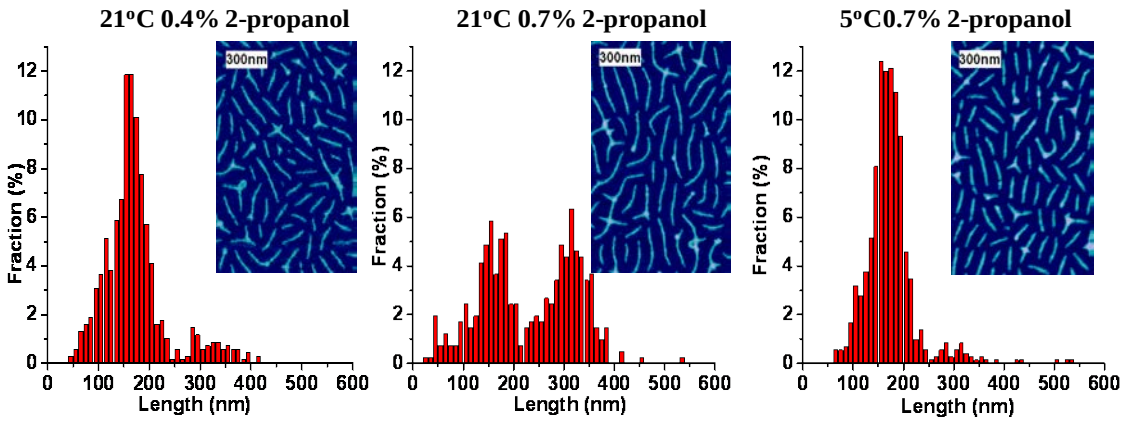

Figure 3.2 Length distributions along with AFM height micrographs of the bottlebrush macromolecules captured after exposure of 15 minutes to 0.4% 2-propanol (21°C), 0.7% 2-propanol (21°C), and 0.7% 2-propanol (5°C) substrates respectively.

Molecular imaging allows monitoring the scission process for a large ensemble of individual macromolecules subjected to identical, yet, tunable mechanical and thermal conditions,[27-29] and offers two complementary methods for quantitative analysis of the kinetics of bond scission. The first method is based on counting the number of molecules per unit area, since the increase in number of molecules is equivalent to the number of ruptured bonds (Appendix II). This method is appropriate for mid-chain scission, resulting in a bimodal distribution with clearly separated distribution bands (Figure 3.2). The second method that is used in this work is based on measuring the number average contour length (L) of the molecular bottlebrushes which decreases upon scission. Both methods are accurate, yet, the first method should take into account an ill-defined variation in the molecular area due to separation of ruptured bottlebrushes. Therefore, we based our analysis on monitoring the length distribution of the imaged macromolecules as a function of time.

To derive the relation between the number of molecules and their number average contour length we consider a system of bottlebrushes, where $[S-S]$ is the number of

bottlebrush macromolecules with intact disulfide bonds at time t and Γ_0 is the number of brush macromolecules with intact S-S bonds in the as prepared sample (prior to deposition on the substrate). We define the number fraction of brush macromolecules with intact S-S bonds (Φ) as below:

$$\Phi(t) \equiv [S-S]/\Gamma_0 \tag{3.1}$$

At the onset of monitoring of the scission process ($t=0$), the initial fraction of disulfides is given by

$$\Phi_0 = [S-S]_0/\Gamma_0 \tag{3.2}$$

where $[S-S]_0$ is the number of disulfides at $t = 0$. Note that $\Gamma_0 \neq [S-S]_0$ as shown in Figure 3.3. Combination of eq. 3.1 and 3.2 yields

$$\frac{\Phi(t)}{\Phi_0} = \frac{[S-S]}{[S-S]_0} \tag{3.3}$$

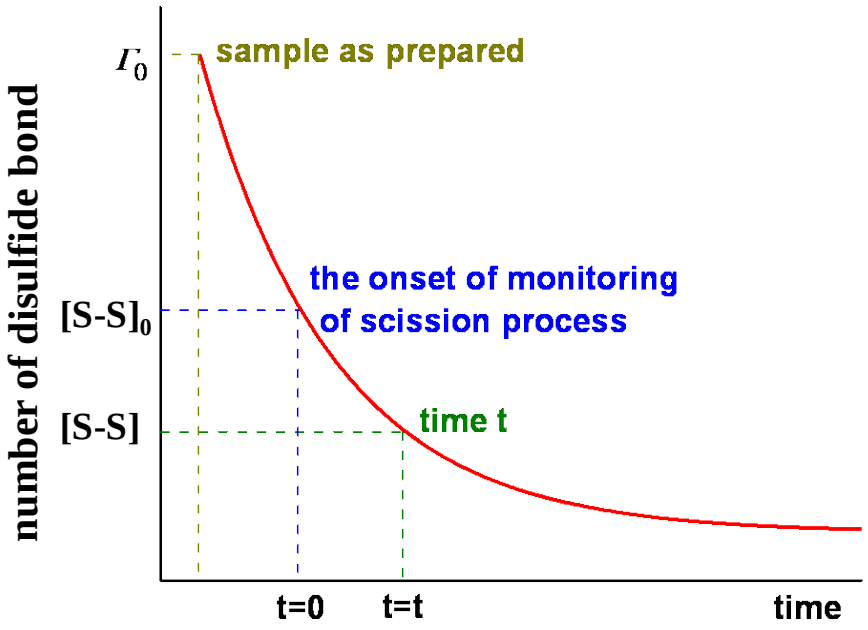

Figure 3.3 Number of disulfide bond versus time.

Since every scission of disulfide bond generates two shorter bottlebrush molecules, at any given moment, the number average contour length of bottlebrush molecules is related to the fraction of bottlebrush molecules with intact disulfide bonds (Φ) as

$$L = \frac{L_1 \cdot 2(1-\Phi)+L_2\Phi}{2(1-\Phi)+\Phi} = \frac{2L_1}{2-\Phi} \tag{3.4}$$

where L_1 is the molecular length resulted from mid-chain scission of the disulfide bond and L_2 is the average contour length of bottlebrush macromolecules with a disulfide linker. Assuming $L_2 = 2L_1$ and $L_1 = L_\infty$ for mid-chain scission (L_∞ is the average contour length at infinite time), eq. 3.4 gives

$$L(t) = \frac{2L_\infty}{2-\Phi} \tag{3.5}$$

and

$$L_0 = \frac{2L_\infty}{2-\Phi_0} \tag{3.6}$$

where L_0 is the average contour length at *t=0*.

By substituting eq. 3.5 and eq. 3.6 into eq. 3.3, one obtains the general relationship between the average contour length and the number of disulfide bonds as

$$\left(\frac{1}{L}-\frac{1}{L_\infty}\right)/\left(\frac{1}{L_0}-\frac{1}{L_\infty}\right) = \frac{[S-S]}{[S-S]_0} \tag{3.7}$$

Considering the homolytic scission of disulfide is a first-order reaction, one can obtain the following relation,

$$\frac{[S-S]}{[S-S]_0} = e^{-kt} \tag{3.8}$$

where *k* is the rate constant. Substituting eq. 3.7 into eq. 3.8, we can get the time dependence of average contour length as

$$\left(\frac{1}{L}-\frac{1}{L_\infty}\right)/\left(\frac{1}{L_0}-\frac{1}{L_\infty}\right) = e^{-kt} \tag{3.9}$$

L_∞ was determined to be $161 \pm 2\,nm$, which did not decrease within experiment time anymore and agrees with the bimodal length distribution. For each data set, the initial time ($t = 0$) was assigned to the first collected data point. Eq. 3.9 was used to fit the experimental data points in Figure 3.4 (a and b).

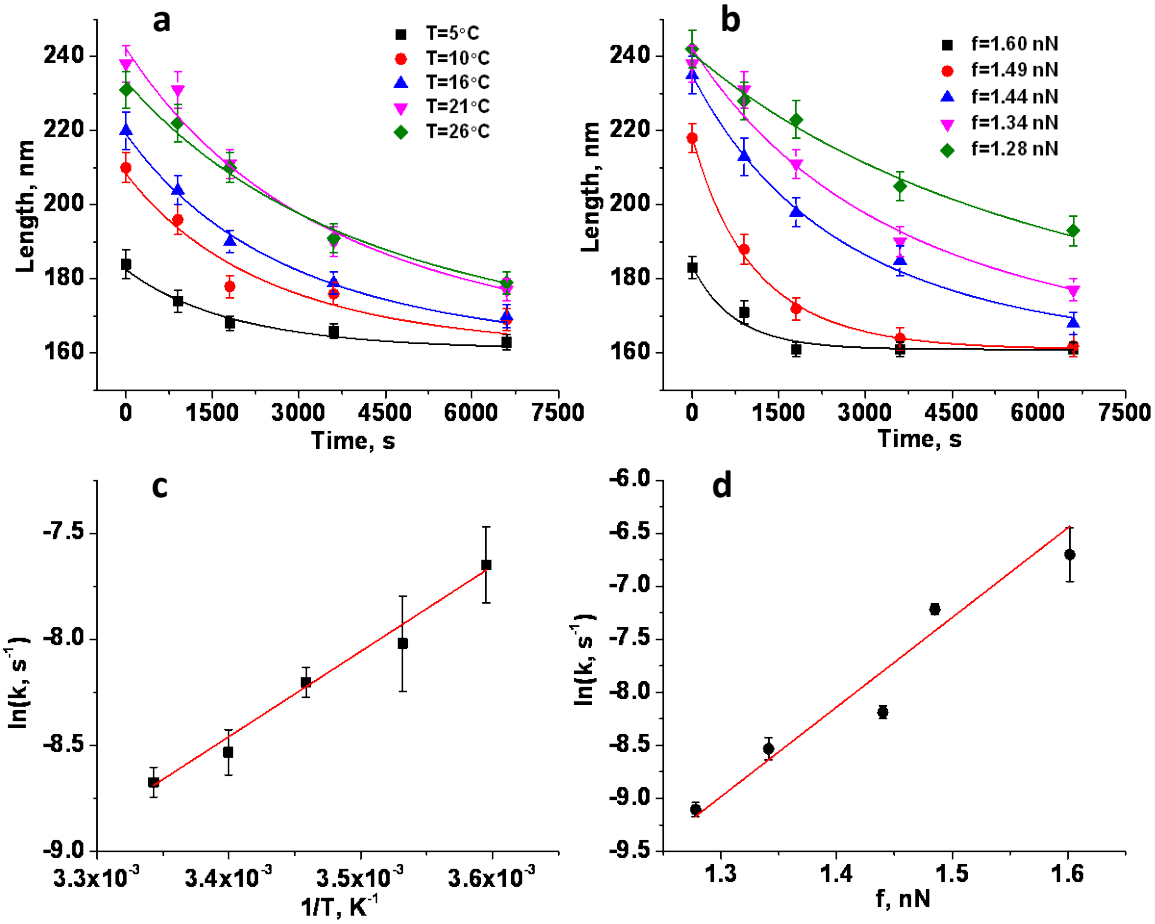

Figure 3.4 (a) Kinetics of the disulfide bond scission at various temperatures on the same substrate (0.7% 2-propanol). Solid lines are generated by fitting the data points with eq. 3.9. (b) Kinetics of the disulfide bond scission on water/2-propanol substrates of different 2-propanol concentrations (0.4% (■); 0.5% (●); 0.6% (▲); 0.7% (▼); 0.8% (♦)) at the same temperature $T_0 = 21$℃. Solid lines are generated by fitting the data points with eq. 3.9. (c) Linear fit of rate constant (ln*k*) as as a function of 1/T with the fitting equation $lnk = (4.02 \pm 0.31) \times \frac{10^3}{T} - (22.1 \pm 1.0)$. (d) Linear fit of rate constant (ln*k*) as a function of force at $T_0 = 21$℃ with the fitting equation $lnk = (8.44 \pm 1.65)\, f - (20.0 \pm 2.4)$.

As shown previously,[18] the backbone tension in adsorbed molecular bottlebrushes increases linearly with the spreading parameter *S* as

$$f \cong Sd \tag{3.10}$$

where *d* is the width of adsorbed bottlebrushes, which was determined as an average distance between worm-like macromolecules in AFM micrographs of Langmuir-Blodgett monolayers prepared at a transfer ratio of 98%. The spreading parameter $S = \gamma_{sg} - (\gamma_{sl} + \gamma_{lg})$ is the difference between the interfacial energies for the substrate/gas (sg), substrate/liquid (sl), and liquid/gas (lg) interfaces. In our experiments, the substrate corresponds to the water/2-propanol subphase, the liquid is a melt of PBA side chains, and the gas is air. The spreading parameter was independently measured through the use of a Langmuir balance as a function of the propanol concentration and temperature (Figure 3.4). On 0.7% 2-propanol solution substrate at $T_0 = 21℃$, we measured $d \cong 90\,nm$ and $S \cong 14.9\,mN/m$, which give a backbone tension of $f \cong 1.34\,nN$.

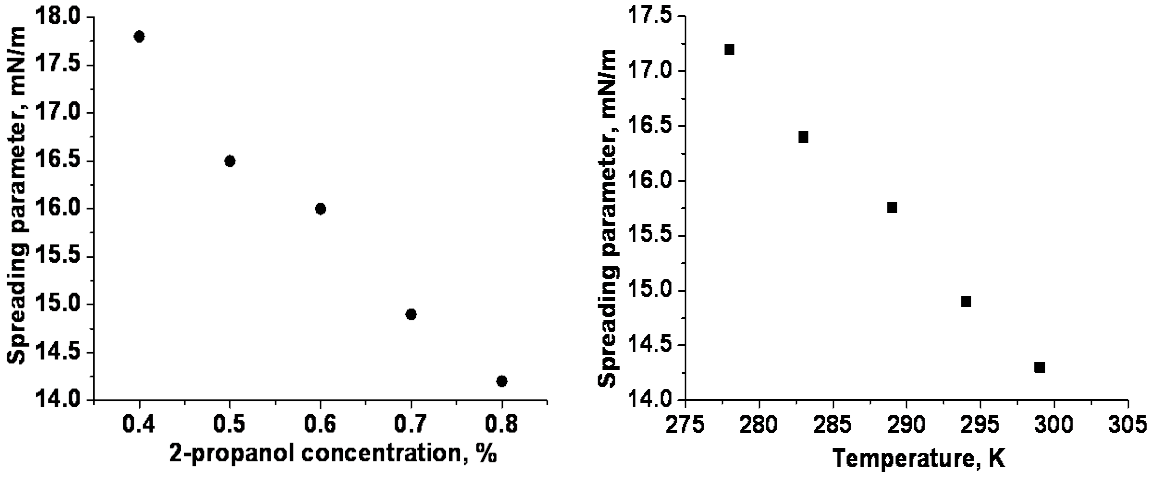

Figure 3.5 spreading parameter of the bottlebrushes molecules as a function of (a) 2-propanol concentration and (b) temperature.

The obtained rate constants are plotted as a function of reciprocal temperature ($1/T$) (Figure 3.4c) and force (Figure 3.4d) respectively. The semi-log plot of $ln\, k(1/T)$ clearly demonstrates the anti–Arrhenius behavior as the rate constant decreases with temperature, and the plot of $ln\, k(f)$ confirms the exponential dependence of force as reported previously.[16,30,42-43] The anti-Arrhenius effect is ascribed to a decrease of spreading parameter with temperature (Figure 3.5b), leading to the corresponding decrease of backbone tension (Figure 3.6), which can overpower thermal effect. Within the studied temperature range from $278K$ to $299K$, the backbone tension can be approximated as

$$f = a - bT \tag{3.11}$$

where $a = 4.99 \pm 0.14\ nN$ and $b = 0.0124 \pm 0.0005\ nN/K$.

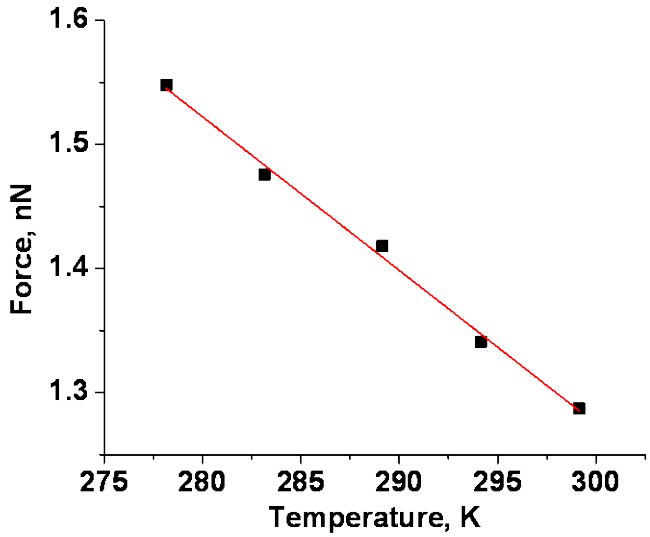

Figure 3.6 Backbone tension in adsorbed bottlebrushes on 0.7% 2-propanol aqueous solution substrate decreases with temperature. The solid line is a linear fit with eq. 3.11.

3.3.2 Data analysis.

In this section, to verify the effect of temperature, we will conduct comparative analysis of the scission kinetics of disulfide bond by two different models: (i) Bell equation, proposed

by Eyring, Zhurkov, and Bell *et al* for various force-activated bond-scission reactions;[30-31,42-43] (ii) transition state theory (TST) with Morse potential.

Bell equation In this case, the force-dependent rate constant of the scission reaction can be described by a phenomenological equation,

$$k = Ae^{-(E_a - f\Delta x)/k_B T} \tag{3.12}$$

where A is temperature (T) independent pre-exponential factor, E_a is activation energy, f is applied force, Δx is activation length (the distance from equilibrium state to transition state along the reaction coordinate), and $k_B = 1.38 \times 10^{23}\ J/K$ is Boltzmann constant. Note that in this model Δx is independent of force. One can obtain the following equations regarding Δx and E_a by taking derivative of logarithm of eq. 3.12 with respect to $1/T$ and f respectively:

$$\frac{\partial lnk}{\partial(1/T)} = -\frac{E_a - a\Delta x}{k_B} \tag{3.13}$$

$$\left(\frac{\partial lnk}{\partial f}\right)_{T_0} = \frac{\Delta x}{k_B T_0} \tag{3.14}$$

From the slopes in Figure 3.4c and 3.4d, we determine $\Delta x = 0.34 \pm 0.07$ Å and $E_a = 69 \pm 24$ kJ/mol. If we perform extrapolation to zero force, the pre-exponential factor is estimated to be on the order of $10^4\ s^{-1}$. The determined Δx value agrees with that from theoretical calculations.[44] Compared to disulfide bond dissociation energy of thiuram disulfides in solution (100~130*kJ/mol*),[45] the obtained value (E_a) is in moderate agreement, yet smaller. This could be due to two facts: (i) in our system the reaction was performed at air/water interface; (ii) bond potential depends on force,[23,32] which will be discussed below. The estimated pre-exponential factor is well below the nominal frequency of attempts $\nu = k_B T/h \cong 10^{12}\ s^{-1}$, where $h = 6.63 \times 10^{-34} Js$ is Planck constant. This could be due to

underestimation of dissociation energy and conformational and packing constraints of the backbone.[23]

TST with Morse potential Considering a disulfide bond under a constant uniaxial force *f*, the effective potential can be written as a function of reaction coordinate *x*:

$$V = V_0(1 - e^{-\beta x})^2 - fx \tag{3.15}$$

where the first term $V_b = V_0(1 - e^{-\beta x})^2$ is a cumulative Morse potential of unperturbed bond. The parameters β^{-1} and V_0 determine the width and depth of the potential well respectively. The second term corresponds to the mechanical work of force. To quantitatively analyze temperature effect on the pre-exponential factor, here we introduce TST, the rate constant can be expressed by the Eyring equation,[35]

$$k_{TST} = \kappa \frac{k_B T}{h} e^{\Delta S_{TS}/k_B} e^{-\Delta V_{TS}/k_B T} \tag{3.16}$$

where the energy barrier $\Delta V_{TS} = V(x_{TS}) - V(x_0)$ is the energy difference between transition state ($x = x_{TS}$) and equilibrium state ($x = x_0$), $\Delta S_{TS} = S(x_{TS}) - S(x_0)$ is entropy difference, κ is the transmission coefficient ($\kappa < 1$), and $\kappa \frac{k_B T}{h} e^{\Delta S_{TS}/k_B} = A$ is the pre-exponential factor.

By taking the derivative of eq. 3.15 one finds two local extrema that yield the following relations for the height ΔV_{TS} and width Δx_{TS} of the activation energy barrier as a function of force:

$$\Delta V_{TS} = V_0\sqrt{1 - f/f_m} - f\Delta x_{TS} \tag{3.17}$$

$$\Delta x_{TS} = \frac{V_0}{2f_m} ln \frac{1+\sqrt{1-f/f_m}}{1-\sqrt{1-f/f_m}} \tag{3.18}$$

where $f_m = (\partial V_b/\partial x)_{max} = \beta V_0/2$ is the maximum bond tension. Here we can see that Δx_{TS} depends on applied force.

To analyze the rate constant data, we rewrite eq. 3.16 in the logarithmic form (eq. 3.19) and re-plot Figure 3.4c and d as $\ln(k/T)$ versus $1/T$ and f respectively (Figure 3.7),

$$ln(k_{TST}/T) = \ln(\kappa\frac{k_B}{h}) + \Delta S_{TS}/k_B - \Delta V_{TS}/k_B T \quad (3.19)$$

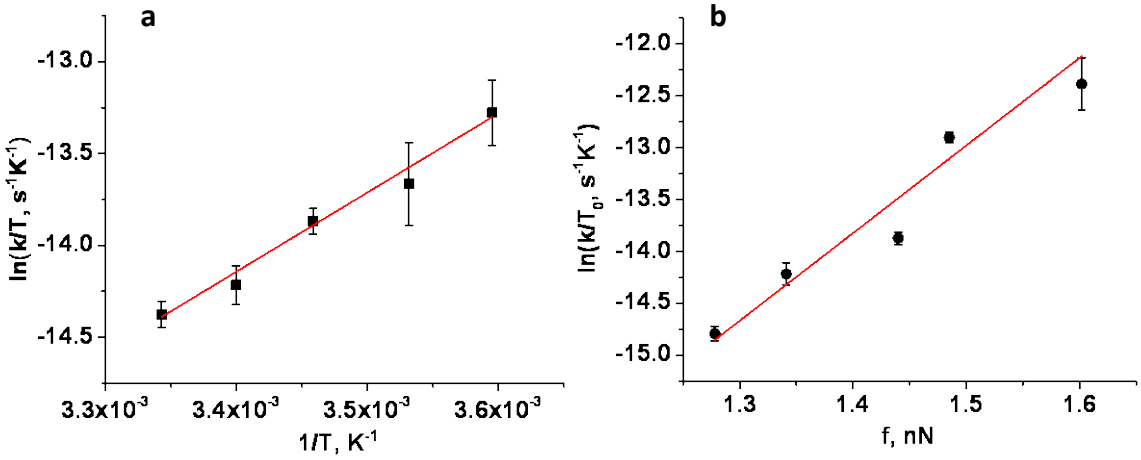

Figure 3.7 (a) Linear fit of $\ln(k/T)$ as as a function of 1/T with the fitting equation $\ln(k/T) = (4.31 \pm 0.31) \times \frac{10^3}{T} - (28.8 \pm 1.0)$. (b) Linear fit of $\ln(k/T_0)$ as a function of force at $T_0 = 21$℃ with the fitting equation $\ln(k/T_0) = (8.44 \pm 1.65)\, f - (25.6 \pm 2.4)$.

Because the measurements were conducted over a relatively narrow interval of forces, the experimental data points in Figure 3.7 (a) and (b) determine two local slopes of $\ln(k/T)$ as a function of $1/T$ and f respectively. To analyze the slopes, the function in eq. 3.19 was approximated by a Taylor series in a neighborhood of the mean force $f_a = 1.43\, nN$ and temperature $T_a = 289\, K$. Due to experimental error, it was sufficient to limit the Taylor approximation to its first order as:

$$\ln\left(\frac{k}{T}\right) \cong A_0 + A_1(f - f_a) \quad (3.20)$$

$$\ln\left(\frac{k}{T}\right) \cong B_0 + B_1(1/T - 1/T_a) \quad (3.21)$$

The coefficients A_1 and B_1 correspond to the first derivatives of eq. 3.19 with respect to f and $1/T$, respectively, which can be calculated using eq. 3.11, eq. 3.17 and eq. 3.18 as:

$$A_1 \equiv \frac{\partial \ln (k/T)}{\partial f}\Big|_{f=f_a} = -\frac{1}{k_B T}\frac{\partial \Delta V_{TS}(f_a)}{\partial f} = \frac{\Delta x(f_a)}{k_B T} \tag{3.22}$$

$$B_1 \equiv \frac{\partial \ln (k/T)}{\partial (1/T)}\Big|_{T=T_a} = \frac{1}{k_B}\left(bT_a \Delta x(T_a) - \Delta V_{TS}(T_a)\right) \tag{3.23}$$

From the slopes in Figure 3.7, we can determine the barrier parameters for both unperturbed potential (V_0 and f_m) and strained potential (ΔV_{TS} and Δx_{TS}), which are then used to construct the potential of disulfide bond (Figure 3.8).

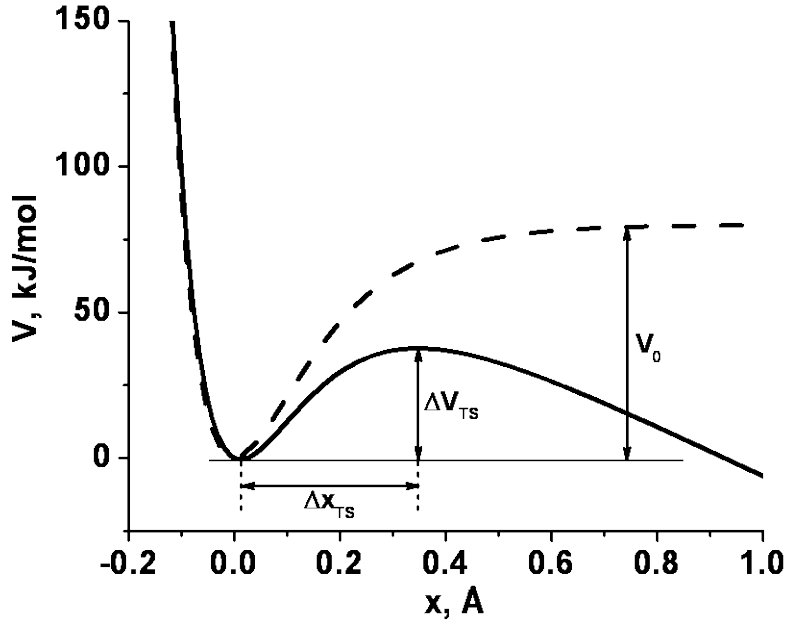

Figure 3.8 Morse potential of disulfide bond: – – – potential of unperturbed bond with dissociation energy $V_0 = 80\ kJ/mol$; —— effective potential of stretched bond under the force of 1.43 nN with $\Delta V_{TS} = 38\ kJ/mol$ and $\Delta x_{TS} = 0.34$ Å.

The determined maximum force $f_m = 4.8 \pm 1.3\ nN$ agrees with the rupture forces of disulfide bond from theoretical simulations in the range of 3.4~4.8 nN depending on the method used.[46] The bond dissociation energy $V_0 = 80 \pm 27\ kJ/mol$ is larger than that

obtained from Bell equation. As discussed in our recent paper,[23] the difference between the calculated dissociation energies from TST (V_0) and Bell equation (E_a) is the factor of $\sqrt{1-f/f_m}$, yielding $V_0' \cong 82\ kJ/mol$ in our case with $f/f_m \cong 0.3$ if one does not consider the effect of temperature on the pre-exponential factor, ascribed to the force dependence of both $\Delta V_b = V_b(x_{TS}) - V_b(x_0) = V_0\sqrt{1-f/f_m}$ and Δx. V_0, however, is slightly smaller than V_0' due to the linear dependence of the pre-exponential factor on temperature, which leads to the increase of the slope in Figure 3.7a by 7% compared with that in Figure 3.4c.

To analyze the pre-exponential factor, from the ordinate intercept of the linear dependence of $\ln(k/T_0)$ upon f, one can estimate the pre-exponential factor (A) at $T_0 =$ 21 ℃ to be on the order of 10^6 s^{-1}, which is about two orders of magnitude larger than that obtained in the first model. This is due to the underestimation of disulfide dissociation energy in the latter case. However, it is still much smaller than the nominal attempt frequency of $10^{12}\ s^{-1}$, which could be ascribed to both conformational and packing constrains of the backbone imposed by bottlebrush architecture and strong adsorption to a surface, and the effects of these constrains could be included into the transmission coefficient κ.[35,47] Table 3.1 summarizes the results from both models.

Table 3.1. Bond potential and activation parameters obtained from different models.

Model	dissociation energy(kJ/mol)	Δx, Å	Pre-exponential factor, s^{-1}
Bell equation	69 ± 24	0.34 ± 0.07	$\sim 10^4$
TST	80 ± 27	0.34 ± 0.07	$\sim 10^6$ (21℃)

3.4 Reduction of strained disulfide by DTT

Thiol/disulfide exchange reaction is of great importance in biological systems.[48-52] In this work, disulfide was reduced to thiols, leading to the scission of disulfide bond, while DTT was oxidized (Figure 3.9). Yet, mechanically induced homolytic scission of disulfide bonds occurred simultaneously in the studied system. Since these reactions (homolytic scission and reduction by DTT) occur on different time scales (DTT-reduction is much faster), we conducted our experiments at lower bond tensions to suppress the homolytic cleavage and thus increase the contribution of bond scission due to reduction. The bond tension was controlled by using molecular bottlebrushes with shorter side chains (n=60) to ensure that the backbone tension is below (or just above) 1 nN.

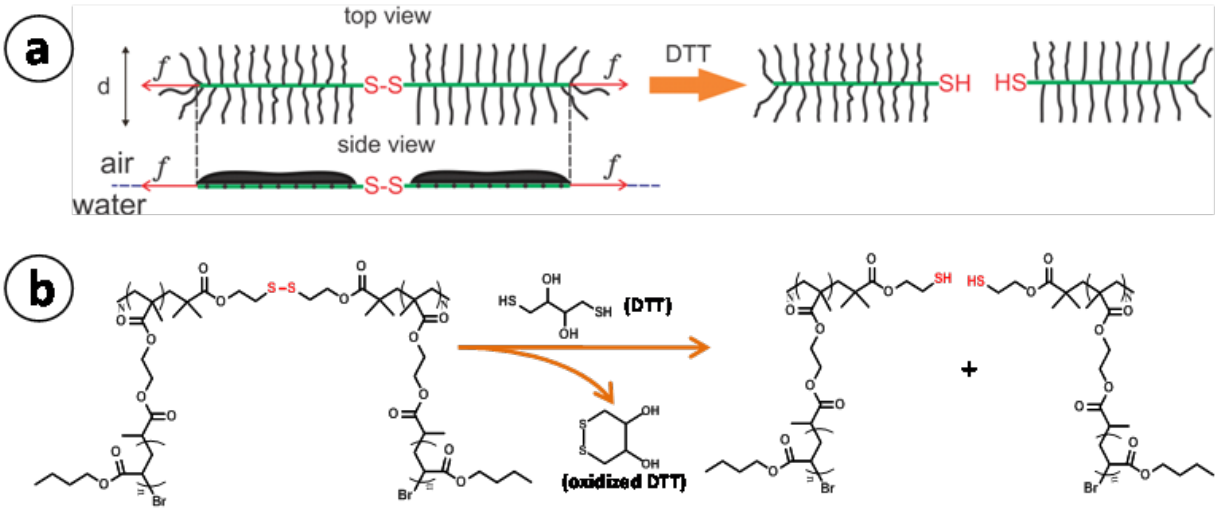

Figure 3.9 (a) The backbone in a bottlebrush macromolecule at the air-water interface is strained due to steric repulsion between the densely grafted side chains. The intrinsic tension in the backbone facilitates reduction of the disulfide linker with dithiothreitol (DTT). (b) Chemical structure of the studied molecular bottlebrushes with poly(*n*-butyl acrylate) side chains and a disulfide linker in the middle of the backbone.

3.4.1 The effect of DTT concentration

The first step in this study was to verify that DTT dissolved in the water subphase accelerates the scission of the disulfide linker in bottlebrush macromolecules adsorbed at the

water/air interface. For this purpose, the kinetics of the reduction process was investigated at six different concentrations of DTT under the same tension. As an example, Figure 3.10 shows two AFM micrographs along with the corresponding length distributions for a lower (1.94×10^{-5} M) and higher (1.94×10^{-4} M) concentrations of DTT in the water subphase. In both cases, one observed a bimodal length distribution represented by two bands at L≅300 nm and L/2≅150 nm that correspond respectively to a) the full length of bottlebrushes with the intact disulfide linker and b) monosulfide bottlebrushes due to mid-chain scission of the disulfide linker during synthesis.[6] However, the relative contribution of the intact macromolecules promptly decreases with the DTT concentration. As shown in Figure 3.10b, after 4h on 1.94×10^{-4}M DTT solution substrate, the population of long molecules at L≅300 nm almost vanished leading to the corresponding increase of the L/2 fraction at 150 nm. This clearly indicates that DTT promotes the scission of the disulfide linker.

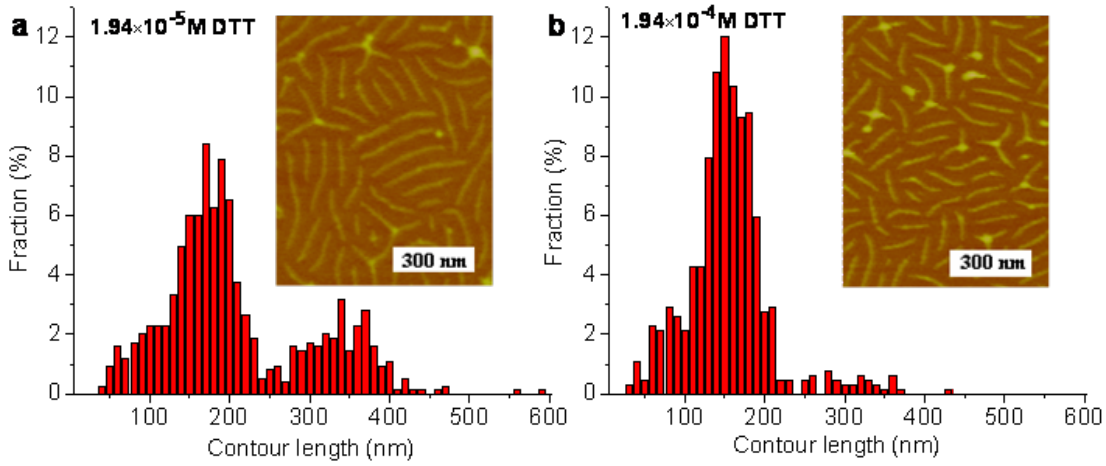

Figure 3.10 AFM height images along with the corresponding length distributions were measured for bottlebrush macromolecules that (prior to transfer to mica) were deposited for 4h on water substrates containing two different concentrations of DTT: (a) 1.94×10^{-5}M and (b) 1.94×10^{-4}M.

Similarly, the time dependence of average contour length can be also described by eq. 3.9 with $L_\infty = 149 \pm 3\ nm$, the average contour length of the mid-chain broken macromolecules measured at long times (days, $t = \infty$). For each [DTT] dataset, the initial time ($t = 0$) was assigned to the first collected data point. As mentioned above, we assume that two parallel processes contribute to the disulfide bond scission: (i) the homolytic scission of the disulfide bond (rate constant k_s) and (ii) the reduction of disulfide by DTT (rate constant k_r), which are the first- and second-order reactions, respectively. Taking [*DDT*] as constant since DTT is present in excess with respect to disulfide (the moles of DTT are at least 10^7 times that of disulfide for all DTT concentrations), the reduction reaction can considered a pseudo first-order reaction. As such, the total rate constant can be written as

$$k = k_r[DTT] + k_s \tag{3.24}$$

Eq. 3.9 was used to fit the experimental data points in Figure 3.11a using the rate constant *k* as a single fitting parameter. The obtained values of the rate constant were plotted as a function of DTT concentration (Figure 3.11b). The first data point corresponds to $k_s = 10^{-5} s^{-1}$, i.e. the rate constant at zero [DTT]. By fitting the data points in Figure 3.11b using eq. 3.24 one obtains $k_r = 1.4\ M^{-1}s^{-1}$, which is the second-order rate constant for thiol/disulfide exchange reaction on the surface of water.

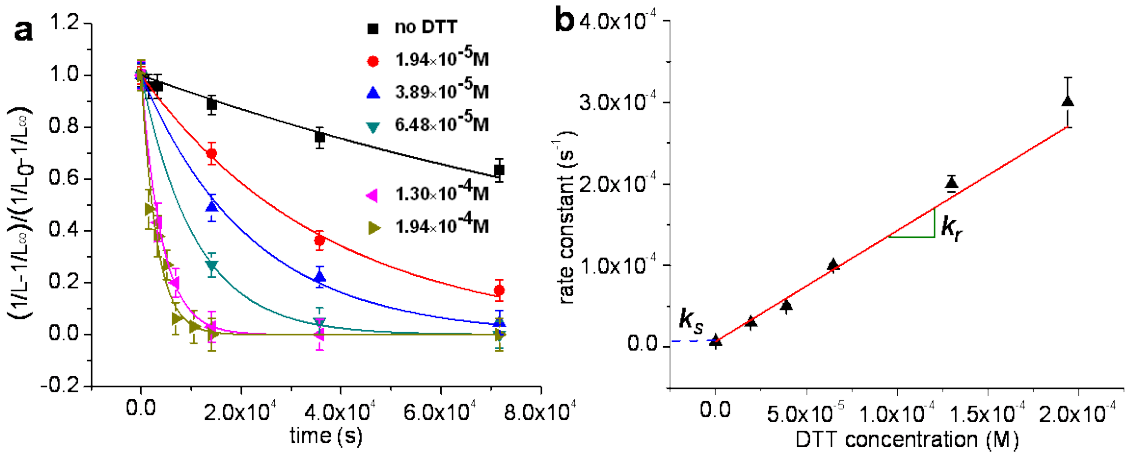

Figure 3.11 (a) Kinetics of the disulfide bond scission at various concentrations of DTT under the same tension ($f = 1.44$ nN). Solid lines are generated by fitting the data points with eq. 3.9 using the rate constant k as a single fitting parameter. (b) The rate constants obtained from the fitting analysis in (a) are plotted as a function of DTT concentration. The linear fit (eq. 3.24, solid line) gives the second-order rate constant k_r for thiol/disulfide exchange reaction. The rate constant $k_s = 10^{-5}s^{-1}$ at zero [DTT] was obtained from the fitting analysis of the upper set (■) of data points in (a).

3.4.2 The effect of force.

To study the effect of bond tension on the reduction rate constant, the bottlebrush macromolecules were deposited on the surface of different water/2-propanol mixtures. On pure water at a room temperature of 298 K, we measured $d = 60 \pm 2\ nm$ and $S = 24.0 \pm 0.2\ mN/m$, which gave a backbone tension of $f_w = 1.44 \pm 0.06\ nN$. Upon adding 2-propanol, the spreading parameter decreases and so does the backbone tension. Figure 3.12 presents kinetic curves measured for different values of the backbone tension at the same concentration of DTT (1.94×10^{-4}M). The figure clearly shows that an incremental increase of bond tension from 0.95 nN to 1.26 nN results in significant acceleration of the scission reaction.

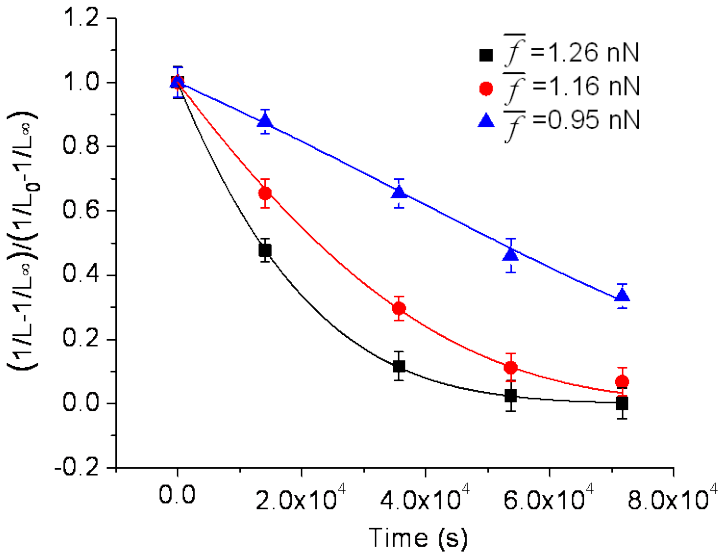

Figure 3.12 Kinetics of disulfide bond scission on three different substrates and, hence, backbone tensions (as indicated). The substrates were mixtures of water and 2-propanol with the following fractions of 2-propanol: 0.3% (black square), 0.5% (red circle), 1.0% (blue triangle). DTT concentration was the same, 1.94×10^{-4}M, in all three experiments.

To quantify the observed tension effects, the data in Figure 3.12 were analyzed using a phenomenological equation proposed by Eyring, Zhurkov, and Bell for various force-activated bond-scission reactions, [30,42-43]

$$k_r = k_{r,0} e^{f\Delta x/k_B T} \tag{3.25}$$

where $k_{r,0}$ is the rate constant at zero force, Δx is the distance from the minimum of the potential well to the transition state along the reaction coordinate,[53] and $k_B = 1.38 \cdot 10^{-23}\, J/K$ is the Boltzmann's constant. Since the rate constant at zero force is unknown, we calculate the rate constant in eq. 3.25 relative to the independently measured rate constant $k_{r,w}$ on a water surface as

$$k_r = k_{r,w} e^{(f-f_w)\Delta x/k_B T} \tag{3.26}$$

where $k_{r,w} = 1.4\ \text{M}^{-1}\text{s}^{-1}$ and $f_w = 1.44\ nN$. Here we assume that Δx does not depend on force, which is acceptable for the narrow interval of forces studied in this work. As mentioned in the experimental section, special care was taken to control the evaporation of 2-propanol and monitor on the resulting variation of the spreading parameter on long time scales. Figure 3.13 shows temporal variations of the spreading parameter for the substrates studied in this work. Within the 20-hour time frame, the tension variation can be approximated with a linear equation,

$$f = \alpha t + f_0 \tag{3.27}$$

where α and f_0 calculated from the linear fitting results in Figure 3.13 are summarized in Table 3.2.

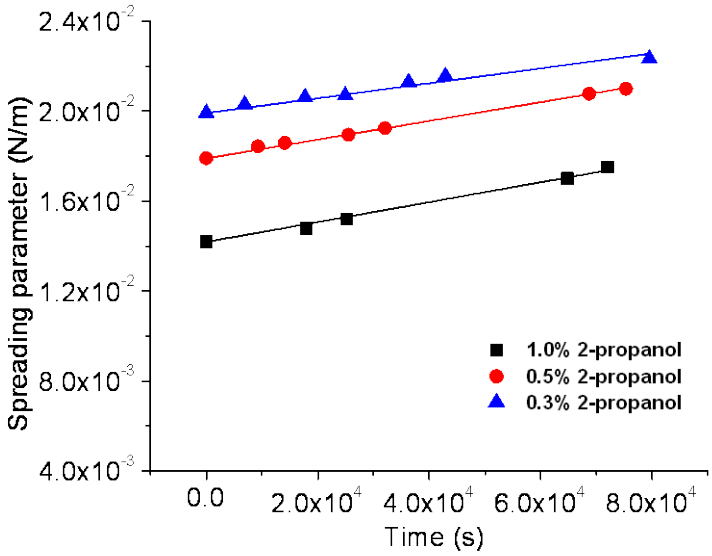

Figure 3.13 Spreading parameter versus time (with the same DTT concentration 1.94×10^{-4}M). Solid lines are linear fitting to the data points.

Table 3.2 α and f_0 values calculated from linear fitting results in Figure 3.13

2-propanol concentration, wt%	$a, 10^{-6} nN/s$	f_0, nN
0.3	1.99	1.19
0.5	2.50	1.07
1.0	2.66	0.85

Even though the effect of propanol evaporation on tension is relatively small (~20% increase), the exponential $k(f)$ dependence (eq. 3.25) requires its inclusion to the kinetics analysis. Plugging eq. 3.27 into eq. 3.26, the following relation can be obtained,

$$k_r = k_{r,w} e^{\frac{(\alpha t + f_0 - f_w)\Delta x}{k_B T}} \tag{3.28}$$

which also depends on time, leading to the failure of eq. 3.9. To derive the kinetic equation regarding the average contour length and time, we approximate eq.3.24 as

$$k \cong k_r [DTT] \tag{3.29}$$

by omitting k_s of the homolytic bond scission ($k_s \ll k$). Then we can get the change the number of disulfide bonds over time as

$$\frac{\partial [S-S]}{\partial t} = kt = k_{r,w}[DTT][S-S] e^{\frac{(\alpha t + f_0 - f_w)\Delta x}{k_B T}} \tag{3.30}$$

By integrating eq. 3.30, one can obtain the following equation

$$\frac{[S-S]}{[S-S]_0} = \exp\left\{-k_{r,w} \cdot [DTT] \cdot \frac{k_B T}{\alpha \cdot \Delta x} \cdot e^{(f_0 - f_w)\cdot \Delta x / k_B T} \cdot \left(e^{\alpha t \cdot \Delta x / k_B T} - 1\right)\right\} \tag{3.31}$$

Substituting eq. 3.7 into eq. 3.31, we can derive the relation between the average contour length and time as

$$\left(\frac{1}{L} - \frac{1}{L_\infty}\right) \Big/ \left(\frac{1}{L_0} - \frac{1}{L_\infty}\right) = \exp\left\{-k_{r,w} \cdot [DTT] \cdot \frac{k_B T}{\alpha \cdot \Delta x} \cdot e^{(f_0 - f_w)\cdot \Delta x / k_B T} \cdot \left(e^{\alpha t \cdot \Delta x / k_B T} - 1\right)\right\} \tag{3.32}$$

which was used to fit the experimental data points in Figure 3.12 with Δx as a single fitting parameter. The determined Δx values were then used to calculate the corresponding rate constant (eq. 3.26). Table 3.3 summarizes the results.

Table 3.3 Results from fitting analysis in Figure 3.12

$\overline{f}$ [1] (*nN*)	Δx [2] (*nm*)	k_r [3] ($M^{-1}s^{-1}$)
1.26	0.024	0.49
1.16	0.026	0.24
0.95	0.029	0.04

1) $\overline{f} = \alpha t/2 + f_0$ is the average force over time.
2) Δx values were obtained from fitting analysis in Figure 3.12.
3) k_r was calculated using eq. 3.26 with corresponding $\overline{f}$ and Δx

The obtained Δx values are somewhat smaller than the corresponding data from single-molecule force-clamp spectroscopy experiments[16,29] ($\Delta x = 0.029 - 0.035$ nm) and theoretical calculations ($\Delta x = 0.036$ nm,[54] $\Delta x = 0.037$ nm[29,55]) conducted at contact force and using thiol-based reducing agents. There could be several reasons for this deviation. First, 3% (ca. 0.001 nm) underestimation of the Δx value is due to the drop of bond tension in the middle section of the backbone, which does not carry side chains (Appendix III). Second, the covalent backbone encapsulated within a shell of tightly adsorbed side chain (Figure 3.9a) is significantly more constrained than polymer chains pulled by a single-molecule probe. The disulfide bond is unable to sample the entire configurational space resulting in a narrow distribution of the angle between the S-S bond and the stretching direction, which directly affects the force projection on the bond. Third, the deviation can be commonly ascribed to the intrinsic uncertainty of the scaling relation (eq. 3.10) that predicts tension values up to a numerical coefficient of the order of unity.

We can also estimate the activation energy using the relationship $k_{r,0} = Ae^{-E_a/RT}$, where $k_{r,0} = 1.4 \times 10^{-4} M^{-1}s^{-1}$ is the second order rate constant for DTT reduction of disulfide at zero force, A is the pre-exponential factor, and R is the universal gas constant. For a broad interval of A ranging from 10^5 to $10^{12}\ M^{-1}s^{-1}$, we estimate the activation energy barrier E_a to be in the range of 51 to 91 kJ/mol. This is about 20 kJ/mol higher than the energy range of 30 to 65kJ/mol obtained in single-molecule pulling tests at constant force,[16,56] which may be attributed to a lower pH at the air/water interface as discussed below.

3.4.3 pH of water surface

The redox rate constant depends on pH of the reaction medium.[57-58] Therefore, it is instructive to compare the rate constant at zero force ($k_{r,0}$) with the corresponding literature data obtained under controlled pH conditions in bulk solutions. For one of the determined Δx values, e.g., $\Delta x = 0.026\ nm$, we can calculate $k_{r,0} = k_{r,w} \cdot e^{-f_w \cdot \Delta x / k_B T} = 1.4 \times 10^{-4} M^{-1}s^{-1}$. This value is at least four orders of magnitude smaller than the second-order rate constant, $5\ M^{-1}s^{-1}$, for the DTT reduction of disulfide bonds in insulin at pH=7,[57]. Such a significant discrepancy may be due to steric inaccessibility of the disulfide bond surrounded by a shell of side chains.[59] However, in adsorbed brushes, the hydrophobic side chains are segregated at the air side of the air/water interface and, hence, do not impose significant steric constraints for small DTT molecules in the aqueous subphase. Therefore, we tentatively believe that the low rate constant is caused by a higher acidity of the surface of water with respect to the neutral bulk water.[60-63] The pH value of the water surface can be estimated from the pH-independent rate constant $k_{r,0}^a$ which is related to the measured $k_{r,0}$ by the following equation

$$k_{r,0}^a = k_{r,0} \cdot \frac{1+10^{pK_2-pH}+10^{pK_1+pK_2-2pH}}{2+10^{pK_2-pH}} \approx k_{r,0} \cdot 10^{pK_1-pH} \qquad (3.33)$$

where pK_1=9.2 and pK_2=10.1 are the first and second dissociation constants for the first and second thiols of DTT respectively.[58,64] From the measured $k_{r,0} = 1.4 \times 10^{-4} M^{-1} s^{-1}$ and the pH-independent rate constant is $k_{r,0}^{a} \cong 50\ M^{-1} s^{-1}$ at room temperature of 298K,[58] one estimates the pH of water surface to be pH≅3.7. This value is significantly smaller than the measured pH=6.6 of the bulk water/2-propanol mixture (0.5 wt/wt %). The lower pH is consistent with the recent simulation and surface sensitive spectroscopic studies, suggesting that hydronium ion is enhanced at air/water interface when compared to bulk solution.[60-63] As such, our system may be used to explore the long standing debate about the acidity of the water surface.[65-68]

3.5 Conclusions

We have employed the molecular tensile machines that are bottlebrush molecules with a disulfide linker in the middle of the backbone to study the homolytic scission of disulfide bonds. The scission rate of the specifically activated disulfide bond by mechanic force showed exponential force dependence and anti-Arrhenius temperature effect. This unusual temperature effect is ascribed to the decrease of backbone tension with temperature, which can overpower the effects of thermal energy and temperature dependent pre-exponential factor. We have also been able to use molecular tensile machines to extract the activation barrier parameters of a covalent bond from the experimental data and construct its potential if assuming one. The phenomenological Bell equation gives the dissociation energy of disulfide bond and activation length; TST considering the force dependent Morse potential provides more information, including activation barrier height and width and maximum force, which are used to construct the potential. The dissociation energy calculated from Bell equation (E_a) deviates that obtained from TST (V_0) by a factor of $\sqrt{1 - f/f_m}$ approximately. In small force

range ($f \ll f_m$), the deviation is negligible since $\sqrt{1 - f/f_m} \cong 1$; if the applied force f is comparable to the maximum force f_m, TST that takes the force dependent potential into consideration should be more appropriate and accurate. The pre-exponential factor estimated from TST is about two orders of magnitude larger than that from Bell equation, due to the underestimation of disulfide bond dissociation energy in the latter case. Nevertheless, it is much smaller than the nominal attempt frequency of $10^{12}\ s^{-1}$, which could be ascribed to both conformational and packing constrains of the backbone imposed by bottlebrush architecture and strong adsorption to a surface.

Besides, we have extended our studies of "molecular tensile machines", bottlebrush macromolecules with a weak linker in the middle of the backbone, to probe the reduction of disulfide bonds by DTT under tension. The kinetics of the S-S reduction process was investigated as a function of DTT concentration and backbone tension. The reduction rate was shown to linearly increase with [DTT] and exponentially increase with tension, which in agreement with the previous literatures.[15-16,34] Although the estimated $\Delta x = 0.024 - 0.029\ nm$ and $E_a = 51 - 91\ kJ/mol$ are comfortably agrees with the literature data, their molecular interpretation needs to be further investigated using computational tools by taking into account the configurational constraints imposed by the bottlebrush architecture, interfacial confinement, and the aqueous environment. Our work provides tentative evidence that the surface of water is more acidic than bulk water. The designed "molecular tensile machines" may also be used to probe the chemistry of other bonds and have potential applications such as sensors, mechanocatalysts, and precursors for self-healing materials.

References

(1) Beyer, M. K.; Clausen-Schaumann, H. *Chem. Rev.* **2005**, *105*, 2921-2948.

(2) Caruso, M. M.; Davis, D. A.; Shen, Q.; Odom, S. A.; Sottos, N. R.; White, S. R.; Moore, J. S. *Chem. Rev.* **2009**, *109*, 5755-5798.

(3) Liang, J.; Fernández, J. M. *ACS Nano* **2009**, *3*, 1628-1645.

(4) Huang, Z.; Boulatov, R. *Chem. Soc. Rev.* **2011**, *40*, 2359-2384.

(5) Yang, Q.-Z.; Huang, Z.; Kucharski, T. J.; Khvostichenko, D.; Chen, J.; Boulatov, R. *Nature Nano.* **2009**, *4*, 302-306.

(6) Park, I.; Sheiko, S. S.; Nese, A.; Matyjaszewski, K. *Macromolecules* **2009**, *42*, 1805-1807.

(7) Hickenboth, C. R.; Moore, J. S.; White, S. R.; Sottos, N. R.; Baudry, J.; Wilson, S. R. *Nature* **2007**, *446*, 423-427.

(8) Parks, J. J.; Champagne, A. R.; Costi, T. A.; Shum, W. W.; Pasupathy, A. N.; Neuscamman, E.; Flores-Torres, S.; Cornaglia, P. S.; Aligia, A. A.; Balseiro, C. A.; Chan, G. K.-L.; Abruña, H. D.; Ralph, D. C. *Science* **2010**, *328*, 1370-1373.

(9) Lenhardt, J. M.; Ong, M. T.; Choe, R.; Evenhuis, C. R.; Martinez, T. J.; Craig, S. L. *Science* **2010**, *329*, 1057-1060.

(10) Davis, D. A.; Hamilton, A.; Yang, J.; Cremar, L. D.; Van Gough, D.; Potisek, S. L.; Ong, M. T.; Braun, P. V.; Martinez, T. J.; White, S. R.; Moore, J. S.; Sottos, N. R. *Nature* **2009**, *459*, 68-72.

(11) Lenhardt, J. M.; Black, A. L.; Craig, S. L. *J. Am. Chem. Soc.* **2009**, *131*, 10818-10819.

(12) Piermattei, A.; Karthikeyan, S.; Sijbesma, R. P. *Nature Chem.* **2009**, *1*, 133-137.

(13) Tennyson, A. G.; Wiggins, K. M.; Bielawski, C. W. *J. Am. Chem. Soc.* **2010**, *132*, 16631-16636.

(14) Wiggins, K. M.; Hudnall, T. W.; Shen, Q.; Kryger, M. J.; Moore, J. S.; Bielawski, C. W. *J. Am. Chem. Soc.* **2010**, *132*, 3256-3257.

(15) Singh, R.; Whitesides, G. M. *J. Am. Chem. Soc.* **1990**, *112*, 6304-6309.

(16) Wiita, A. P.; Ainavarapu, S. R. K.; Huang, H. H.; Fernandez, J. M. *Proc. Natl. Acad. Sci. USA* **2006**, *103*, 7222-7227.

(17) Kucharski, T. J.; Huang, Z.; Yang, Q.-Z.; Tian, Y.; Rubin, N. C.; Concepcion, C. D.; Boulatov, R. *Angew. Chem., Int. Ed.* **2009**, *48*, 7040-7043.

(18) Sheiko, S. S.; Sun, F. C.; Randall, A.; Shirvanyants, D.; Rubinstein, M.; Lee, H.-i.; Matyjaszewski, K. *Nature* **2006**, *440*, 191-194.

(19) Lebedeva, N. V.; Sun, F. C.; Lee, H.-i.; Matyjaszewski, K.; Sheiko, S. S. *J. Am. Chem. Soc.* **2008**, *130*, 4228-4229.

(20) Park, I.; Shirvanyants, D.; Nese, A.; Matyjaszewski, K.; Rubinstein, M.; Sheiko, S. S. *J. Am. Chem. Soc.* **2010**, *132*, 12487-12491.

(21) Park, I.; Nese, A.; Pietrasik, J.; Matyjaszewski, K.; Sheiko, S. S. *J. Mater. Chem.* **2011**, *21*, 8448-8453.

(22) Li, Y.; Nese, A.; Lebedeva, N. V.; Davis, T.; Matyjaszewski, K.; Sheiko, S. S. *J. Am. Chem. Soc.* **2011**, *133*, 17479-17484.

(23) Lebedeva, N. V.; Nese, A.; Sun, F. C.; Matyjaszewski, K.; Sheiko, S. S. *Proc. Natl. Acad. Sci. USA* **2012**, *109*, 9276-9280.

(24) Freedman, R. B.; Hirst, T. R.; Tuite, M. F. *Trends in Biochemical Sciences* **1994**, *19*, 331-336.

(25) Wedemeyer, W. J.; Welker, E.; Narayan, M.; Scheraga, H. A. *Biochemistry* **2000**, *39*, 4207-4216.

(26) Myers, J. K.; Nick Pace, C.; Martin Scholtz, J. *Protein Science* **1995**, *4*, 2138-2148.

(27) Sheiko, S. S.; Möller, M. *Chem. Rev.* **2001**, *101*, 4099-4124.

(28) Sheiko, S. S.; Prokhorova, S. A.; Beers, K. L.; Matyjaszewski, K.; Potemkin, I. I.; Khokhlov, A. R.; Möller, M. *Macromolecules* **2001**, *34*, 8354-8360.

(29) Sheiko, S. S.; Möller, M. In *Macromolecular Engineering : Precise Synthesis, Materials Properties, Applications*; Krzysztof Matyjaszewski, Y. G., Ludwik Leibler, Ed.; Wiley: 2007; Vol. 3, p 1515-1574.

(30) Bell, G. *Science* **1978**, *200*, 618-627.

(31) Evans, E.; Ritchie, K. *Biophysical Journal* **1997**, *72*, 1541-1555.

(32) Beyer, M. K. *J. Chem. Phys.* **2000**, *112*, 7307-7312.

(33) Dudko, O. K.; Hummer, G.; Szabo, A. *Phys. Rev. Lett.* **2006**, *96*, 108101.

(34) Liang, J.; Fernández, J. M. *J. Am. Chem. Soc.* **2011**, *133*, 3528-3534.

(35) Wynne-Jones, W. F. K.; Eyring, H. *J. Chem. Phys.* **1935**, *3*, 492-502.

(36) Kramers, H. A. *Physica* **1940**, *7*, 284-304.

(37) Matyjaszewski, K.; Xia, J. *Chem. Rev.* **2001**, *101*, 2921-2990.

(38) Pakula, T.; Zhang, Y.; Matyjaszewski, K.; Lee, H.-i.; Boerner, H.; Qin, S.; Berry, G. C. *Polymer* **2006**, *47*, 7198-7206.

(39) Sheiko, S. S.; Sumerlin, B. S.; Matyjaszewski, K. *Prog. Polym. Sci.* **2008**, *33*, 759-785.

(40) Lee, H.-i.; Pietrasik, J.; Sheiko, S. S.; Matyjaszewski, K. *Prog. Polym. Sci.* **2010**, *35*, 24-44.

(41) Matyjaszewski, K. *Macromolecules* **2012**, *45*, 4015-4039.

(42) Kauzmann, W.; Eyring, H. *J. Am. Chem. Soc.* **1940**, *62*, 3113-3125.

(43) Zhurkov, S. N. *Int. J. Fract. Mech.* **1965**, *1*, 311-322.

(44) Iozzi, M. F.; Helgaker, T.; Uggerud, E. *J. Phys. Chem. A* **2011**, *115*, 2308-2315.

(45) Nichols, P.; Grant, M. *Aust. J. Chem.* **1983**, *36*, 1379-1386.

(46) Iozzi, M. F.; Helgaker, T.; Uggerud, E. *Molecular Physics* **2009**, *107*, 2537-2546.

(47) Winzor, D. J.; Jackson, C. M. *J. Mol. Recognit.* **2006**, *19*, 389-407.

(48) Chen, S.; Springer, T. A. *Proc. Natl. Acad. Sci. USA* **2001**, *98*, 950-955.

(49) Kadokura, H.; Katzen, F.; Beckwith, J. *Annu, Rev. Biochem* **2003**, *72*, 111-135.

(50) Barford, D. *Curr. Opin. Struct. Biol.* **2004**, *14*, 679-686.

(51) Yan, B.; Smith, J. W. *Biochemistry* **2001**, *40*, 8861-8867.

(52) Mayans, O.; Wuerges, J.; Canela, S.; Gautel, M.; Wilmanns, M. *Structure (London, England : 1993)* **2001**, *9*, 331-340.

(53) Koti Ainavarapu, S. R.; Wiita, A. P.; Dougan, L.; Uggerud, E.; Fernandez, J. M. *J. Am. Chem. Soc.* **2008**, *130*, 6479-6487.

(54) Császár, P.; Csizmadia, I. G.; Viviani, W.; Loos, M.; Rivail, J.-L.; Perczel, A. *J. Mol. Struct. Theochem.* **1998**, *455*, 107-122.

(55) Fernandes, P. A.; Ramos, M. J. *Chem. Eur. J.* **2004**, *10*, 257-266.

(56) Ainavarapu, S. R. K.; Wiita, A. P.; Dougan, L.; Uggerud, E.; Fernandez, J. M. *J. Am. Chem. Soc.* **2008**, *130*, 6479-6487.

(57) Holmgren, A. *J. Biol. Chem.* **1979**, *254*, 9627-9632.

(58) Rothwarf, D. M.; Scheraga, H. A. *Proc. Natl. Acad. Sci. U.S.A.* **1992**, *89*, 7944-7948.

(59) Creighton, T. E. *J. Mol. Biol.* **1975**, *96*, 767-776.

(60) Buch, V.; Milet, A.; Vácha, R.; Jungwirth, P.; Devlin, J. P. *Proc. Natl. Acad. Sci. U.S.A.* **2007**, *104*, 7342-7347.

(61) Iuchi, S.; Chen, H.; Paesani, F.; Voth, G. A. *J. Phys. Chem. B* **2008**, *113*, 4017-4030.

(62) Vacha, R.; Horinek, D.; Berkowitz, M. L.; Jungwirth, P. *Phys. Chem. Chem. Phys.* **2008**, *10*, 4975-4980.

(63) Petersen, P. B.; Saykally, R. J. *J. Phys. Chem. B* **2005**, *109*, 7976-7980.

(64) Whitesides, G. M.; Lilburn, J. E.; Szajewski, R. P. *The Journal of Organic Chemistry* **1977**, *42*, 332-338.

(65) Beattie, J. K.; Djerdjev, A. M. *Angewandte Chemie* **2004**, *116*, 3652-3655.

(66) Beattie, J. K.; Djerdjev, A. M.; Warr, G. G. *Faraday Discussions* **2009**, *141*, 31-39.

(67) Creux, P.; Lachaise, J.; Graciaa, A.; Beattie, J. K.; Djerdjev, A. M. *J. Phys. Chem. B* **2009**, *113*, 14146-14150.

(68) Mundy, C. J.; Kuo, I. F. W.; Tuckerman, M. E.; Lee, H.-S.; Tobias, D. J. *Chem. Phys. Lett.* **2009**, *481*, 2-8.

Chapter 4

Tension Effects on Optical Properties

4.1 Introduction

Materials, changing color upon mechanical deformation, have potential applications in pressure or stress sensors. Recently, there have been a large quantity of reports about mechanically induced color or spectroscopic change of polymer based materials, and the mechanisms vary from case to case.[1] Weder et al. have done pioneering work on the photoluminescent character change of chromophores-polymer blends where the chromophores were dispersed in a polymer matrix.[2-3] Upon tensile deformation, the aggregates of chromophores were dissociated, leading to large blue shifts. Reneker et al. showed that tension induced cis to trans conformation change of azobenzene could also result in the change of its absorption.[4] In another example, it was showed that the absorption peak of polythiophene (PT) exhibits a red shift with increasing pressure due to the increase of effective conjugation length.[5-7] More recently, Moore et al. reported that bulk polymers with mechanophores (spiropyran) links incorporated into the networks changed color upon stretching, involving the ring-opening reaction of spiropyran to form merocyanine with C-O bond rupture.[8] Other mechanisms include mechanically induced formation of excimers,[9-10] interchain interaction,[11-13] and *etc*. However, in all these examples, the effect of bond deformation including length and angle due to tension, which could be important, was neglected. Although there are reports showing the spectroscopic changes of poly (diacetylenes) incorporated into a polymer matrix with strains,[14-16] the effect of tension still

remains mystery because of the uncertainty of the relation between macroscopic strain and bond tension on a molecular scale.

In this chapter, we present our investigation of the effects of tension on the photophysics of PT with the help of molecular tensile machines that are molecular bottlebrushes.[17-21] The tension is self-generated along the backbone due to steric repulsion between densely grafted side chains and can be amplified from picoNewton to nanoNewton range upon adsorption to a liquid substrates by controlling the length of side chains, surface tension of the substrate and the pressure of the molecular bottlebrush film.[22-23] The advantages of bottlebrush macromolecules are force control that tension is evenly distributed along the backbone (except the end caps)[24] and representative statistics of stressed PTs. Here, the molecular tensile machines are bottlebrush macromolecules with PT backbone and poly(butyl acrylate) (PBA) side chains. PT has been chosen as a model molecule given that PT based materials are commonly used in organic solar cells and field-effect transistors[25-27] and thus it is important for both fundamental understanding and potential applications. The PT bottlebrushes are named as PT-m where m is the degree of polymerization (DP) of PBA side chains. In this paper, the spectroscopic characterization of the PT bottlebrushes under controlled force is discussed and compared to the prediction of density functional theory (DFT) calculations.

4.2 Experimental Section

4.2.1 Synthesis and characterization of 2,5-Poly(3-[1-ethyl-2(2-(poly(butyl acrylate))]thiophene) (PEBBT-g-PBA). Typical procedure is as follows**:** A clean and dry 25 ml Schlenk flask was charged with 2,5-Poly(3-[1-ethyl-2(2-bromoisobutyrate)]thiophene) (PEBBT, (0.0278 g, 0.100 mmol, prepared by following a previously published procedure),[28]

butyl acrylate (18.0 mL, 140 mmol), N,N,N',N'',N''-pentamethyldiethylenetriamine (8.63 µg, 0.050 mmol), $CuBr_2$ (0.0006 g, 0.0025 mmol), and anisole (2.00 mL). The flask was deoxygenated by two freeze-pump-thaw cycles. During the last cycle, the flask was filled with nitrogen and CuBr (0.0068 g, 0.0475 mmol) was added to the frozen mixture. The flask was sealed, evacuated and back-filled with nitrogen five times before it was immersed in an oil bath at 50 ^{o}C. During the reaction, fractions of aliquot were taken out via syringe to obtain molecular bottlebrushes with a series of molecular weights (Table 4.1).

Scheme 4.1 Synthesis of PEBBT-g-PBA molecular bottlebrushes

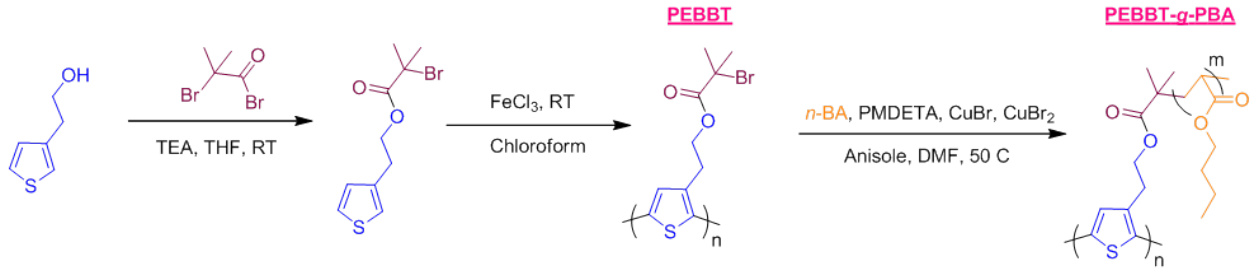

Table 4.1 Characterization of PT bottlebrushes

Sample	Mn[a]	PDI[b]	d(nm)[c]	$\lambda_{max,ex}$(nm) [d]	$\lambda_{max,em}$(nm) [e]
Macroinitiator (MI)	46,200	11.6	NA	415	554
PT-5	135,000	4.96	15±3	425	549
PT-25	244,000	4.48	35±2	427	547
PT-60	643,000	2.93	64±2	428	546
PT-120	852,000	2.60	84±2	430	545
PT-190	1,040,000	2.46	120±2	429	546

[a] Molecular weight determined by GPC. [b] Polydispersity determined by GPC. [c] The width of PT bottlebrush determined from AFM images (Figure 4.1). [d] Wavelength at maximum emission intensity in chloroform solution. [e] Wavelength at maximum excitation intensity in chloroform solution.

To confirm successful synthesis of the PT bottlebrush molecules, AFM was used to investigate their structures (the procedures are shown in the next section). The imaged

molecules exhibit wormlike conformation, suggesting extension of densely grafted molecular bottlebrushes (Figure 4.1). The widths of the bottlebrushes increase with the DP of PBA side chains (Table 4.1 and Appendix IV).

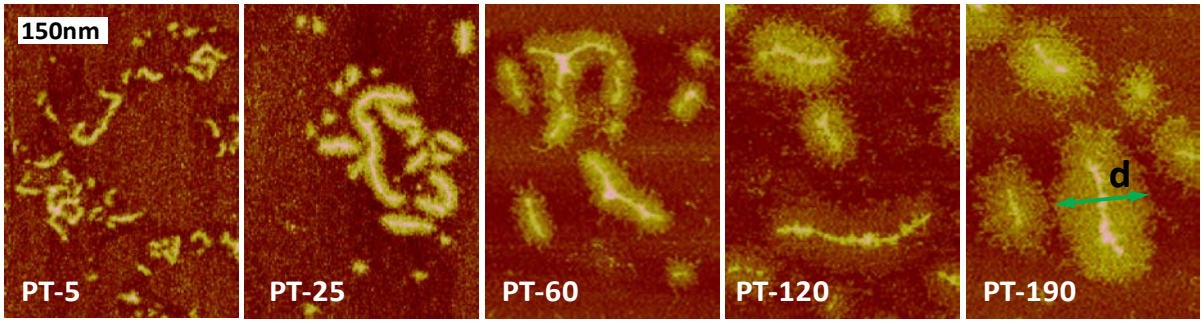

Figure 4.1 AFM height images of the PT bottlebrushes with different DP of PBA side chains spin cast from dilute chloroform solution onto freshly cleaved mica substrates.

Fluorescence spectra of MI and PT bottlebrushes in chloroform solution were recorded on PTI-QM4SE-NIR spectrometer (Photon Technology International) using 1.00 cm quartz cuvettes. Their fluorescence excitation and emission spectra are showed in Figure 4.2.

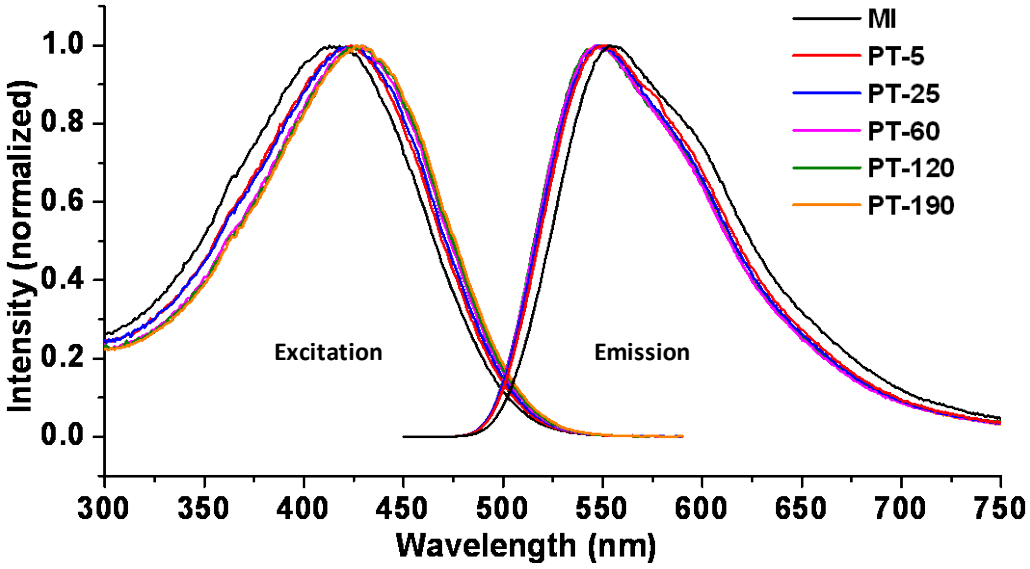

Figure 4.2 Normalized fluorescence spectra of PT samples in chloroform solutions. For the emission spectra, all the samples were excited at 405 nm.

For the MI, the wavelengths of the maximal excitation ($\lambda_{max,ex}$) and emission ($\lambda_{max,em}$) are 415 nm and 554 nm respectively; after graft of PBA side chains (e.g. PT-5), there was a red shift (ca. 10 nm) of $\lambda_{max,ex}$ and a blue shift (ca. 5 nm) of $\lambda_{max,em}$. However, the shifts between the PT bottlebrushes of different DP of PBA side chains were much smaller. This could be due to a greater flexibility of MI in the absence of PBA side chains, which might facilitate larger excitonic structural distortions relative to the MI ground state.[28]

In solutions, the backbone tension in bottlebrush molecules is small, on the order of 10-100 pN.[22] Therefore the effect of tension will not be discussed.

4.2.2 Atomic force microscopy (AFM). To confirm wormlike structures of PT bottlebrush samples, dispersed thin films of the molecules were prepared by spin-casting from a dilute solution in chloroform on a freshly cleaved mica substrate. To study the conformation of PT backbones, dense films were transferred from Langmuir-Blodgett (LB) trough (Minimicro, KSV) onto freshly cleaved mica substrates at constant film pressure. Topographic images of individual molecules were collected using a multimode Atomic Force Microscopy (Bruker) in PeakForce mode.[29] We used silicon cantilevers with a resonance frequency of about 50-90 kHz and a spring constant of about 0.4 N/m.

4.2.3 Fluorescence (FL) spectroscopy. Fluorescence spectra of sub-monolayers were recorded by a spectrograph (Acton SP2300, Princeton Instruments) with a CCD camera (eXcelon, Princeton Instruments) on a LB trough (Minimicro, KSV) with a quartz window in the center as showed in Figure 4.3. The substrate in the trough was a mixture of water (Milli-Q double-distilled, ρ=18.2 MΩ) and 2-propanol (Aldrich, 99%) which allows accurate control of the spreading parameter of PBA bottlebrushes. A direct emitting semiconductor laser (405nm, Coherent) was used as the excitation source. The laser beam passed through

the objective (Olympus Uplan FLN 10×, NA 0.3) of an inverted microscope (Olympus X71) that was focused on the surface of water/2-propanol mixture and excited the pre-deposited samples. The pressure of the monolayer was controlled by LB control software.

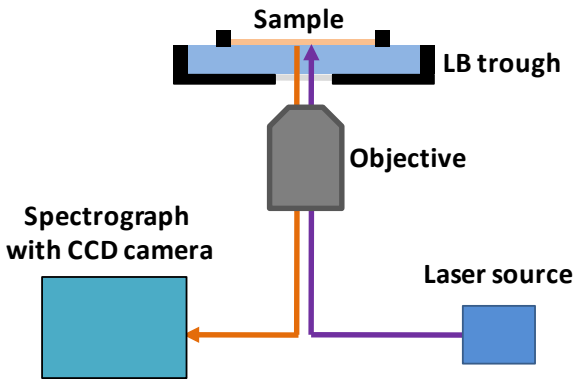

Figure 4.3 Schematic representation of Molecular-fluorescence spectroscopy.

4.2.4 DFT calculations. A model with oligothiophene of three monomers was built to simulate the stretching process of the PT chain. B3LYP/6-311++G** implemented in the G09 software package (http://www.gaussian.com/g_tech/g_ur/m_citation.htm) was applied to optimize the mode geometry as well as scan the 1-dimension stretching process. Both stretching two end hydrogen atoms and two end carbon atoms with the scan step size of 0.02 Angstrom in the oligothiophene molecule show very similar geometries and the computed HOMO-LUMO gap changes. We also simulated the entire process with the implicit solvent model (i.e., IEFPCM), which agrees with the observed phenomena in the gas phase calculations. As such, in Figure 4.8, we illustrated how the HOMO-LUMO gap that is analogous to the energy band gap of PT can be changed when stretching two end carbon atoms in gas phase. The molecular tension is computed by the vector length of analytical forces on two end carbon atoms depending on which atoms are stretched.

4.3 Results and Discussion

To investigate the effects of tension on optical properties, we measured their fluorescence emission spectra of PT bottlebrushes at the surface of water/2-propanol mixture in a LB trough. As shown previously,[22-23] the tension along the backbone in molecular bottlebrushes adsorbed to a flat substrate can be expressed as $f \cong S \cdot d$ at zero film pressure ($\Pi = 0$), where d is the width of the adsorbed bottlebrushes (Figure 1). The spreading parameter $S = \gamma_{sg} - (\gamma_{sl} + \gamma_{lg})$ is the difference between the interfacial energies for the substrate/gas (sg), substrate/liquid (sl), and liquid/gas (lg) interfaces. The spreading parameter was determined from the surface pressure-molecular area isotherms measured at high compressions, i.e. for thick films, using a LB trough (Figure 6).[30] While at non-zero film pressure, the expression can be modified as

$$f \cong (S - \Pi) \cdot d$$

The equation above provides us three ways to tune the backbone tension: side chain length, pressure and spreading parameter, as discussed below.

4.3.1 Effect of side chain length. First of all, we investigated the effect of side chain length. As showed in Figure 4.4a and c, for the bottlebrush samples from PT-5 to PT-190, the intensity decreases with side chain length under the same film pressure of 0.4 mN/m, due to the decrease of the fraction of PT backbone. The moles of excited PT backbones at the surface are roughly proportional to 1/d, and thus the FL intensity per thiophene unit should be proportional to $I_{max} \times d$, where I_{max} is the maximum intensity. Ideally, the FL intensity per thiophene unit should be the same for all PT bottlebrush samples, but it fluctuates due to many factors, such as imperfection of film homogeneousness and photobleaching (Appendix VI). On the contrary, the intensity of MI is even much lower than that of PT-190, which could be ascribed to the interaction between PT chains in a dense film of MI in favor of

nonradiative pathways for relaxation.[11,31] This did not occur for the bottlebrush samples since the densely grafted side chains prevent PT backbones getting close to each other. In Figure 4.4b, PT bottlebrushes with grafted side chains (e.g. PT-5) show a blue shifts (ca. 25 nm) of $\lambda_{max,em}$ compared to MI, which are much larger than that (ca. 5 nm) in solution. It could also result from the interaction between MI chains leading to the decrease of its energy band gap.

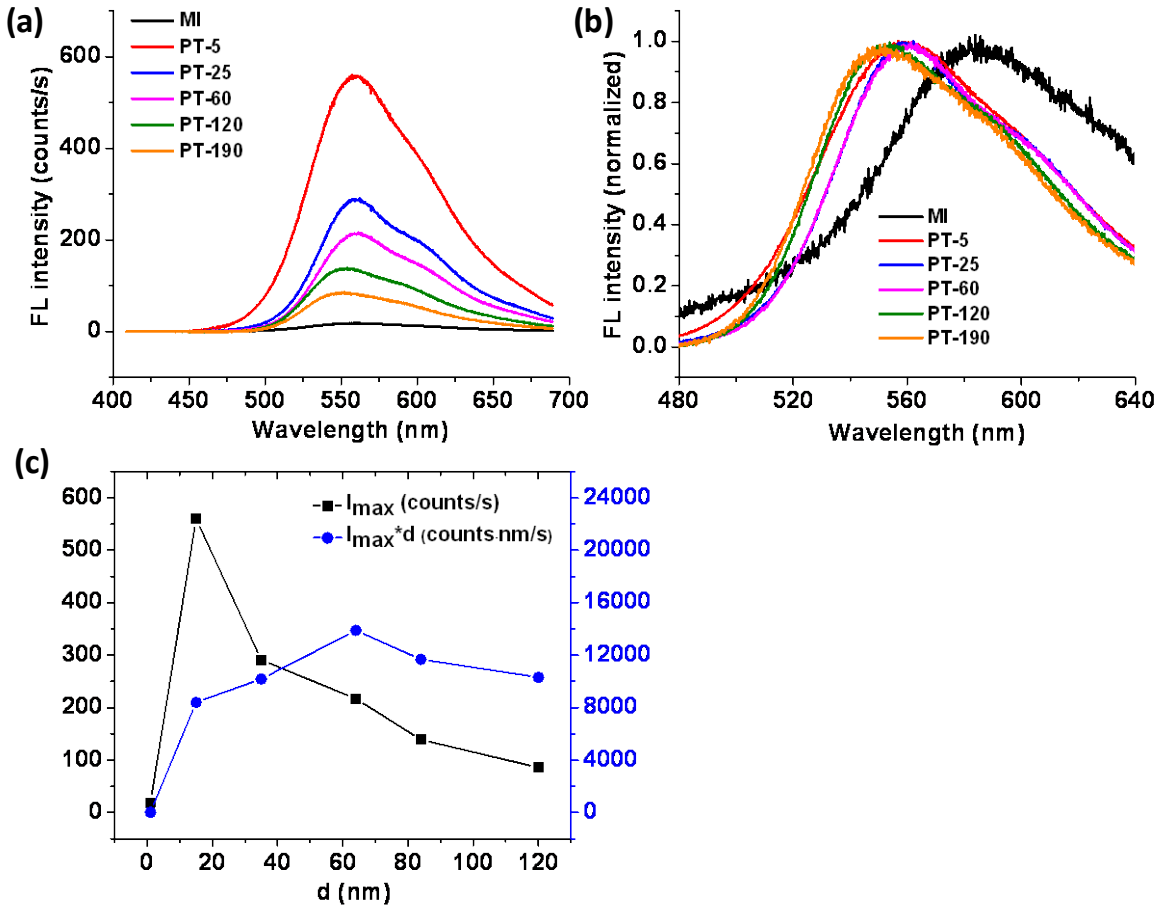

Figure 4.4 (a) FL spectra of PT bottlebrushes with different side chain lengths on 0.5% 2-propanol substrate at film pressure of 0.4 mN/m; (b) normalized FL spectra corresponding to (a); (c) maximum intensity versus the width of PT bottlebrush.

4.3.2 Effect of film pressure and substrate. Subsequently, we investigated the effect of film pressure on FL spectra of PT bottlebrush samples. As an example, Figure 5 shows the FL spectra of PT-60 at different film pressures on the same substrate of 0.5% 2-propanol.

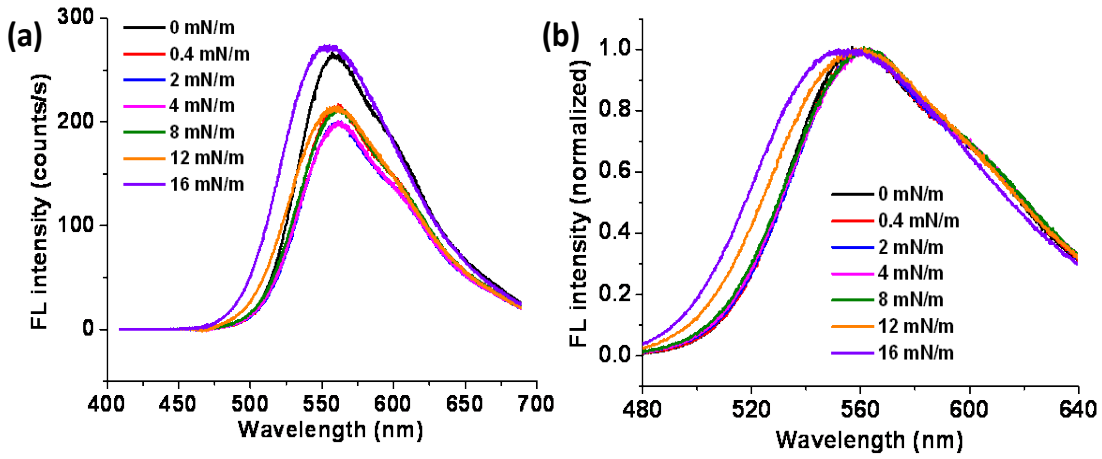

Figure 4.5 (a) FL spectra of PT-60 on 0.5% 2-propanol substrate at different film pressures; (b) normalized FL spectra corresponding to (a).

Ideally, the intensity is supposed to increase with film pressure. However, there is no obvious trend due to the reasons mentioned before. At low pressures, the spectra have a main peak at ~550 nm (short bottlebrushes) and a shoulder at ~600 nm (long bottlebrushes), which may be attributed to the large PDI of the PT backbones. As film pressure increases, the shoulder eventually disappears due to conformational transition of the bottlebrush molecules from extended to folded and twisted chains, especially for the long ones (Figure 4.6). Unlike PBA bottlebrushes with flexible backbone of full C-C bonds, the PT bottlebrushes did not collapse into globules because of the rigidity of PT backbones.[30] With respect to the broadening and shift of the peaks, we will discuss in detail in the following paragraphs.

We have also measured the FL spectra PT-60 and PT-190 on different substrates, e.g. 0.3% 2-propanol and 0.7% 2-propanol, whereas they are not showed here.

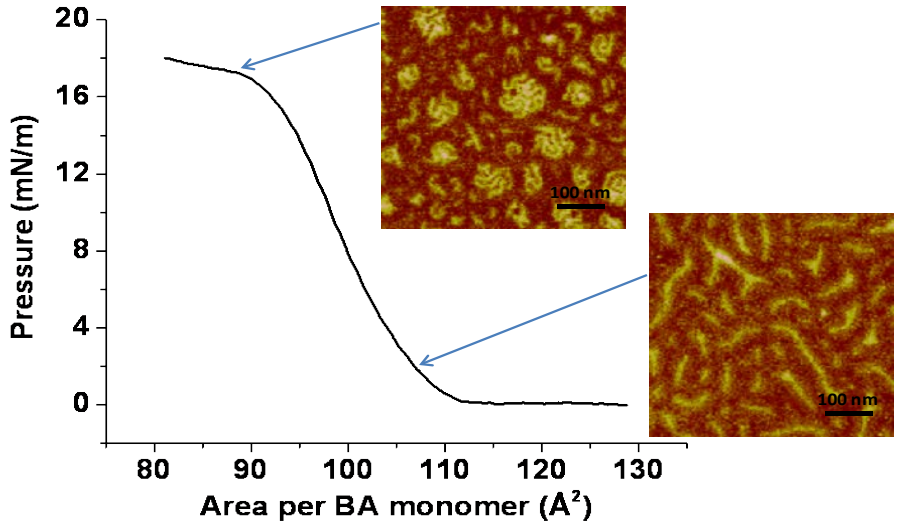

Figure 4.6 Pressure-molecular area isotherm for PT-60 bottlebrushes on 0.5/99.5% 2-propanol/water mixture. AFM micrographs of monolayers of PT-60 bottlebrushes transferred onto freshly cleaved mica substrates at 17 mN/m and 2 mN/m, respectively.

4.3.3 Energy band gap and full width at half maximum intensity (FWHM) vs. tension.

Summarizing all the experimental results, we are able to correlate the energy band gap of PT backbone approximated from $\lambda_{max,em}$ and FWHM with backbone tension (Figure 4.7).

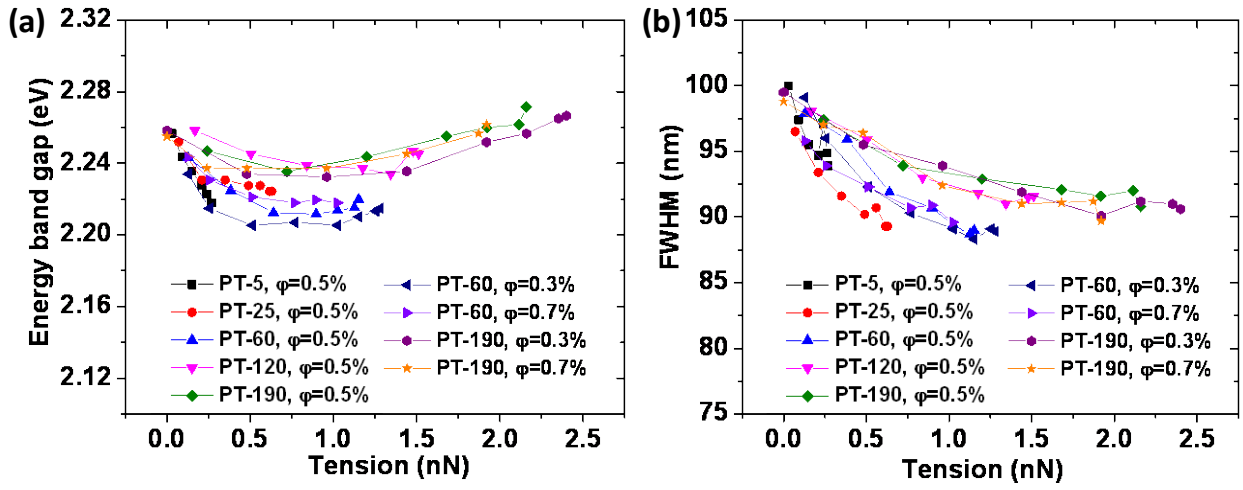

Figure 4.7 changes of energy band gap of PT backbone (a) and FWHM (b) with tension. φ is the weight fraction of 2-propanol in the substrate.

As shown in Figure 4.7a, the energy band gap decreases with backbone tension first, and then increases after the tension reaches a certain threshold (ca. 1.0 nN). Although there is difference of energy band gap between different data sets, which might be due to effects of solvents and chemical environment of the backbone, we attribute the decrease of energy band gap to the increase of conjugation length[32] and its increase to the deformation of the bonds in the backbone respectively, which will be discussed in comparison with theoretical prediction in the next section. One could also notice that the decrease of energy band gap is larger for PT bottlebrushes with shorter side chains than that for PT bottlebrushes with longer side chains, roughly. This might be because the conformation of the latter is more difficult to be disturbed (Appendix VII). In Figure 4.7b, the FWHM decreases as backbone tension increases (i.e. film pressure decreases) before a certain threshold tension is reached, which could be ascribed to the decrease of intramolecular interaction within the backbones switching from folded and twisted to extended conformation.[33] After the threshold point, the FWHM levels off. Surprisingly, the threshold tension agrees with that for the changes of energy band gap with backbone tension in Figure 4.7a.

4.3.4 Theoretical prediction. We have used a model with oligothiophene of three monomers to simulate stretching process of the PT backbone based on DFT. The HOMO-LUMO gap changes exhibit a “V” shape when the tension is increased from 0 nN to 5 nN (Figure 4.8). In other words, the gap is first decreased from 3.5 eV to 3.43 eV when the tension is increased from 0 to 1.7 nN. After this threshold tension point, the gap is increased monotonically with respect to the applied tension. More interestingly, the gap change behaviors are strongly correlated to geometric changes of the oligothiophene molecule. Without tension, the molecule is distorted with the Cs symmetry (Figure 4.8). When increasing the tension, the

conformation of the oligothiophene molecule is gradually changed to a completely planar geometry while the minimal HOMO-LUMO gap is reached. After the conformation is planar, the gap is always increased with respect to the large molecular tension. This "V" shape phenomena of the HOMO-LUMO gap qualitatively agree with the observations from experiments (Figure 4.7a).

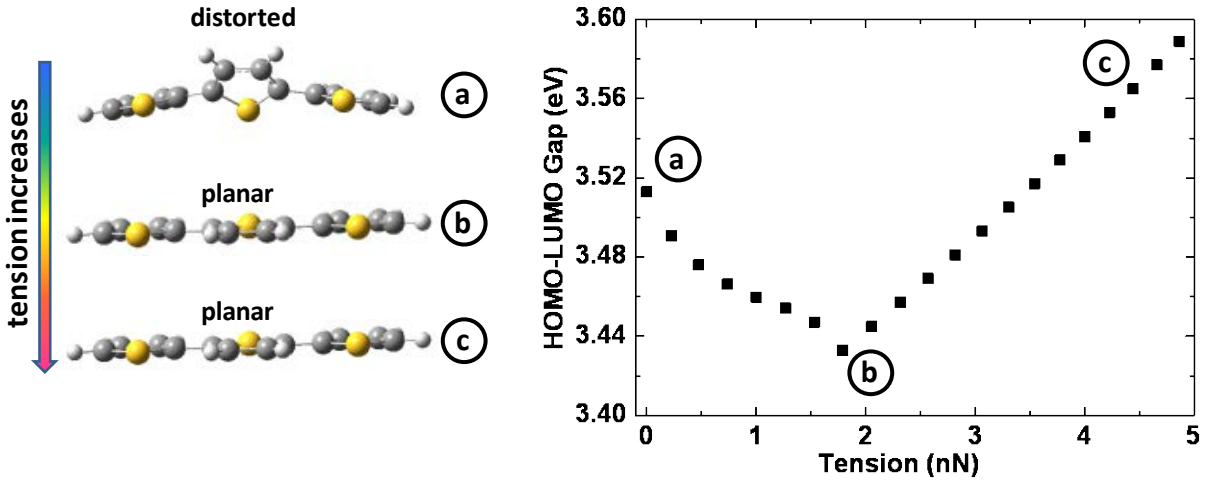

Figure 4.8 Conformational change of oligothiophene molecule of three monomers with increasing applied tension (left). HOMO-LUMO gap changes exhibit a "V" shape with tension increasing from 0 nN to 5 nN (right).

Understanding the geometry and structure changes with tension, we shall revisit the experimental results in Figure 4.7. As the backbone tension increases from 0 to ~1.0 nN, the conjugation length of the PT backbone is increased due to conformational changes from two processes: (i) the folded and twisted backbone is gradually extended, and (ii) the dihedral angles between neighboring thiophene rings become more and more planar, leading to the decrease of energy band gap. These two processes may occur simultaneously. At the threshold tension point, the planarity of PT backbone reaches its limit and therefore there is no further increase of conjugation length. Afterwards, the energy band gap increases with

applied tension due to the deformation of bond length and angles within the thiophene rings (Appendix VIII). From the view of electronic structures, we believe that the vibrational energy levels in the ground state are lowered more than the lowest vibrational level in the excited singlet state when applied tension is increased, resulting in the increase of energy band gap. Although the change is small, it is in good agreement with the theoretical predication. In fact, the bonds are also deformed before the threshold point, increasing the energy band gap, but the effect of conjugation dominates leading to a net decrease. In addition, the experimental threshold tension (ca. 1.0 nN) is smaller than that predicted (1.7 nN) for the fully planar oligothiophene, which might be attributed to the fact that the PT backbone could not be stretched to a fully planar plane because of the repulsion between densely grafted side chains. To summarize up, both experimental observations and theoretical predication suggest that molecular tension can be utilized to optimize optical properties of molecular bottlebrushes with PT backbones by tuning molecular conformations.

4.4 Conclusions

We used PT bottlebrushes as molecular tensile machines to study the effects of tension on the optical properties of conjugated polymers (e.g. PT in this contribution). We measured the fluorescence spectra of PT bottlebrush sub-monolayers on substrates of water/2-propanol mixtures under controlled backbone tension by controlling the side chain length, film pressure and spreading parameter of the bottlebrushes on the substrates. The energy band gap of PT backbone decreases before the threshold tension (ca. 1.0 nN) is reached, due to the increase of conjugation length which is the dominant effect over that of bond deformation. After the threshold point, the conjugation length of PT backbone could no longer be increased, and the deformation of bond length and angle starts to take effects, leading to the

increase of energy band gap. Although the changes in energy band gap with tension are small, they are in good and qualitative agreement with theoretical prediction by DFT based on the model of stretching a oligothiophene molecule of three monomers. This suggests that molecular tension can be utilized to optimize optical properties of molecular bottlebrushes with PT backbones by tuning molecular conformations.

References

(1) Caruso, M. M.; Davis, D. A.; Shen, Q.; Odom, S. A.; Sottos, N. R.; White, S. R.; Moore, J. S. *Chem. Rev.* **2009**, *109*, 5755-5798.

(2) Löwe, C.; Weder, C. *Advanced Materials* **2002**, *14*, 1625-1629.

(3) Crenshaw, B. R.; Weder, C. *Chemistry of Materials* **2003**, *15*, 4717-4724.

(4) Reneker, D. H.; Mattice, W. L.; Quirk, R. P.; Kim, S. J. *Smart Materials and Structures* **1992**, *1*, 84.

(5) Yoshino, K.; Nakao, K.; Onoda, M.; Sugimoto, R.-i. *Solid State Communications* **1988**, *68*, 513-516.

(6) Hess, B. C.; Kanner, G. S.; Vardeny, Z. *Physical Review B* **1993**, *47*, 1407-1411.

(7) Iwasaki, K.-i.; Fujimoto, H.; Matsuzaki, S. *Synthetic Metals* **1994**, *63*, 101-108.

(8) Davis, D. A.; Hamilton, A.; Yang, J.; Cremar, L. D.; Van Gough, D.; Potisek, S. L.; Ong, M. T.; Braun, P. V.; Martinez, T. J.; White, S. R.; Moore, J. S.; Sottos, N. R. *Nature* **2009**, *459*, 68-72.

(9) Ikawa, T.; Shiga, T.; Okada, A. *Journal of Applied Polymer Science* **1997**, *66*, 1569-1573.

(10) Yang, J.; Li, H.; Wang, G.; He, B. *Journal of Applied Polymer Science* **2001**, *82*, 2347-2351.

(11) Yang, G.; Li, Y.; White, J. O.; Drickamer, H. G. *J. Phys. Chem. B* **1999**, *103*, 5181-5186.

(12) Samuelsen, E. J.; Mårdalen, J.; Konestabo, O. R.; Hanfland, M.; Lorenzen, M. *Synthetic Metals* **1999**, *101*, 98-99.

(13) Muramatsu, Y.; Yamamoto, T.; Hasegawa, M.; Yagi, T.; Koinuma, H. *Polymer* **2001**, *42*, 6673-6675.

(14) Rubner, M. F. *Macromolecules* **1986**, *19*, 2129-2138.

(15) Stanford, J. L.; Young, R. J.; Day, R. J. *Polymer* **1991**, *32*, 1713-1725.

(16) Day, R. J.; Hu, X.; Stanford, J. L.; Young, R. J. *Polymer Bulletin* **1991**, *27*, 353.

(17) Sheiko, S. S.; Sun, F. C.; Randall, A.; Shirvanyants, D.; Rubinstein, M.; Lee, H.-i.; Matyjaszewski, K. *Nature* **2006**, *440*, 191-194.

(18) Lebedeva, N. V.; Sun, F. C.; Lee, H.-i.; Matyjaszewski, K.; Sheiko, S. S. *J. Am. Chem. Soc.* **2008**, *130*, 4228-4229.

(19) Park, I.; Sheiko, S. S.; Nese, A.; Matyjaszewski, K. *Macromolecules* **2009**, *42*, 1805-1807.

(20) Li, Y.; Nese, A.; Lebedeva, N. V.; Davis, T.; Matyjaszewski, K.; Sheiko, S. S. *J. Am. Chem. Soc.* **2011**, *133*, 17479-17484.

(21) Lebedeva, N. V.; Nese, A.; Sun, F. C.; Matyjaszewski, K.; Sheiko, S. S. *Proc. Natl. Acad. Sci. USA* **2012**, *109*, 9276-9280.

(22) Panyukov, S.; Zhulina, E. B.; Sheiko, S. S.; Randall, G. C.; Brock, J.; Rubinstein, M. *J. Phys. Chem. B* **2009**, *113*, 3750-3768.

(23) Panyukov, S. V.; Sheiko, S. S.; Rubinstein, M. *Phys. Rev. Lett.* **2009**, *102*, 148301.

(24) Park, I.; Nese, A.; Pietrasik, J.; Matyjaszewski, K.; Sheiko, S. S. *J. Mater. Chem.* **2011**, *21*, 8448-8453.

(25) Roncali, J. *Chem. Rev.* **1992**, *92*, 711-738.

(26) Dennler, G.; Scharber, M. C.; Brabec, C. J. *Advanced Materials* **2009**, *21*, 1323-1338.

(27) Sirringhaus, H. *Advanced Materials* **2005**, *17*, 2411-2425.

(28) Wang, M.; Zou, S.; Guerin, G.; Shen, L.; Deng, K.; Jones, M.; Walker, G. C.; Scholes, G. D.; Winnik, M. A. *Macromolecules* **2008**, *41*, 6993-7002.

(29) Sheiko, S. S.; Möller, M. *Chem. Rev.* **2001**, *101*, 4099-4124.

(30) Sun, F.; Sheiko, S. S.; Möller, M.; Beers, K.; Matyjaszewski, K. *The Journal of Physical Chemistry A* **2004**, *108*, 9682-9686.

(31) Yang, G.; Li, Y.; White, J. O.; Drickamer, H. G. *J. Phys. Chem. B* **1999**, *103*, 7853-7859.

(32) Bredas, J. L.; Silbey, R.; Boudreaux, D. S.; Chance, R. R. *J. Am. Chem. Soc.* **1983**, *105*, 6555-6559.

(33) Moses, D.; Feldblum, A.; Ehrenfreund, E.; Heeger, A. J.; Chung, T. C.; MacDiarmid, A. G. *Physical Review B* **1982**, *26*, 3361-3369.

Chapter 5

Molecular Imaging as a Tool for Quantitative Characterization of Molecular Dimensions and Conformation

5.1 Introduction

The work presented in Chapter 3 and 4 has focused on the study of tension effects on chemical reactions and optical properties, respectively. In the work showed in Chapter 3, atomic force microscopy (AFM) was used to follow the reaction progress by monitoring the average contour length of the molecular bottlebrushes. In fact, AFM can do much more, such as single molecule force spectroscopy,[1] structure and conformation study of polymers[2-3] and even measurement of molecular weight.[4] In this chapter, selected collaborative work with synthetic chemists will be presented. With the help of AFM, we can provide supplementary, yet important, information about their synthetic polymers beyond simple visualization (*e.g.* size, composition, and chain conformation), in addition to GPC, NMR spectroscopy and scattering techniques that measure average information.

5.2 Orthogonal self-assembly in folding block copolymers

Protein folding is a dynamic process of molecular self-assembly during which a single-stranded polypeptide chain folds to form a well-defined three dimensional (3D) tertiary structure, where orthogonal self-assembly is one of the essential features.[5-9] In this work, a series of ABA triblock copolymers that fold into single-chain polymeric nanoparticles (SCPNs) by intramolecular orthogonal self-assembly were synthesized (Figure 5.1). Either A, benzene-1,3,5-tricarboxamide (BTA),[10-11] or B, 2-ureido-4[1*H*]-pyrimidinone (UPy)[12]

moieties can induce single-chain folding under selected conditions. BTA is a well-explored helically self-assembling motif that forms aggregates through threefold-symmetric hydrogen bonding (Figure 5.1c). The Upy motif forms a dimer complex with a large equilibrium constant through complementary quadruple hydrogen bonding (Figure 5.1d). A molecular design approach combining both of these self-assembling motifs in a folding block copolymer would represent a significant milestone leading to synthetic protein analogues in which orthogonal self-assembly would induce folding of each block into internal segregated domains.

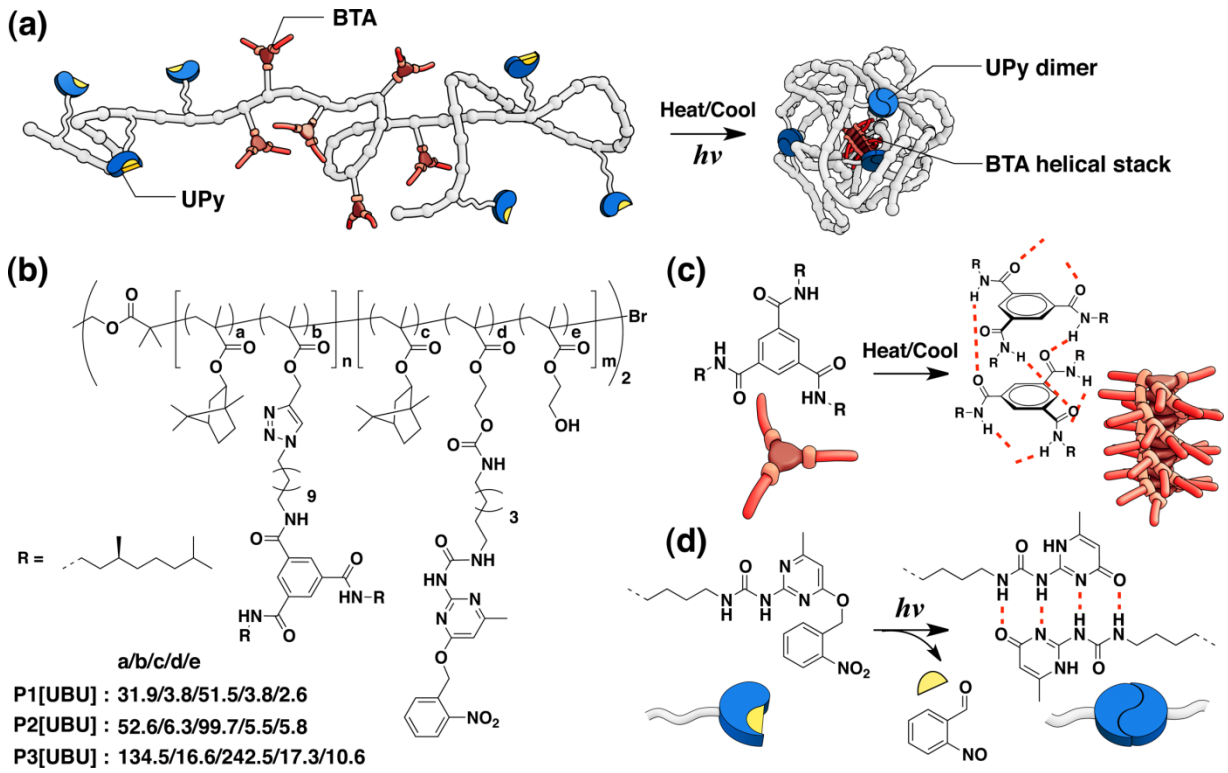

Figure 5.1 (a) Design of a triblock copolymer with BTA and UPy moieties folding into single-chain polymeric nanoparticle crosslinked via orthogonal self-assembly. (b) Chemical structure of the triblock copolymer, **P1[UBU]**, **P2[UBU]**, and **P3[UBU]**. (c) Helical self-assembly of chiral BTAs via three-fold hydrogen bonding. (d) Photoinduced dimer formation of *o*-nitrobenzyl protected UPys via quadruple hydrogen bonding.

Although the folding process was fully characterized using a combination of ^{1}H NMR and circular dichroism (CD) spectroscopy, size-exclusion chromatography (SEC), and small-angle X-ray scattering (SAXS), all the information collected was indirect proof for orthogonal self-assembly. Gratifyingly, AFM was also used to monitor the folding process on the molecular scale and provided a clear and direct view of the single-molecule nanostructures, as showed in Figure 5.2. Before UV irradiation, some individual chains adopted a "bead-tail" conformation, which is highly reminiscent of the "partly folded" state, in which only BTA moieties in the middle block self-assemble into internal helical stacks and partly collapse the polymer chain. Subsequently, UV irradiation triggered intramolecular Upy association resulting in complete collapse of individual polymer chains into nanoparticles. Direct visualization of the nanostructures in the folding process by AFM strongly supported our proposal that the triblock copolymers successfully demonstrate the controlled folding of synthetic polymers into compartmentalized SCPNs via orthogonal self-assembly.

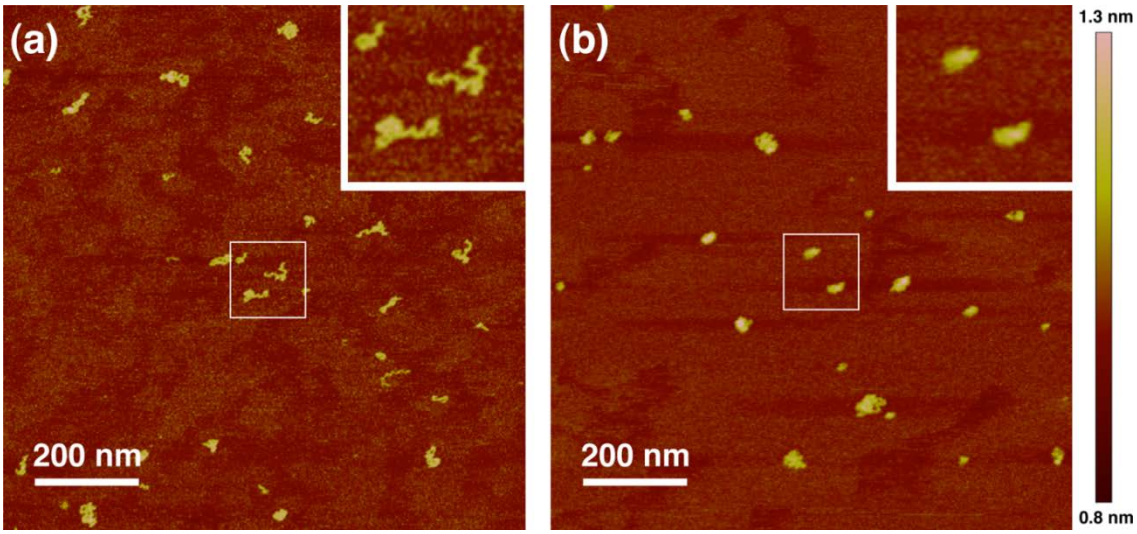

Figure 5.2 AFM height micrographs of **P3[UBU]** capture two-steps of molecular folding process (a) before and (b) after UV irradiation. The film samples were prepared by spin casting from dilute 1,2-dichloroethane solution on a mica substrate. The top-right insets show magnifications of the framed areas.

5.3 How far can we push polymer architectures?

Historically, polymeric architectures were limited to relatively simple structures like block copolymers, grafted polymers and polymer networks.[13-14] In the last decades, the progress in synthetic methodologies in conjunction with the use of conformational constraints has led to a better control over the size and shape of polymer architectures, as highlighted by the development of complex architectures such as dendrimers[15-16] and cylindrical brush polymers.[17] In addition, supramolecular interactions were effective in controlling polymer conformations, as demonstrated by the folding of individual polymer chains into well-defined discrete nanoparticles.[10,12,18-21] Also hybrids of several polymeric architectures have been explored leading to, for example, super-amphiphiles and protein-polymer conjugates.[22-24] In our search to the synthetic limits of controlling polymer architectures we started a joint project to include both a cylindrical brush polymer and single-chain polymeric nanoparticles within one polymer chain. Cylindrical brushes represent a new class of polymeric materials that feature self-assembly on mesoscales,[25-26] ultra-soft elastomers,[27] intramolecular mechanochemistry,[28-29] lubrication of cartilage,[30] and mucus clearance in lung airways.[31] Single-chain polymeric nanoparticles have recently attracted a considerable research interest as they allow for compartmentalized systems, which show interesting applications in catalysis and sensing.[11,32-33]

Here we present the synthesis and characterization of a block copolymer based on a polymer-brush block and on a hydrogen-bonded assisted folded polymer block. As a hydrogen-bonding moiety, we choose the ureido-pyrimidinone (UPy) group which is well-known for its ability to form strong, reversible, quadruple hydrogen bonds, making it an ideal candidate for the use in a wide range of self-assembly based applications.

The structural characteristics of the target block-copolymer requires a step-wise synthetic approach and combines different polymerization chemistries with post-modification strategies. The synthesis of the final polymers **4**, with a UV-labile protecting group on the UPy-unit, is presented in Scheme 5.1.

Scheme 5.1 Synthesis of brush-extended polymers 4c-4d

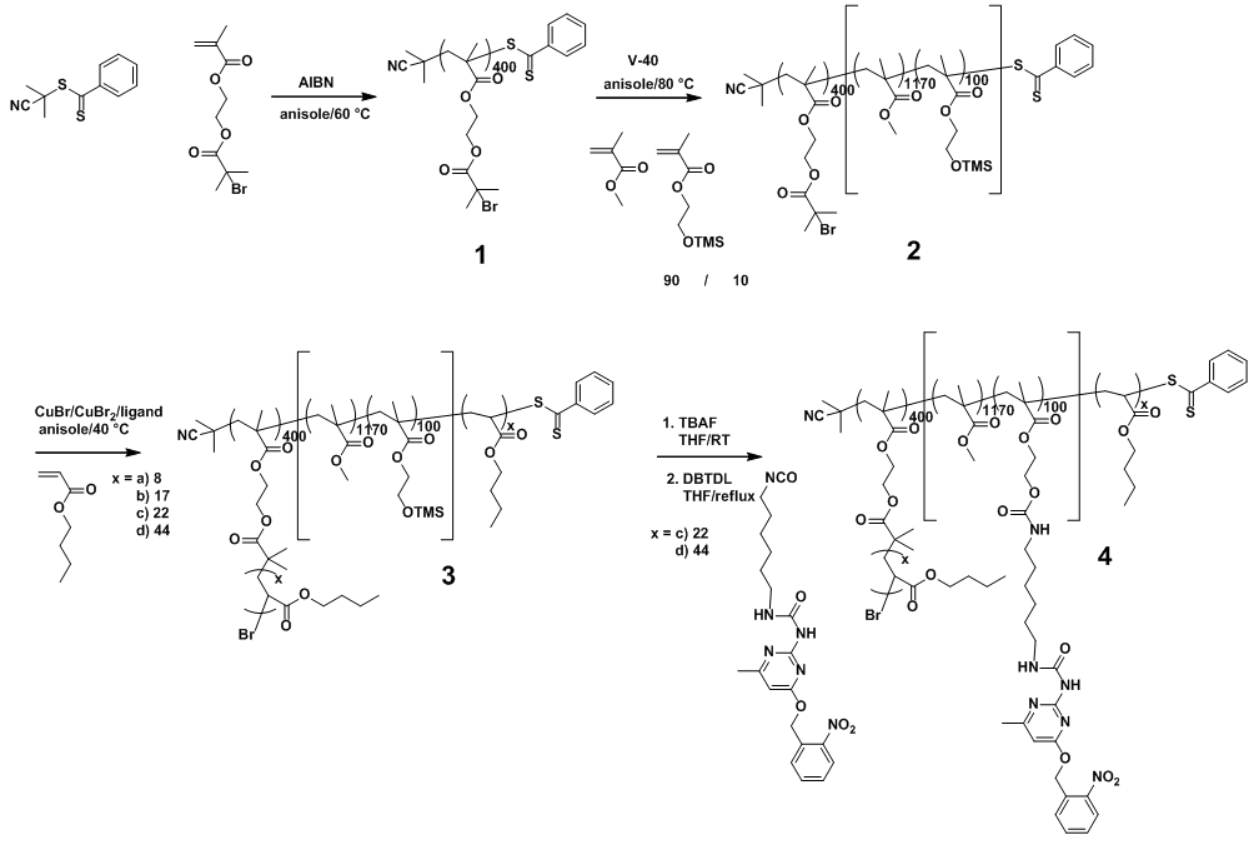

Finally, UV-irradiation of the precursors **4c, d** produced the final products **5c, d** in which a polymer brush is combined with a folded polymer (Figure 5.3).

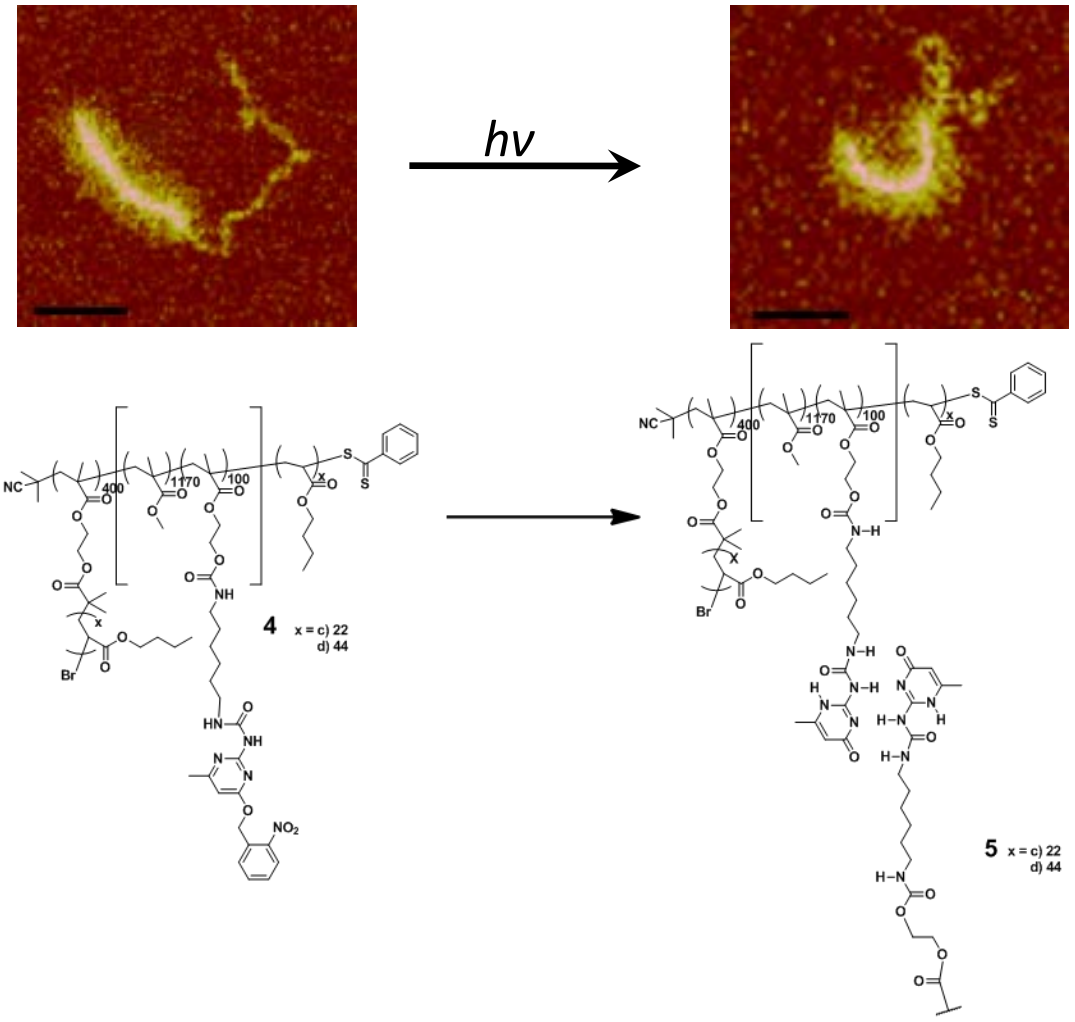

Figure 5.3 Polymer structures **4c-d and 5c-d** and representative AFM height micrographs of polymer **4d** (left) and **5d** (right); scale bar = 50 nm.

AFM studies of polymer **4c-d** (before deprotection) and polymer **5c-d** (after deprotection) on mica enabled precise imaging of the characteristic transformation from an unfolded to folded brush-block copolymer, respectively (Figure 5.4). The clear imaging of the linear block, as an individual randomly coiled polymer chain, is ascribed to strong adsorption on mica and anchoring to the brush block. AFM images after deprotection clearly show enhancement in folding of Upy-containing polymer block. As expected, the length of the brush grafts does not influence the folding behavior of the other block. Dynamic light

scattering (DSC) experiments as well as SEC, normally very informative for the folding process, do not show significant differences in the conversions of **4c, d** into **5c, d** after deprotection, since the vast majority of the mass is located in the brush segment. However, molecular imaging by AFM readily allows an accurate statistical analysis of large ensembles of block copolymers with respect to the length and radius of gyration (R_g). Analysis of the brush section of **5c** and **5d** furnished equal contour lengths for both polymers (87 and 85 nm, respectively), which was in excellent agreement with the estimated *DP* of this block. Additionally, the difference in the radius of gyration of the UPy-block before and after deprotection (25 ± 6 *vs.* 16 ± 3 nm, respectively for **4c** and **5c**, and 26 ± 7 *vs.* 20 ± 6 nm, respectively for **4d** and **5d**, Figure 5.5) was determined by tracing the linear-chain blocks of over 60 individual molecules.

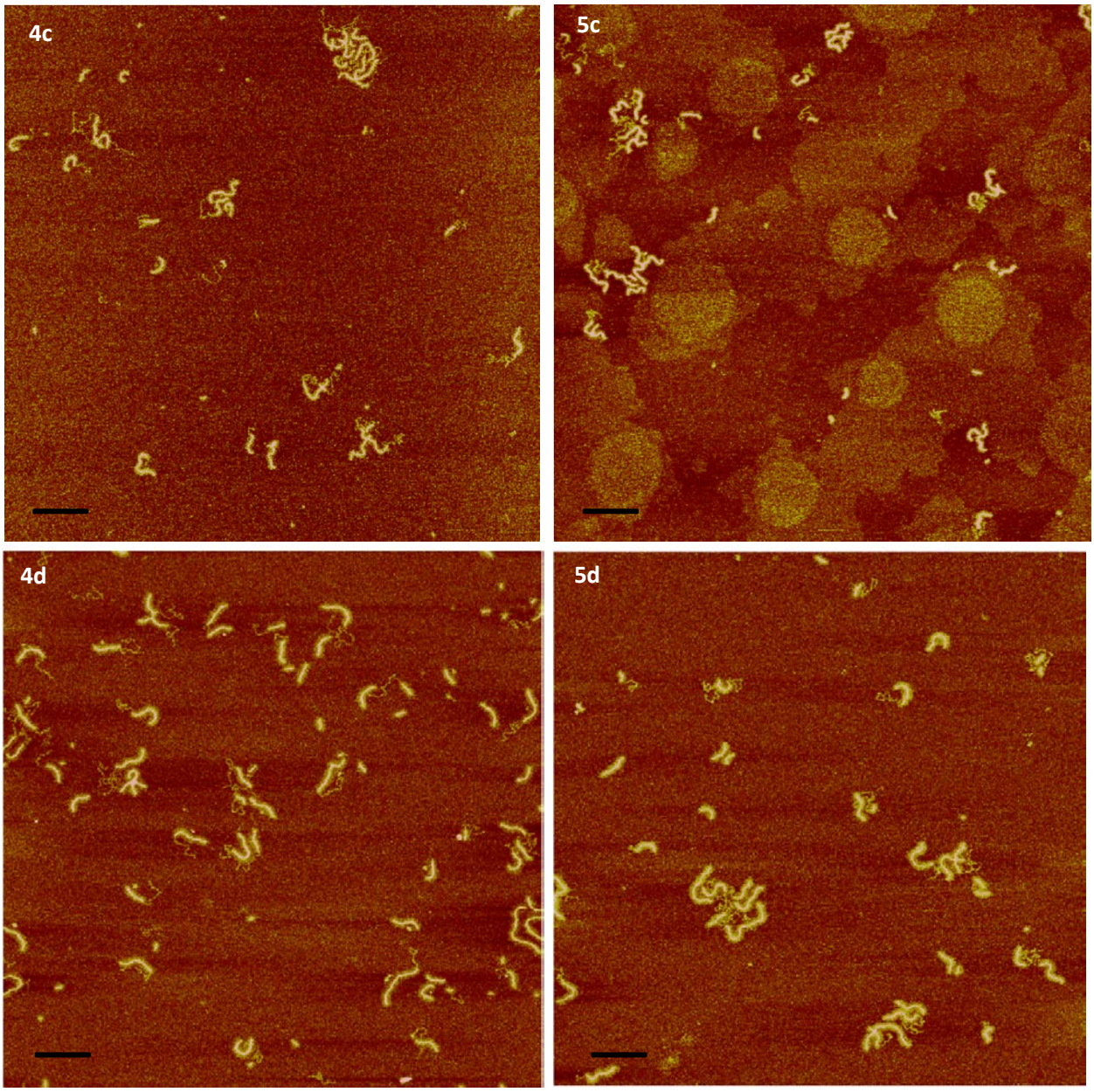

Figure 5.4 Representative AFM height micrographs of individual macromolecules of polymer **4c** (top left) and **5c** (top right), **4d** (bottom left) and **5d** (bottom right) adsorbed on a mica substrate. The samples were prepared by spin casting from dilute dichloroethane solution. Scale bar = 200 nm.

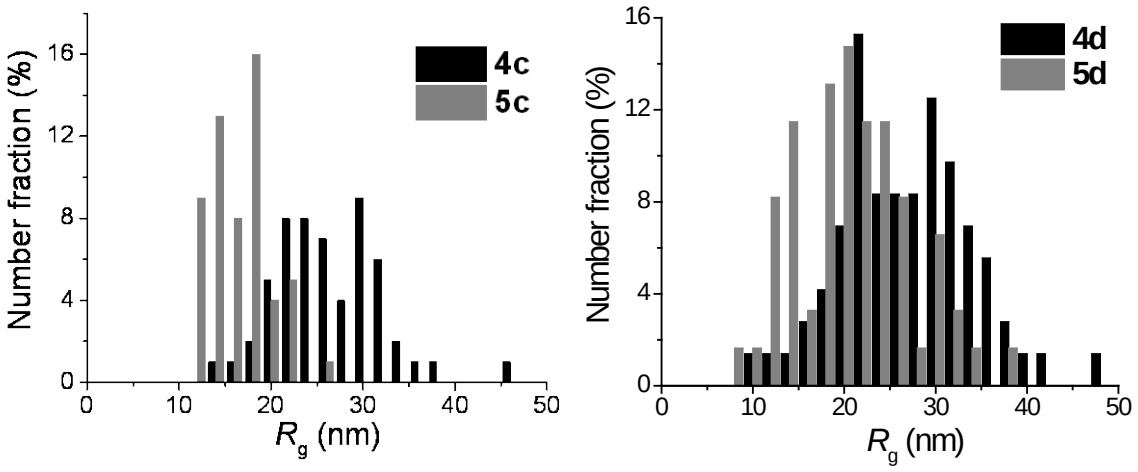

Figure 5.5 Changes in R_g for AFM micrographs in shown in Figure 5.4.

Due to unknown topology of intramolecular hydrogen bonding and complex nature of interactions between the substrate and polymer blocks the development of a theoretical model for quantitative analysis of molecular dimensions would be an ambiguous project. However, we can estimate an upper limit for the linear-block dimension by assuming hydrogen bonds were formed between neighboring UPy groups after deprotection. In this case, hydrogen bonding results in a chain which is approximately two times shorter (~L/2) and two times thicker, i.e., stiffer with a Kuhn length of ~2b, where L and b are the contour length and Kuhn length, respectively, of the linear-chain block before deprotection. Knowing that the scaling factor for real two-dimensional polymer chains is 0.75,[34] we estimate the ratio of the radius of gyration before deprotection to that after deprotection to be ~1.4, which is in good agreement with the experimental numbers (25/16 = 1.6 for **4c, 5c** and 26/20 = 1.3 for **4d, 5d**). As such, the AFM analysis of the block-copolymer on a surface is consistent with the behavior of the individual components in solution.

5.4 Molecular bottlebrushes prepared by iron based ATRP

Iron-based catalysts have been employed in controlled radical polymerization (CRP)[35] to synthesize well-defined homopolymers and copolymers.[36-43] The products of these iron-catalyzed reactions can be considered to be environmentally friendly polymers because iron is a nontoxic, readily available, and a low cost catalyst. ATRP using iron halides (Fe^nX_n) and tetrabutylammonium halide (TBAX) complexes were reported enabling well-controlled polymerization of methyl methacrylate (MMA) and styrene (St).[44-46]

In this work, we describe the first example of synthesis of molecular bottlebrushes having densely grafted poly(n-butylacrylate) (PBA), polystyrene (PS), or poly(di(ethylene glycol)ethyl ether acrylate)) (PDEGA) side chains by iron-based ATRP. The monomers were polymerized from a poly[2-(2-bromoisobutyryloxy)ethyl methacrylate] (PBiBEM) macroinitiator with a degree of polymerization in backbone of 400 (DP_{BB} = 400) using an iron(II) bromide ($Fe^{II}Br_2$), iron(III) bromide ($Fe^{III}Br_3$), and tetrabutylammonium bromide (TBABr) catalyst system (Scheme 5.2).

Scheme 5.2 Synthesis of molecular bottlebrushes by ATRP using iron catalyst and macroinitiator ($PBiBEM_{400}$) via grafting-from approach

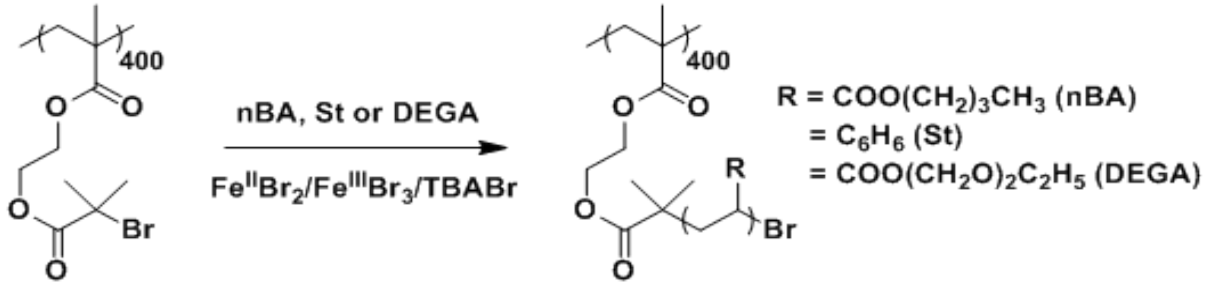

Molecular imaging by AFM provides useful information on the structure of the bottlebrush macromolecule, such as presence of intermolecular coupling or branching, in addition to direct measurement of the molecular dimensions including the length of backbone and side chains. Three different bottlebrushes were imaged by PeakForce QNM mode AFM.

Figure 5.6 exhibits AFM height images of PBiBEM$_{400}$-*g*-PBA$_{80}$, PBiBEM$_{400}$-*g*-PS$_{76}$, and PBiBEM$_{400}$-*g*-PDEGA$_{48}$.

The AFM scan reveals a densely packed Langmuir-Blodgett film of worm-like PBA and PDEGA bottlebrush macromolecules with less than *ca*. 10 % of intermolecular coupling, estimated by directly counting each molecule. This indicates that the iron catalyzed grafting-from polymerization progressed without significant levels of intermolecular termination even with a dense distribution of initiating sites. The number-average contour length (L_n) and length distribution (L_w/L_n) of backbone, the distance between molecules (bottlebrush width, *D*), and the molecular weight ($M_{n,AFM}$) were determined by the AFM-LB method.[4] The results are summarized in Table 5.1. A backbone $DP_{bb,\ AFM}$ = 510 was estimated from L_n, assuming a fully stretched backbone. The value was larger than $DP_{bb,GPC}$ = 400 determined by GPC for PMMA standard, which can be attributed to the difference of hydrodynamic volume of the backbone in GPC compared to the MMA standard. As shown in Table 5.1, the length distribution of backbone (L_w/L_n = 1.09-1.11) determined by the AFM-LB method was in agreement with M_w/M_n = 1.15 of PBiBEM macroinitiator. The distance (*D*) of 50 nm between the backbones of the PBA bottlebrush was larger than 45 nm determined for the PDEGA bottlebrush because of longer PBA side chain compared with PDEGA side chain. The molecular weights ($M_{n,AFM}$) of PBiBEM$_{400}$-*g*-PBA$_{80}$: 4.3 × 10^6 and PBiBEM$_{400}$-*g*-PDEGA$_{48}$: 3.5 × 10^6 obtained by the AFM-LB method were consistent with the absolute $M_{n,MALLS}$, PBiBEM$_{400}$-*g*-PBA$_{80}$: 4.1 × 10^6 and PBiBEM$_{400}$-*g*-PDEGA$_{48}$: 3.7 ×10^6, from MALLS.

It was not possible to apply the AFM-LB method to characterization of PS bottlebrushes (PBiBEM$_{400}$-*g*-PS$_{76}$) due to the lack of molecular resolution in LB-monolayers attributed to

weaker attraction of PS side-chains to the air/water interface leading to weaker extension and stronger aggregation of brush macromolecules. To image individual molecules of PS bottlebrushes, dilute solutions in chloroform were spin-cast onto a HOPG substrate. Worm-like macromolecules finely dispersed on the substrate were revealed by AFM. This sample preparation allowed accurate measurements of the number average contour length L_n =119±4 nm, width D=30 nm, and height h=2 nm (Table 5.1). The average contour length of PS bottlebrushes was slightly shorter than those of the PBA and PDEGA samples, indicating smaller extension of their backbones due to weaker attraction of the PS side-chains to HOPG.[47] The contour length distribution (L_w/L_n) was calculated to be 1.09, which agreed with the polydispersity (PDI) of PBiBEM macroinitiator.

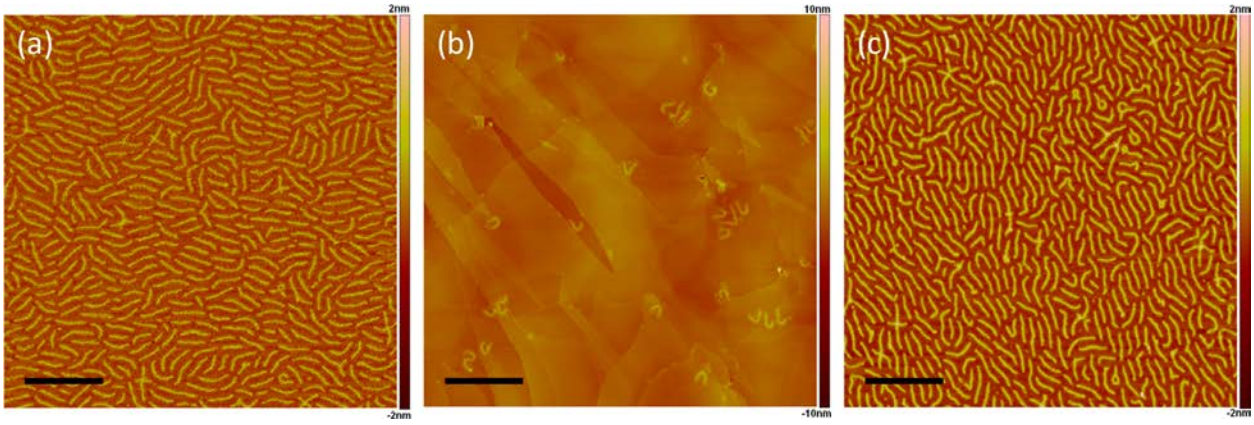

Figure 5.6 AFM height images of molecular bottlebrushes: (a) PBiBEM$_{400}$-g-PBA$_{80}$ transferred from air/water interface onto mica substrate, (b) PBiBEM$_{400}$-g-PS$_{76}$ spin cast onto highly oriented pyrolytic graphite (HOPG) substrate from dilute chloroform solution, and (c) PBiBEM$_{400}$-g-PDEGA$_{48}$ transferred from air/water interface onto mica substrate. Scale bar = 400 nm.

Table 5.1 Characterization of bottlebrush molecules

brush	L_n (nm)[a]	L_w/L_n	D (nm)[b]	$M_{n,AFM}$ [c] $\times 10^{-6}$	$M_{w,MALLS}$ [e] $\times 10^{-6}$	$M_{n,MALLS}$ [e] $\times 10^{-6}$	M_w / M_n [f]
$PBiBEM_{400}$-*g*-PBA_{80}	130 ± 2	1.09	50	4.3	4.17	4.12	1.18
$PBiBEM_{400}$-*g*-PS_{76}	119±4	1.09	30	NA[d]	4.22	4.03	1.22
$PBiBEM_{400}$-*g*-$PDEGA_{48}$	126 ± 2	1.11	45	3.5	3.83	3.71	1.28

[a]Number average contour length. [b]Width of molecular bottlebrush. [c]Number average molecular weight by AFM-LB method. [d]The AFM-LB method could not be applied due to the lack of molecular resolution in LB-monolayers of PS bottlebrushes. [e] M_w and M_n based on MALLS in THF using dn/dc=0.069 (PBA), 0.176 (PS), and 0.085 mL/g (PDEGA). [f] M_w / M_n based on GPC in THF for poly(methyl methacrylate) (PMMA) standard.

5.5 Conclusions

Selected collaborative work has been presented in this chapter, which demonstrates that AFM is a powerful tool for molecular imaging and conformation study. AFM can provide direct visualization of single molecules and beyond that, useful and unique information about their size distribution, conformation and even molecular weight can be obtained. This supplementary information, in addition to GPC, NMR spectroscopy and scattering techniques that measure average information, can help synthetic chemists to further confirm their success in synthesizing final products.

References

(1) Neuman, K. C.; Nagy, A. *Nature Methods* **2008**, *5*, 491-505.

(2) Kumaki, J.; Nishikawa, Y.; Hashimoto, T. *J. Am. Chem. Soc.* **1996**, *118*, 3321-3322.

(3) Sheiko, S. S.; Möller, M. *Chem. Rev.* **2001**, *101*, 4099-4124.

(4) Sheiko, S. S.; da Silva, M.; Shirvaniants, D.; LaRue, I.; Prokhorova, S.; Moeller, M.; Beers, K.; Matyjaszewski, K. *J. Am. Chem. Soc.* **2003**, *125*, 6725-6728.

(5) Anfinsen, C. B. *Science* **1973**, *181*, 223-230.

(6) Whitesides, G.; Mathias, J.; Seto, C. *Science* **1991**, *254*, 1312-1319.

(7) Rief, M.; Gautel, M.; Oesterhelt, F.; Fernandez, J. M.; Gaub, H. E. *Science* **1997**, *276*, 1109-1112.

(8) Dobson, C. M. *Nature* **2003**, *426*, 884-890.

(9) Lindorff-Larsen, K.; Piana, S.; Dror, R. O.; Shaw, D. E. *Science* **2011**, *334*, 517-520.

(10) Mes, T.; van der Weegen, R.; Palmans, A. R. A.; Meijer, E. W. *Angew. Chem., Int. Ed.* **2011**, *50*, 5085-5089.

(11) Terashima, T.; Mes, T.; De Greef, T. F. A.; Gillissen, M. A. J.; Besenius, P.; Palmans, A. R. A.; Meijer, E. W. *J. Am. Chem. Soc.* **2011**, *133*, 4742-4745.

(12) Foster, E. J.; Berda, E. B.; Meijer, E. W. *J. Am. Chem. Soc.* **2009**, *131*, 6964-6966.

(13) Matyjaszewski, K. *Science* **2011**, *333*, 1104-1105.

(14) Matyjaszewski, K.; Gnanou, Y.; Leibler, L. *Macromolecular Engineering: Precise Synthesis, Materials Properties, Applications*; Wiley-VCH: Weinheim, 2007.

(15) Tomalia, D. A. *Progress in Polymer Science* **2005**, *30*, 294-324.

(16) Astruc, D.; Boisselier, E.; Ornelas, C. *Chem. Rev.* **2010**, *110*, 1857-1959.

(17) Sheiko, S. S.; Sumerlin, B. S.; Matyjaszewski, K. *Prog. Polym. Sci.* **2008**, *33*, 759-785.

(18) Cherian, A. E.; Sun, F. C.; Sheiko, S. S.; Coates, G. W. *J. Am. Chem. Soc.* **2007**, *129*, 11350-11351.

(19) Seo, M.; Beck, B. J.; Paulusse, J. M. J.; Hawker, C. J.; Kim, S. Y. *Macromolecules* **2008**, *41*, 6413-6418.

(20) Altintas, O.; Barner-Kowollik, C. *Macromolecular Rapid Communications* **2012**, *33*, 958-971.

(21) Appel, E. A.; Dyson, J.; del Barrio, J.; Walsh, Z.; Scherman, O. A. *Angew. Chem., Int. Ed.* **2012**, *51*, 4185-4189.

(22) Nicolas, J.; Mantovani, G.; Haddleton, D. M. *Macromolecular Rapid Communications* **2007**, *28*, 1083-1111.

(23) Lutz, J.-F.; Börner, H. G. *Progress in Polymer Science* **2008**, *33*, 1-39.

(24) Börner, H. G. *Progress in Polymer Science* **2009**, *34*, 811-851.

(25) Xia, Y.; Olsen, B. D.; Kornfield, J. A.; Grubbs, R. H. *J. Am. Chem. Soc.* **2009**, *131*, 18525-18532.

(26) Rzayev, J. *ACS Macro Letters* **2012**, *1*, 1146-1149.

(27) Pakula, T.; Zhang, Y.; Matyjaszewski, K.; Lee, H.-i.; Boerner, H.; Qin, S.; Berry, G. C. *Polymer* **2006**, *47*, 7198-7206.

(28) Sheiko, S. S.; Sun, F. C.; Randall, A.; Shirvanyants, D.; Rubinstein, M.; Lee, H.-i.; Matyjaszewski, K. *Nature* **2006**, *440*, 191-194.

(29) Panyukov, S.; Zhulina, E. B.; Sheiko, S. S.; Randall, G. C.; Brock, J.; Rubinstein, M. *J. Phys. Chem. B* **2009**, *113*, 3750-3768.

(30) Greene, G. W.; Banquy, X.; Lee, D. W.; Lowrey, D. D.; Yu, J.; Israelachvili, J. N. *Proceedings of the National Academy of Sciences* **2011**, *108*, 5255-5259.

(31) Button, B.; Cai, L.-H.; Ehre, C.; Kesimer, M.; Hill, D. B.; Sheehan, J. K.; Boucher, R. C.; Rubinstein, M. *Science* **2012**, *337*, 937-941.

(32) Huerta, E.; Stals, P. J. M.; Meijer, E. W.; Palmans, A. R. A. *Angew. Chem., Int. Ed.* **2012**, n/a-n/a.

(33) Gillissen, M. A. J.; Voets, I. K.; Meijer, E. W.; Palmans, A. R. A. *Polymer Chemistry* **2012**, *3*, 3166-3174.

(34) Rubinstein, M.; Colby, R. H. *Polymer Physics*; Oxford University Press: Oxford, 2003.

(35) Braunecker, W. A.; Matyjaszewski, K. *Progress in Polymer Science* **2007**, *32*, 93-146.

(36) Ando, T.; Kamigaito, M.; Sawamoto, M. *Macromolecules* **1997**, *30*, 4507-4510.

(37) Matyjaszewski, K.; Wei, M.; Xia, J.; McDermott, N. E. *Macromolecules* **1997**, *30*, 8161-8164.

(38) Zhu, S.; Yan, D. *Macromolecules* **2000**, *33*, 8233-8238.

(39) O'Reilly, R. K.; Gibson, V. C.; White, A. J. P.; Williams, D. J. *J. Am. Chem. Soc.* **2003**, *125*, 8450-8451.

(40) Xue, Z.; Linh, N. T. B.; Noh, S. K.; Lyoo, W. S. *Angew. Chem., Int. Ed.* **2008**, *47*, 6426-6429.

(41) Wang, Y.; Matyjaszewski, K. *Macromolecules* **2010**, *43*, 4003-4005.

(42) Wang, Y.; Matyjaszewski, K. *Macromolecules* **2011**, *44*, 1226-1228.

(43) Wang, Y.; Kwak, Y.; Matyjaszewski, K. *Macromolecules* **2012**, *45*, 5911-5915.

(44) Teodorescu, M.; Gaynor, S. G.; Matyjaszewski, K. *Macromolecules* **2000**, *33*, 2335-2339.

(45) Wang, Y.; Zhang, Y.; Parker, B.; Matyjaszewski, K. *Macromolecules* **2011**, *44*, 4022-4025.

(46) Mukumoto, K.; Wang, Y.; Matyjaszewski, K. *ACS Macro Letters* **2012**, *1*, 599-602.

(47) Sun, F.; Sheiko, S. S.; Möller, M.; Beers, K.; Matyjaszewski, K. *The Journal of Physical Chemistry A* **2004**, *108*, 9682-9686.

Chapter 6

Uncompleted Studies and Proposed Future Work

6.1 Ultrasonic degradation of molecular bottlebrushes (in collaboration with Stephen Craig group at Duke)

Ultrasound is an important tool to study mechanochemistry and is widely used to apply force to dilute polymer solutions, leading to the scission of polymer chains. The mechanism for scission is solvodynamic shear caused by cavitation: the nucleation, growth, and collapse of bubbles in solution. Strong pressure waves are generated when a bubble collapses, pulling nearby polymer chains toward the cavity of the bubble, and the solvodynamic shear elongates the polymer chains, leading to scission.[1] Scission generally occurs near the midpoint of a polymer chain (approximately within the middle 15% of the chain, in the case of homopolymers), where solvodynamic forces are the greatest.[1-2]

Recently, sonication-induced scission of nanotubes, nanowires and filaments has also been studied.[3-4] The effects of their diameters were of particular interest, which is not discussed here. Inspired by these studies, we are interested to investigate sonication-induced scission of cylindrical molecular bottlebrush backbones with respect to their cross-sectional diameter (i.e. side chain length). The significance of this study is that the molecular bottlebrush system is different from nanotube, nanowire and filament systems by two facts: (i) molecular bottlebrushes are “soft” and (ii) the strength of the backbone does not depend on the length of side chains.

To qualify the effects of side chain length, two molecular bottlebrush samples with the same backbone but different side-chain degrees of polymerization (DP60 and DP100) were dissolved in tetrahydrofuran (THF, ~ 1mg/ml), and sonicated with ultrasonic pulse (20 kHz, 12 W/cm^2, 1 sec on/1 sec off) at 6-9 °C under nitrogen atmosphere (Figure 6.1a). Aliquots were removed periodically, and the scission of backbone was monitored by GPC with multi-angle light scattering (MALS) detector and AFM.

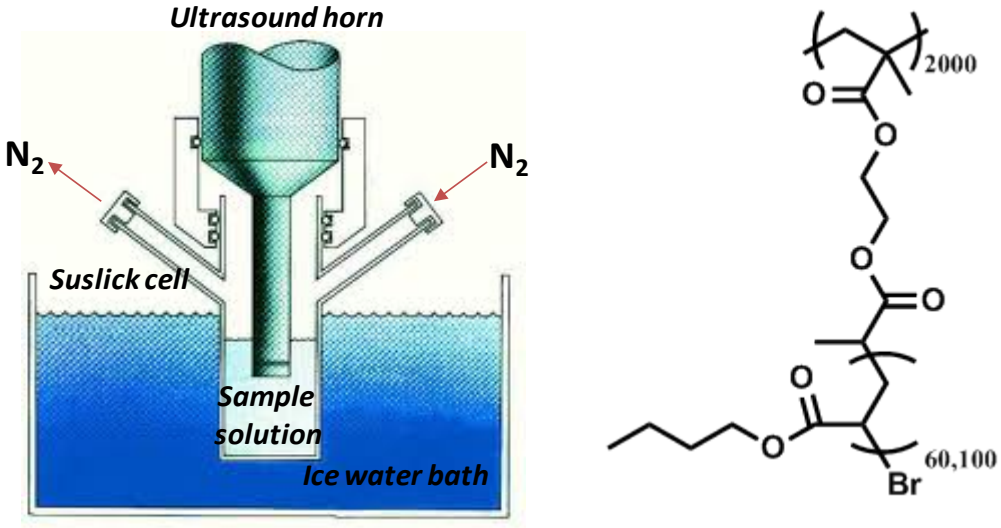

Figure 6.1 Typical ultrasound mechanochemistry experimental setup (left); chemical structure of the studied molecular bottlebrushes (right).

As showed in Figure 6.2, both molecular bottlebrushes became shorter as sonication proceeded, indicating the scission of bottlebrush backbones. The scission of side chains did not occur because their molecular weights were below the limit.[5] After sonication for 120 min, the bottlebrushes were believed to reach their limiting lengths, since the molecular weights did not change after 60 min (Figure 6.3a). The limiting length for DP100 (~40 nm) is shorter than that for DP 60 (~65 nm) as expected, which could be due to the larger force generated at the middle of the backbone of the bottlebrushes with longer side chains.[3]

However, more experiments need to be done to further confirm this effect and build a relation between the limiting length and the length of side chains.

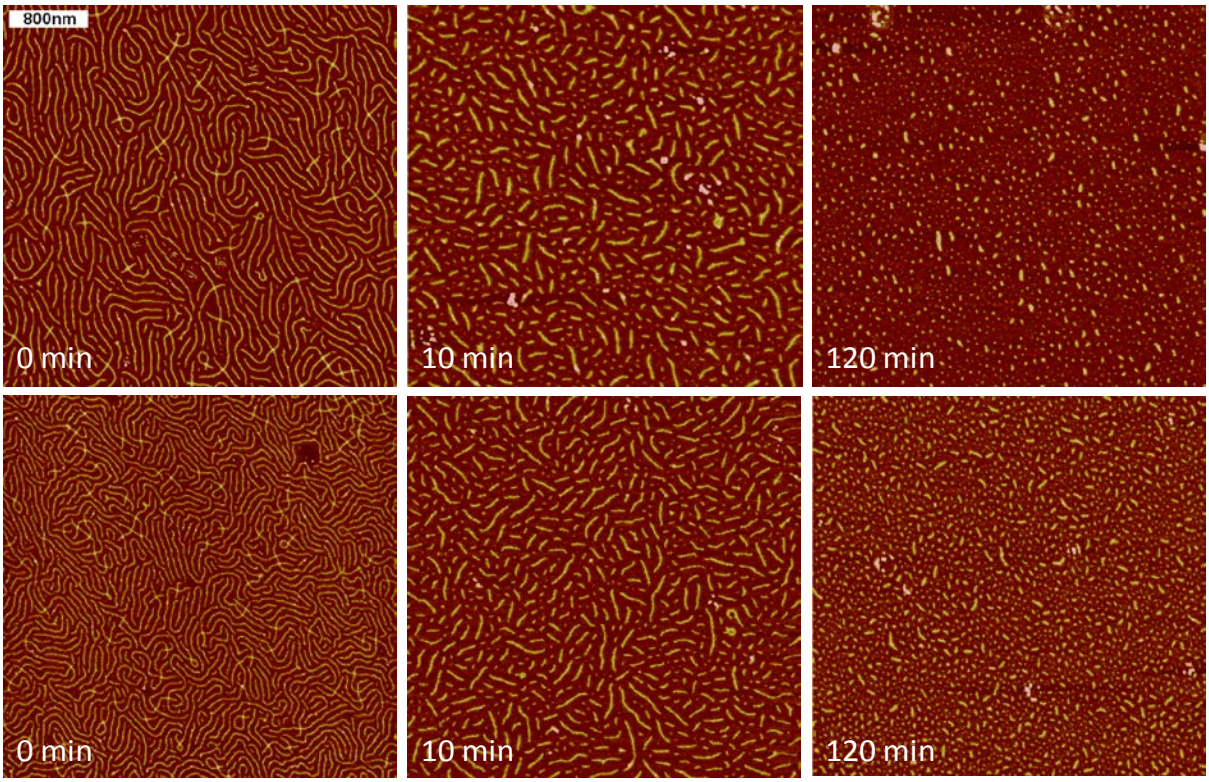

Figure 6.2 Representative AFM height micrographs of molecular bottlebrushes after different sonication times: DP100 (top) and DP60 (bottom). The size of the micrographs is the same.

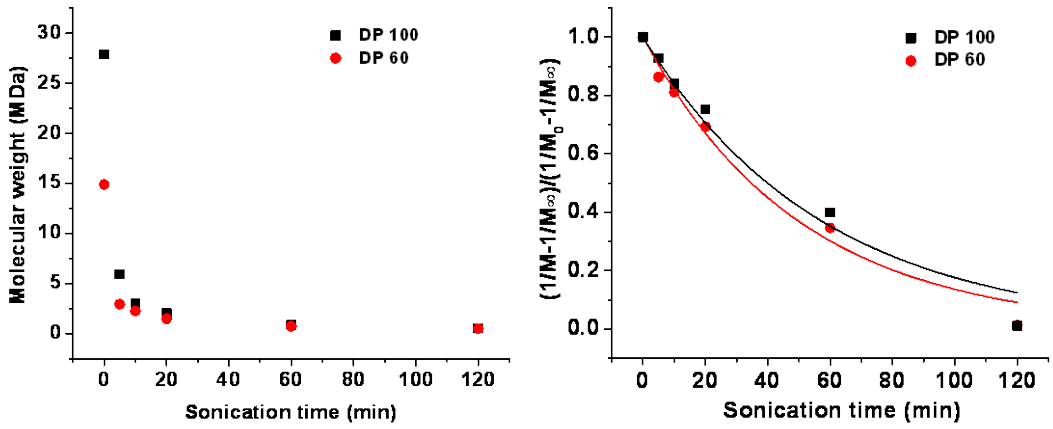

Figure 6.3 Molecular weight of both bottlebrush molecules decreases with sonication time (left); kinetics of sonication-induced scission, solid lines are exponential fits to the data points with eq. 6.1 (right).

Due to the complexity of sonication-induced scission process, analysis of the kinetics is not simple work. The scission rate depends on too many factors, e.g. initial and limiting molecular. Therefore different models have been developed to describe molecular weight evolution during sonication.[6] In this preliminary work, we choose a simple model proposed by Ovenall and co-workers

$$\frac{1/M-1/M_\infty}{1/M_0-1/M_\infty} = e^{-kt} \tag{6.1}$$

where M is the molecular weight at time t, M_0 and M_∞ are the initial and limiting molecular weights respectively, and $k = k_0 \frac{M_\infty}{cm_0}$ is the rate constant (c is polymer concentration, m_0 is monomer molecular weight). Eq. 6.1was used to fit the data points in Figure 6.3, yielding the rate constants of 0.02 min^{-1} and 0.017 min^{-1} for DP60 and DP100 respectively. The rate constants are very close, but one should note that they are dependent on limiting molecular weight. Due to the lack of data, comparison of sonication-induced scission rate constants of bottlebrush molecules with different side chain lengths are not discussed here.

For future work, more experiments need to be carried out, and a more sophisticated model should be used to quantitatively evaluate the effects of side chain length on the limiting molecular weight and scission rate.

6.2 Unclicking the click

Recently it has been reported that highly inert 1,2,3-triazole moiety that is the product of azide and alkyne “click” coupling within a poly(methyl acrylate) chain is susceptible to ultrasound-induced cycloreversion.[7] To test and verify this result, molecular bottlebrushes with 1,2,3-triazole in the middle of backbone were synthesized by ATRP and adsorbed onto 2-propanol/water surface for scission study.

The length of the bottlebrushes has bimodal distributions with two bands at ~130 nm and ~260 nm that correspond respectively to i) the full length of bottlebrushes with the intact 1,2,3-triazole linker and ii) bottlebrushes due to mid-chain scission of the linker (Figure 6.5). The population of the band at ~130 nm increased with time, indicating the mid-chain scission. However, mid-chain scission due to possibilities other than cycloreversion of 1,2,3-triazole could not be excluded. Therefore, as control experiments, the scission of molecular bottlebrushes with 1,2,4-triazole moiety in the middle of the backbone can be investigated. If mid-chain scission does not occur in the control experiments, one can conclude that 1,2,3-triazloe is susceptible to mechanically induced cycloreversion.

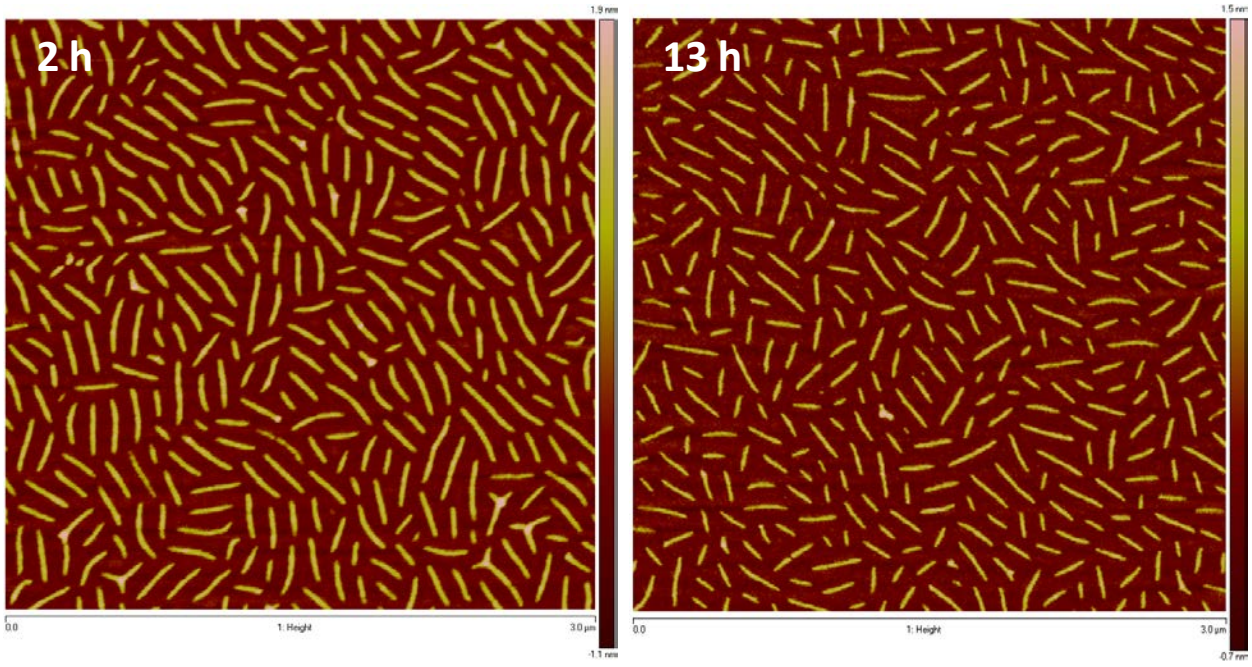

Figure 6.4 Representative AFM height micrographs of triazole molecular bottlebrushes with DP of PBA side chains of 128 after exposure to 2-propanol/water (0.3/99.7 wt/wt%) surface for different times. 2-propanol was added to control the backbone tension to suppress random scission of C-C bonds.

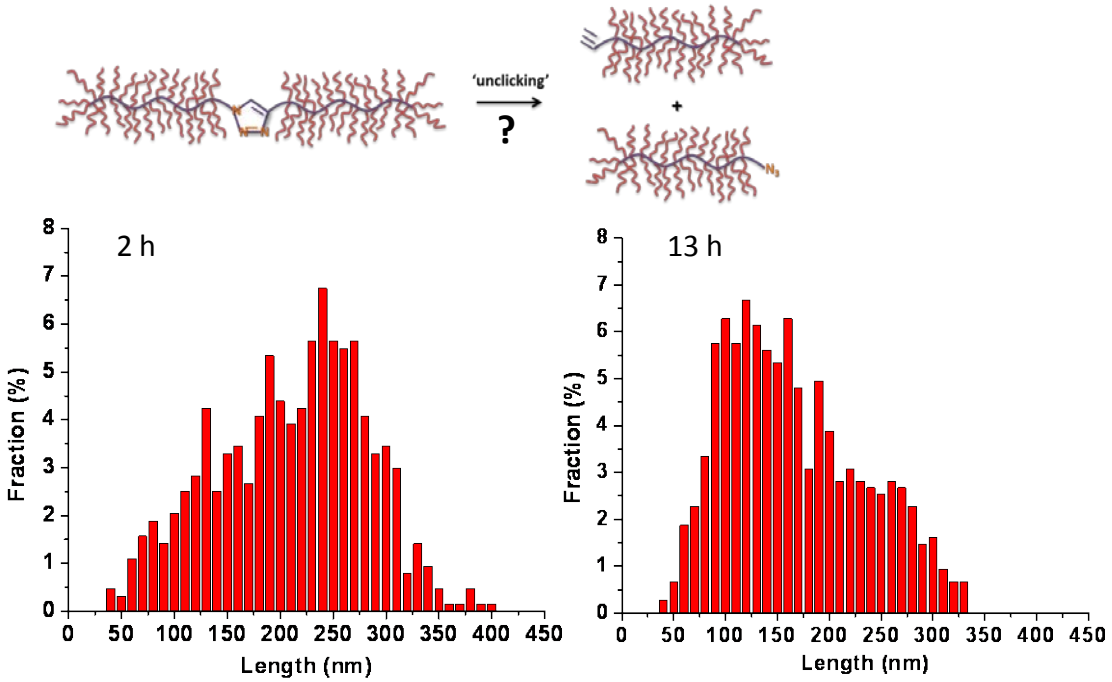

Figure 6.5 Corresponding length distributions of the molecular bottlebrushes in Figure 6.4.

Another way to verify the result is to check whether the mid-chain scission can be accelerated by catalysts (e.g. $CuSO_4$/sodium ascorbate).

References

(1) Basedow, A.; Ebert, K. In *Advances in Polymer Science*; Springer Berlin / Heidelberg: 1977; Vol. 22, p 83-148.

(2) Suslick, K. S.; Price, G. J. *Annual Review of Materials Science* **1999**, *29*, 295-326.

(3) Hennrich, F.; Krupke, R.; Arnold, K.; Rojas Stütz, J. A.; Lebedkin, S.; Koch, T.; Schimmel, T.; Kappes, M. M. *J. Phys. Chem. B* **2007**, *111*, 1932-1937.

(4) Huang, Y. Y.; Knowles, T. P. J.; Terentjev, E. M. *Advanced Materials* **2009**, *21*, 3945-3948.

(5) Caruso, M. M.; Davis, D. A.; Shen, Q.; Odom, S. A.; Sottos, N. R.; White, S. R.; Moore, J. S. *Chem. Rev.* **2009**, *109*, 5755-5798.

(6) Akyüz, A.; Catalgil-Giz, H.; Giz, A. T. *Macromolecular Chemistry and Physics* **2008**, *209*, 801-809.

(7) Brantley, J. N.; Wiggins, K. M.; Bielawski, C. W. *Science* **2011**, *333*, 1606-1609.

Appendix I

Time-dependent contribution of S-S scission

To find out the proper reaction time to suppress S-C and C-C bond scission, it is necessary to evaluate the contribution of S-S, S-C and C-C bond scission as a function of time. From our previous paper,[1] we know that the scission rate constants for S-S, S-C and C-C bonds are $k_{s-s} = 4.3 \times 10^{-4}$ s^{-1} (1.9 nN), $k_{s-c} = 7.6 \times 10^{-6}$ s^{-1} (2.3 nN) and $k_{c-c} = 1.5 \times 10^{-6}$ s^{-1} (2.2 nN), respectively. For a bottlebrush molecule with an intact disulfide linker, the disulfide bond or one of the two S-C bonds, and ~5 C-C bonds (assuming the limiting length of ~60 nm)[2-3] could break. One should note that S-S scission and S-C scission were competing reactions and that C-C scission was independent of the competing reactions. Then we can estimate the ratio of broken S-S bonds to all broken bonds to be larger than

$$\frac{\frac{k_{s-s}}{k_{s-s}+k_{s-c}} \times [1 - e^{-(k_{s-s}+k_{s-c})t}]}{[1 - e^{-(k_{s-s}+k_{s-c})t}] + 5 \times (1 - e^{-k_{c-c}t})} \cong \frac{1 - e^{-k_{s-s}t}}{(1 - e^{-k_{s-s}t}) + 5 \times (1 - e^{-k_{c-c}t})}$$

$$= \frac{1 - e^{-4.3\times10^{-4}t}}{\left(1 - e^{-4.3\times10^{-4}t}\right) + 5 \times \left(1 - e^{-1.5\times10^{-6}t}\right)}$$

at applied tension of 1.9 nN, as showed in Figure A1. To keep the fraction of broken S-S bonds above 95%, the reaction time should be no longer than ~6600 s (i.e. 110 min).

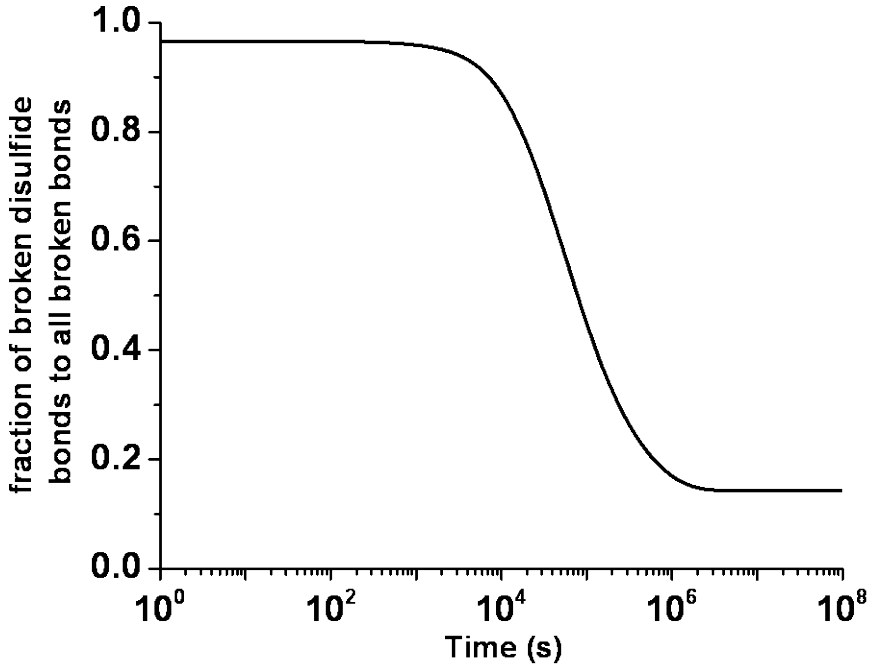

Figure A1. Contribution of S-S bond scission as a function of time.

Appendix II

Scission kinetics based on number fraction of S-S bonds

The number fraction of the disulfide linkers (ψ) exactly corresponds to the number fraction of the prior-to-scission molecules, which can be obtained from the length distribution histograms by integrating the area of the distribution band at L≅320 nm (Figure 3.2). Thus the number fraction of broken molecules equals $1-\psi$. Then we can obtain the following equations relating L and ψ,

$$L = L_2\psi + L_1(1-\psi) = (1+\psi)L_\infty$$

$$L_0 = L_2\psi_0 + L_1(1-\psi_0) = (1+\psi_0)L_\infty$$

where ψ_0 is the number fraction at $t = 0$. Here we rewrite eq. 3.9 as

$$\left(\frac{L_\infty}{L} - 1\right) / \left(\frac{L_\infty}{L_0} - 1\right) = e^{-kt}$$

By plugging $\frac{L_\infty}{L} = \frac{1}{1+\psi}$ and $\frac{L_\infty}{L_0} = \frac{1}{1+\psi_0}$ in equation above, we can derive the kinetic equation based on the number fraction of S-S bonds as

$$(1 + 1/\psi_0)/(1 + 1/\psi) = e^{-kt}$$

Appendix III

Tension drop in the middle section of the bottlebrush backbone

Calculations of backbone tension in regular bottle-brush macromolecules assume a uniform grafting density of the side chains. In the case of disulfide-linked bottlebrushes, this assumption should be revisited because of the extended spacer connecting the S-S bond to the brush backbone at both sides. The spacer does not carry side chains resulting in a local decline of the backbone tension as schematically shown in Figure A2. From the chemical structure in Figure 3.1, the total contour length of the spacer including the S-S bond is ~2 nm. The scaling relation $f \cong S \cdot x$ for the tension gradient at the ends of a bottlebrush backbone predicts that the tension drop in the middle of the spacer is $\Delta f/f \cong l/d = 2/60 = 0.03$, i.e. about 3%.[4] Correspondingly, this decrease in tension allows for a 3% increase of Δx, which would raise the obtained $\Delta x = 0.024\ nm$ by about 0.001 nm.

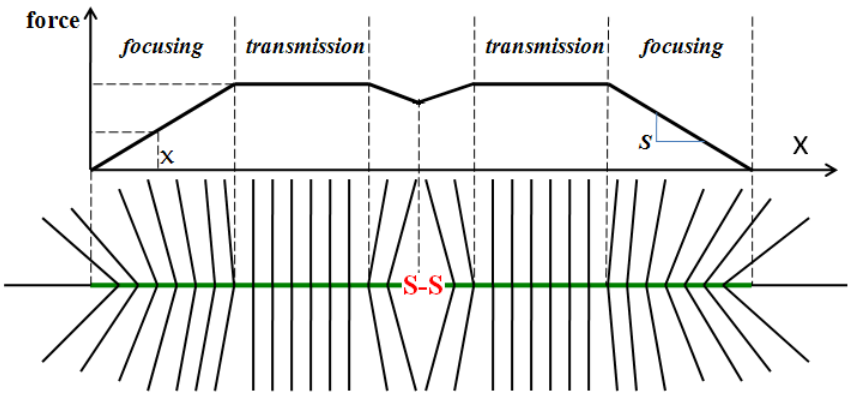

Figure A2. The tension profile along the bottlebrush backbone includes focusing and transmission zones at bottlebrush ends and central sections, respectively. In addition, the disulfide spacer (free of side chains) in the middle of the backbone creates a local drop of backbone tension. The gradient of backbone tension both at the backbone ends and in the spacer is given by $f \cong S \cdot x$.

Appendix IV

Bottlebrush width vs. DP of side chains

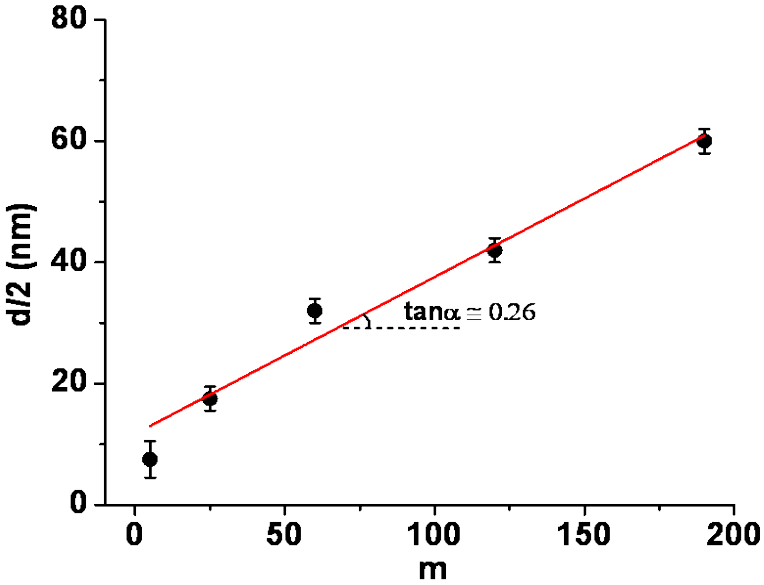

Figure A3. Change of contour length (d/2) with the degree of polymerization (m) of the side chains of PT bottlebrushes. The solid line is a linear fit, where the slope agrees with the monomer length (0.25 nm) of butyl acrylate.

Appendix V

Background spectrum

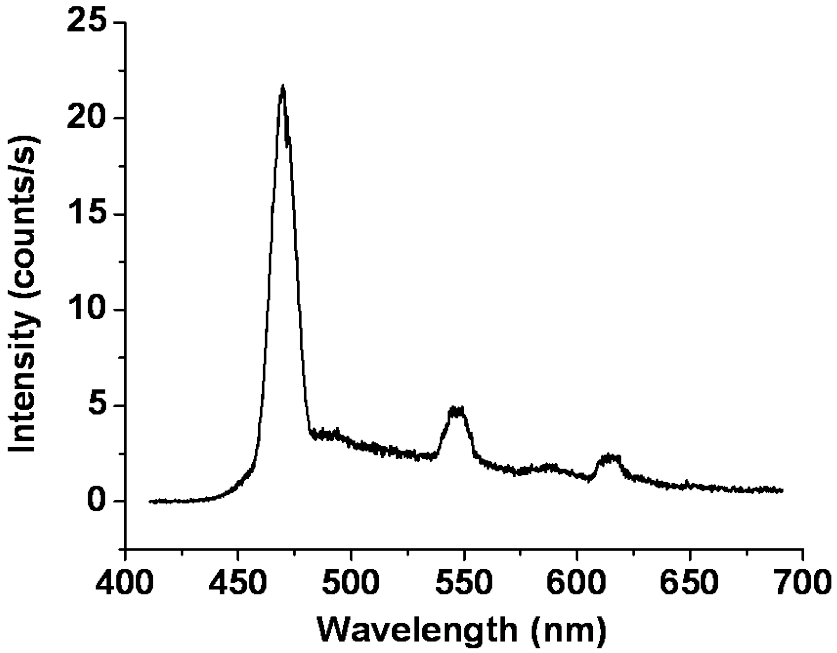

Figure A4. The background signal of 0.5% 2-propanol without deposited PT bottlebrushes at excitation wavelength of 405 nm. The peak at ~470 nm belongs to Raman scattering of water molecules.

Appendix VI

Photobleaching

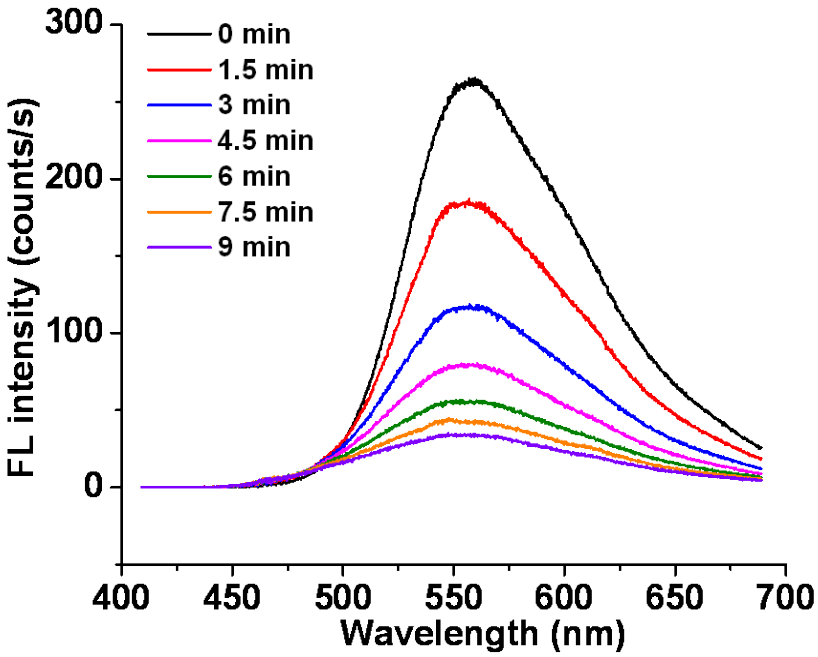

Figure A5. FL spectra of PT-60 bottlebrushes on 0.5% 2-propanol substrate at a constant pressure of 12 mN/m after different exposure times to excitation light (405 nm).

Appendix VII

Backbone conformation change of PT-190 with pressure

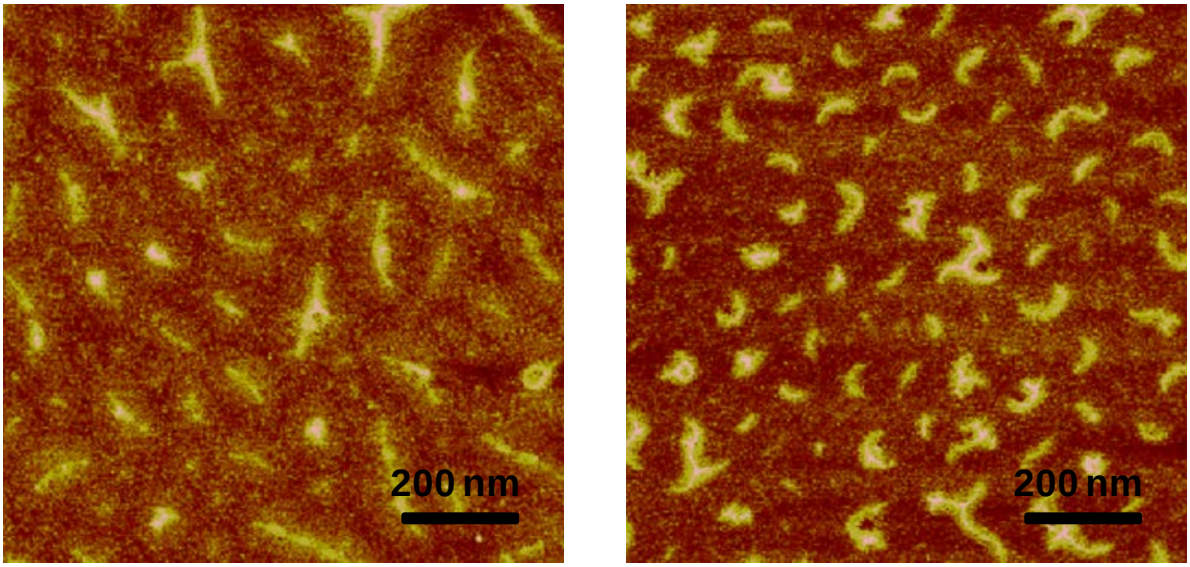

Figure A6. AFM height micrographs of PT-190 bottlebrushes transferred to freshly cleaved mica substrates from the surface of 0.5% 2-propanol substrate at different pressures: 2mN/m (left) and 17 mN/m (right), respectively.

Appendix VIII

Deformation of bong length and angle with tension

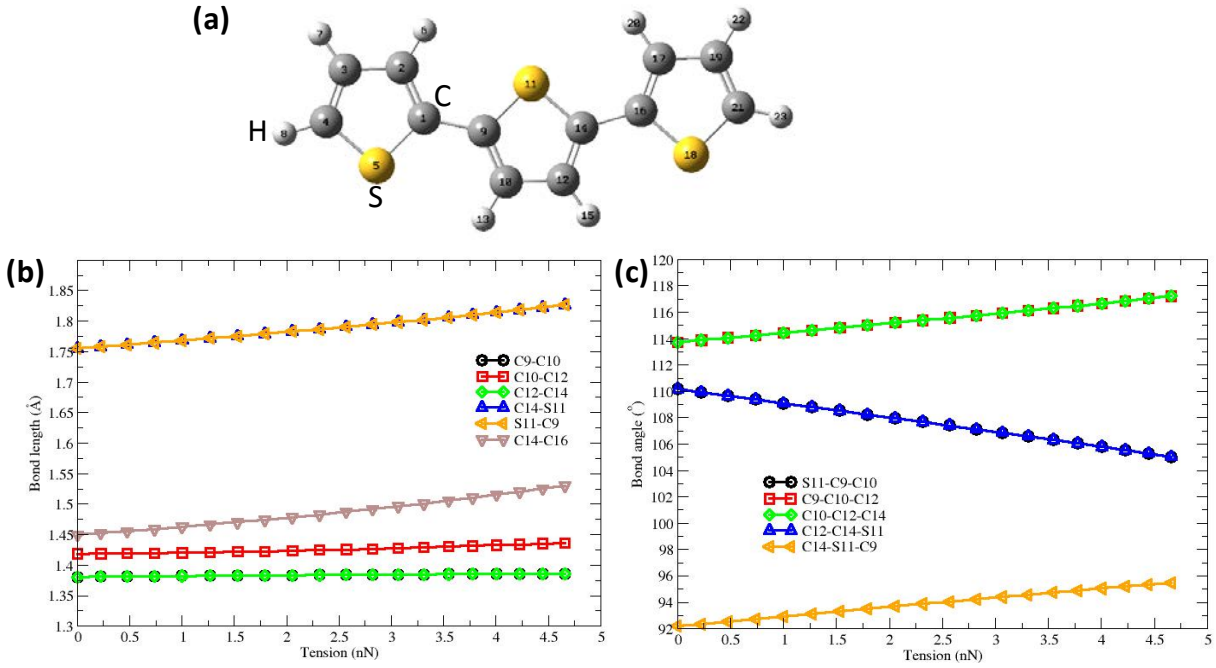

Figure A7. (a) The model of oligothiophene with three monomers. (b, c) Change of bond length and angle in the middle thiophene unit with applied tension respectively, shown as an example.

Appendix References

(1) Park, I.; Sheiko, S. S.; Nese, A.; Matyjaszewski, K. *Macromolecules* **2009**, *42*, 1805-1807.

(2) Sheiko, S. S.; Sun, F. C.; Randall, A.; Shirvanyants, D.; Rubinstein, M.; Lee, H.-i.; Matyjaszewski, K. *Nature* **2006**, *440*, 191-194.

(3) Lebedeva, N. V.; Sun, F. C.; Lee, H.-i.; Matyjaszewski, K.; Sheiko, S. S. *J. Am. Chem. Soc.* **2008**, *130*, 4228-4229.

(4) Park, I.; Nese, A.; Pietrasik, J.; Matyjaszewski, K.; Sheiko, S. S. *J. Mater. Chem.* **2011**, *21*, 8448-8453.